Inhalable Nano-structured Microparticles for Lung Cancer Treatment

Dissertation

zur Erlangung des Grades

des Doktors der Naturwissenschaften

der Naturwissenschaftlich-Technischen Fakultät

der Universität des Saarlandes

von

Salma Mahmoud AbdelHafez AbdelFattah

Saarbrücken

2023

Die vorliegende Arbeit wurde unter der Betreuung von **Prof. Dr. Marc Schneider** am Institut für Biopharmazie und Pharmazeutische Technologie der Universität des Saarlandes angefertigt.

List of contents

List of abbreviations

^{1}H-NMR	Proton nuclear magnetic resonance
2D	Two-dimensional
3D	Three-dimensional
A549	Adenocarcinoma human alveolar epithelial cells
AcMD	Acetalated maltodextrin
AcMD-NPs	Acetalated maltodextrin nanoparticles
ANOVA	Analysis of variance
BCA	Bicinchoninic acid
CLSM	Confocal laser scanning microscope
CO_2	Carbon dioxide
CTF	Corrected total fluorescence
Đ	Dispersity
D_{ae}	Aerodynamic diameter
DAPI	4′,6-Diamidino-2-phenylindole
DBU	1,8-Diazabicyclo[5.4.0]undec-7-ene
DE	Dextrose equivalent
D_{geo}	Geometric diameter
DL	Drug loading
DLS	Dynamic light scattering
DMSO	Dimethyl sulfoxide
DPBS	Dulbecco's phosphate buffered saline
DPI	Dry powder inhaler
DSC	Differential scanning calorimetry
dTHP-1	Differentiated human macrophage-like THP-1 cells
ECM	Extracellular matrix
ED	Emitted dose
EDTA	Ethylenediaminetetraacetic acid
EE	Entrapment efficiency
FBS	Fetal bovine serum
FCS	Fetal calf serum
FPF	Fine particle fraction
GSD	Geometric standard deviation

HPLC	High performance liquid chromatography
IntDen	Integrated density
KCl	Potassium chloride
MD	Maltodextrin
MEM	Minimum essential medium
MMAD	Mass median aerodynamic diameter
M_n	Number average molecular weight
MOC	Micro-orifice collector
MPs	Microparticles
MRC-5	Human fetal lung fibroblasts
MTT	3-(4,5-Dimethylthiazol-2-yl)-2,5-diphenyl-2H-tetrazolium bromide
M_w	Weight average molecular weight
NGI	Next generation impactor
NHS	*N*-Hydroxysuccinimide
NPs	Nanoparticles
NSCLC	Non-small cell lung cancer
OD	Optical density
PBS	Phosphate buffered saline
PDI	Polydispersity index
Pe	Peclet number
PEG	Polyethylene glycol
PMA	Phorbol 12-myristate 13-acetate
pMDI	Pressurized metered-dose inhaler
PMMA	Poly(methyl methacrylate)
PPTS	Pyridinium *p*-toluene sulfonate
PVA	Polyvinyl alcohol
Rhod-AcMD	Rhodamine-conjugated acetalated maltodextrin
Rhod-AcMD-NPs	Rhodamine-conjugated acetalated maltodextrin nanoparticles
Rhod-MD	Rhodamine-conjugated maltodextrin
RPMI-1640	Roswell Park Memorial Institute medium
SEC	Size exclusion chromatography
SEM	Scanning electron microscope
SCLC	Small cell lung cancer
SLF	Simulated lung fluid

SMI	Soft mist inhaler
TEA	Triethylamine
T_g	Glass transition temperature
TGA	Thermogravimetric analysis
THP-1	Acute leukemia human monocytic cells
TME	Tumor microenvironment
T_{onset}	Onset decomposition temperature
USP	United States Pharmacopeia
UV	Ultraviolet

List of tables

List of figures

Summary

Zusammenfassung

1. Summary

Lung cancer is the most lethal cancer among all malignancies worldwide. Whether applied alone or combined with other interventions, intravenous chemotherapy is a first-line treatment in most lung cancer cases. However, poor response is usually realized due to suboptimal drug concentration in cancerous tissue and systemic side effects. Through achieving higher drug concentration in the lungs and limiting the systemic exposure, the pulmonary route provides a dual solution to the drawbacks of systemic administration. This work aims to design an inhalable nano-in-micro particulate delivery system for lung cancer treatment. For composing the nanoparticle (NP) part of the system, maltodextrin was modified into hydrophobic acetalated maltodextrin (AcMD) with acid-triggered degradation. Nanoprecipitation yielded uniform AcMD-NPs, that were loaded with a hydrophobic model drug, resveratrol. The AcMD-NPs exhibited tunable degradation and release in acidic pH. They were well tolerated by lung adenocarcinoma A549 and differentiated monocytic THP-1 cells but showed different uptake behavior. For efficient pulmonary deposition, the AcMD-NPs were embedded into microparticles (MPs) via spray drying. Collagenase was added to the MP matrix for enhancing the NP intratumoral penetration through extracellular matrix modulation. Collagenase was demonstrated to enhance the NP penetration into a lung cancer spheroid co-culture model, consisting of A549 cells and lung MRC-5 fibroblasts.

2. Zusammenfassung

Lungenkrebs ist die Krebsart mit der höchsten Mortalität. Chemotherapie wird als intravenöse Erstbehandlung entweder allein oder in Kombination mit anderen Maßnahmen angewendet. Aufgrund der suboptimalen Arzneimittelkonzentration im Krebsgewebe sowie Nebenwirkungen erreicht man ein schlechtes Ansprechen des Tumors. Durch höherer lokale Arzneimittelkonzentration in der Lunge und Begrenzung der systemischen Exposition bietet die pulmonale Applikation einen zweifachen Benefit gegenüber der systemischen Verabreichung. Diese Arbeit zielt darauf ab, ein inhalierbares Nano-in-Mikro-Partikelabgabesystem für die Behandlung von Lungenkrebs zu entwickeln. Zum Aufbau der Nanopartikel wurde Maltodextrin mithilfe der säurelabilen Acetalbindung hydrophobisiert (acetalisiertes Maltodextrin (AcMD)). Die Nanopräzipitation ergab einheitliche AcMD-Nanopartikel (NP), die mit einem Modellwirkstoff, Resveratrol, beladen wurden. Die AcMD-NP zeigten bei saurem pH-Wert einen einstellbaren Abbau sowie Freisetzung. Sie wurden von Lungenadenokarzinom-A549- und differenzierten monozytären THP-1-Zellen gut vertragen, zeigten jedoch unterschiedliches Aufnahmeverhalten. Für pulmonale Ablagerung wurden die AcMD-NP durch Sprühtrocknung in Mikropartikel (MP) eingebettet. Kollagenase wurde zu der MP-Matrix hinzugefügt, um die intratumorale Penetration der NP zu verbessern. Die Kollagenase hat das NP-Eindringen in ein Sphäroid-modell, das aus A549-Zellen und Lungenfibroblasten MRC-5 besteht, verbessert.

General introduction

3. General introduction

3.1 Lung cancer

3.1.1 Incidence, mortality, epidemiology, and etiology

As reported in the latest global cancer statistics in 2020 [1, 2], lung cancer is the second most diagnosed cancer worldwide (11.4% of all cancer types), occupying the highest incidence in males (14.3%) and the third highest incidence in females (8.4%) (**Figure 1**). In terms of mortality, lung cancer is the leading cause of cancer-related deaths (18.0%), where it is ranked first in males (21.5%) and second in females (13.7%) (**Figure 1**). Due to the expanding global use of tobacco, it is estimated that the lung cancer burden will continue to grow in the future [3, 4]. The incidence and mortality rates of lung cancer is reported to be higher in the developed countries. However, the lack of a proper reporting system and reliable statistical data in the developing countries might not reflect the real situation [5]. The foremost risk factor of lung cancer that outweighs all the other risk factors is tobacco smoking. Other risk factors include air pollution, occupational exposure, chronic pulmonary diseases, obesity, and other lifestyle factors [4].
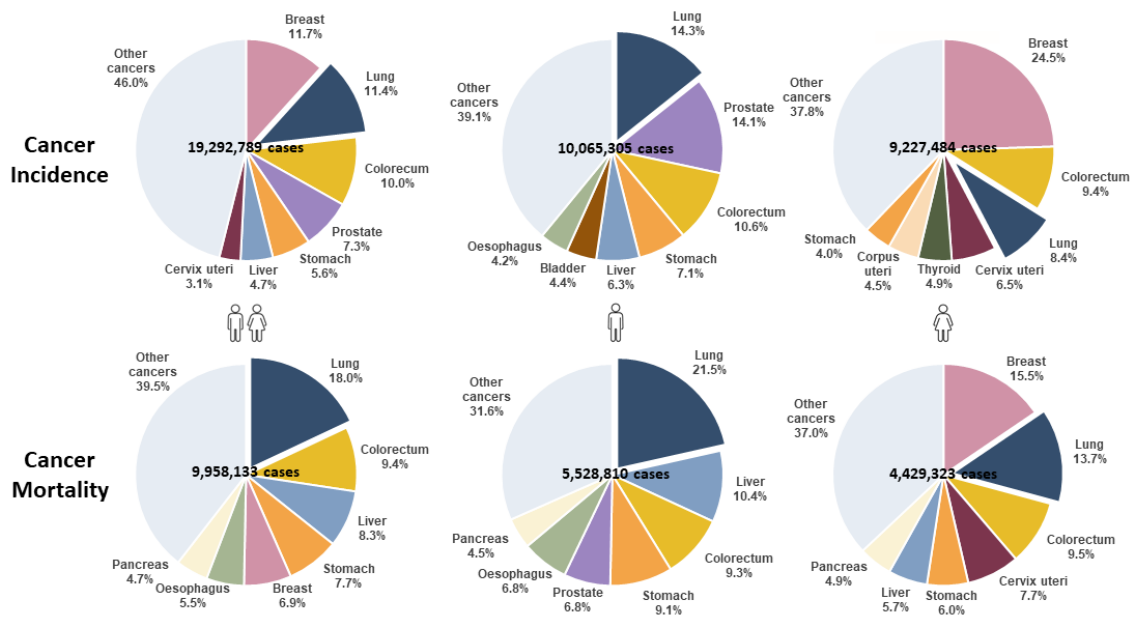
Figure 1. Worldwide incidence and mortality rates of lung cancer among other cancer types for both genders, male, and female populations as indicated. The displayed data are based on the latest cancer statistical reports [1, 2].

3.1.2 Histological types and subtypes

Lung cancer is classically categorized into two broad histological types: small cell lung cancer (SCLC) and non-small cell lung cancer (NSCLC), accounting for approximately 15% and 85% of all lung cancer incidences, respectively [6, 7]. SCLC is highly aggressive; associated with rapid progression, early metastasis, chemo-resistance, and very low survival rates [8-10]. Based on the current lung cancer classification, two subtypes are listed for SCLC: small cell carcinoma and combined small cell carcinoma [8, 11]. The more incident lung cancer type, NSCLC, is mainly subclassified into adenocarcinoma, squamous cell carcinoma and large cell carcinoma, representing 40%, 25-30% and 10-15% of the total lung cancer cases [5, 12]. Further lung cancer subclasses and subclass combinations have recently been identified according to the expressed histopathological features, molecular profiles, and gene mutations [6, 11, 13]. In addition to the cytopathological aspects, lung cancer subtypes differ with respect to the location at which they develop in the lungs. While most SCLC and squamous cell carcinoma tumors tend to locate centrally [8, 14], adenocarcinomas develop in the bronchiolar and alveolar regions and hence are mainly more peripherally located [14, 15].

3.1.3 NSCLC treatment modalities

The selection of treatment strategy and its objective, i.e., curative or palliative, for a NSCLC case is stage specific. Complete surgical resection is the typical primary intervention for stage I, II and IIIA NSCLC patients [16, 17]. If the tumor is unresectable or surgery is contraindicated, primary radiotherapy is the next treatment option to be considered [5, 17]. Although their therapeutic benefit for early-stage NSCLC is controversial, neoadjuvant or adjuvant therapy could be administered to improve the outcome of surgery and clear micro- or distant metastasis [18, 19]. Chemotherapy, radiation, and targeted therapy are alternatives for adjuvant therapy, where most stage II and IIIA NSCLC patients undergo adjuvant chemotherapy to diminish the risk of cancer relapse [16]. Treatment options for stage IIIB and IV cases are chemotherapy, targeted therapy, radiotherapy with/without surgery, where the treatment goal in these advanced stages is largely palliative. The decision of the treatment interventions and their sequence depends on the tumor location, the patient's general status and the presence of comorbidities [17, 20, 21].

3.2 The extracellular matrix (ECM)

The ECM is an acellular constitutional component, that is widespread over all the body tissues and organs and serves as a scaffold for the cellular components. From the organism development and throughout life, it plays an essential role in tissue formation, morphogenesis, repair, and homeostasis [22]. Two broad types of ECM can be distinguished and are well compartmentalized from each other: the interstitial matrix, which fills the extracellular spaces within the tissue, and the highly specialized basement membrane, which separates the epithelial cells from the stromal compartments and other tissues [22-24]. The ECM function, composition and pathological changes in solid tumors would be addressed in the following subsections.

3.2.1 The ECM physiological functions

Through its three dimensional (3D) complex mesh-like structure, the ECM provides mechanical and architectural support to the residing cells, maintains the organ integrity, and acts as a reservoir for water and growth factors [25]. It defines the tissue boundaries and hence, restricts cell migration and aberrant proliferation [26]. It imparts elasticity to organs, which is of particular importance during organ development and morphogenesis [27]. In addition to structural functions, the ECM regulates cellular processes including cell adhesion, proliferation, survival, migration, and invasion [28]. A reciprocal interaction exists between the ECM and the tissue/organ cells; while cells deposit, degenerate, and remodel the ECM, the ECM mutually influences the cell behavior [22, 29]. A balance between the ECM deposition and degradation is an essential part of homeostasis. Reduced or elevated ECM turnover result in tissue fibrosis or destruction, respectively, with both contributing to cancer progression [30, 31].

3.2.2 Pathological features and effects of ECM in solid tumors

The onset of cancer and its progression are associated with a high degree of ECM dysregulation at the biochemical, biomechanical, and structural levels [22]. Desmoplasia (involving fibroblast expansion and activation, increased deposition and crosslinking of ECM molecules, increased angiogenesis and tissue inflammation [32]) is a common

manifestation in several solid tumors, including lung tumors, and resembles tissue fibrosis in many aspects [33, 34]. Both cancer cells and fibroblasts interplay with the tumor microenvironment (TME), resulting in increased stiffness of the ECM through excessive secretion and reduced catabolism of collagen and hyaluronic acid. Stiffening of the ECM is consequently accompanied by further malignant alterations, creating a positive loop that accelerates the disease progression. A dense ECM accumulates growth factors and promotes multiple signaling pathways involved in malignant transformation, cancerous proliferation, metastasis, angiogenesis, genome instability, immunosuppression, and resistance to therapy [25].

3.2.3   The ECM composition

The mammalian ECM comprises approximately 300 different proteins, where the ECM composition varies based on its type and location [23]. The components of ECM can be chemically classified into proteins and glycoproteins (such as collagen, fibronectin, elastin and laminin), glycosaminoglycans (mainly hyaluronic acid) and proteoglycans (such as heparan sulfate and chondroitin sulfate). The ECM building blocks assemble and interconnect in different arrays, yielding infinite number of shapes, geometries and topologies [22].

3.2.4   Collagen: the main component of the ECM

Collagen is the major structural component and most abundant protein in the interstitial matrix, representing about 90% of the ECM protein and 30% of the total proteins in humans [25]. To date, 28 types of collagen have been differentiated [35]. All collagens have triple helix structure, consisting of homo- or heterotrimers of three polypeptide chains [25, 36]. Among all the matrix components, collagen is the most observed element to change in either deposition, degradation, organization and/or post-translational modification in solid tumors with respect to healthy tissues [37]. Fibrillar collagen I is a main constituent of tumor desmoplasia, and could be correlated to cancer cell survival and metastasis in many solid tumors [33].

3.2.5 The ECM as a barrier against the delivery of therapeutics

The heterogenous rigid ECM network that is deposited around and throughout the solid tumor constitutes an immense physical barrier **(Figure 2)**, thereby impeding the intratumoral delivery of therapeutics and accordingly reducing their therapeutic efficacy [38]. The dense ECM raises the tumoral interstitial pressure and hampers the diffusive and convective transport within the tumor matrix [39, 40]. Additionally, the high interstitial pressure compresses the tumor vasculature and hence impairs the perfusion of circulating therapeutic agents into the tumor tissue [41]. In certain solid tumors, the collagen fibrous network was characterized to have 20 - 42 or 75 - 130 nm interfibrillar spacing in compactly aligned or loosely arranged collagen fibrils, respectively, thereby restricting the particulate drug transport [42].
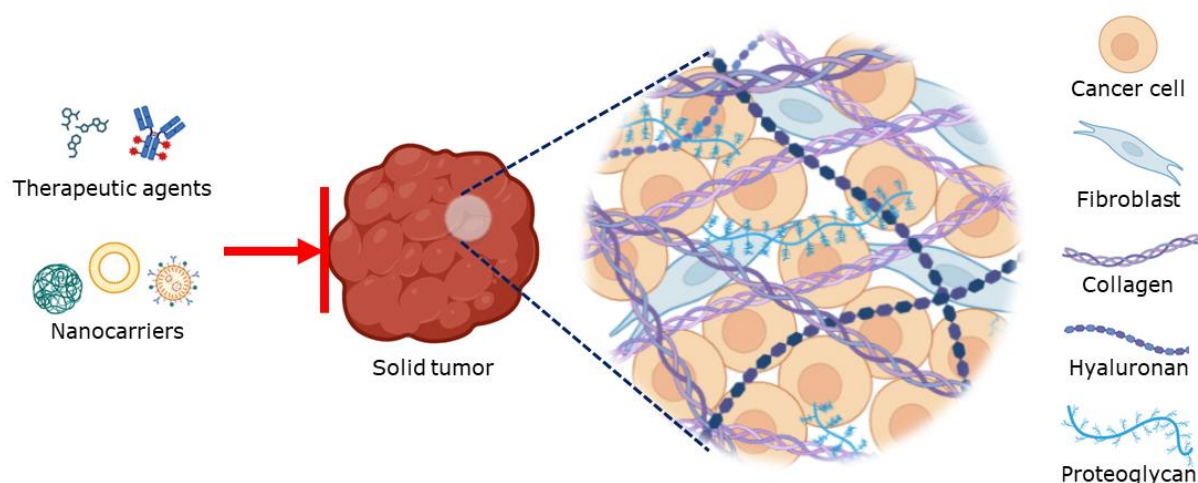
Figure 2. Illustration of the ECM and its main structural components, acting as a physical barrier against the perfusion, penetration, and diffusion of therapeutic agents and nanocarriers into solid tumors. This figure was created with BioRender.com.

3.3 The lungs as a route of administration

The pulmonary route has been regarded as an effective route of administration for both local and systemic delivery of therapeutics. It offers several advantages such as non-invasiveness, rapid onset of action, self-administration, and high patient compliance. Inhalation therapy has been favorably used for the treatment of respiratory diseases such as

bronchitis, asthma, cystic fibrosis, and chronic obstructive pulmonary disease. Besides, the lungs have great potential for systemic delivery due to their huge surface area, thin alveolar barrier, rich vascularization, limited metabolic activity and avoidance of first pass metabolism. However, pulmonary deposition is governed by intricate physiological, pathophysiological, and pharmaceutical factors, influencing the therapeutic effectiveness of inhaled treatment, and rendering it a challenging route of administration [43-45].

3.3.1 Anatomy, histology, and physiology of the lungs

There are several ways to classify the regions of the respiratory tract. Anatomically, it is divided into three regions: the extrathoracic region (the nasal/oral cavity, pharynx, larynx, and tracheal entrance), the tracheobronchial region (the trachea, bronchi, and terminal bronchioles), and the alveolar region (the respiratory bronchioles, alveolar ducts, and alveolar sacs, which are clustering groups of alveoli) [46]. Another common method divides the lungs into two functional zones: the conducting airways (responsible for filtration and conditioning of the inhaled air) and the respiratory airways (responsible for gas exchange). The conducting airways extends from the nasal/oral cavity to the terminal bronchioles, whereas the respiratory airways comprise the respiratory bronchioles, alveolar ducts, and alveolar sacs [43]. The pulmonary tract and its anatomical and functional divisions are illustrated in **figure 3**.
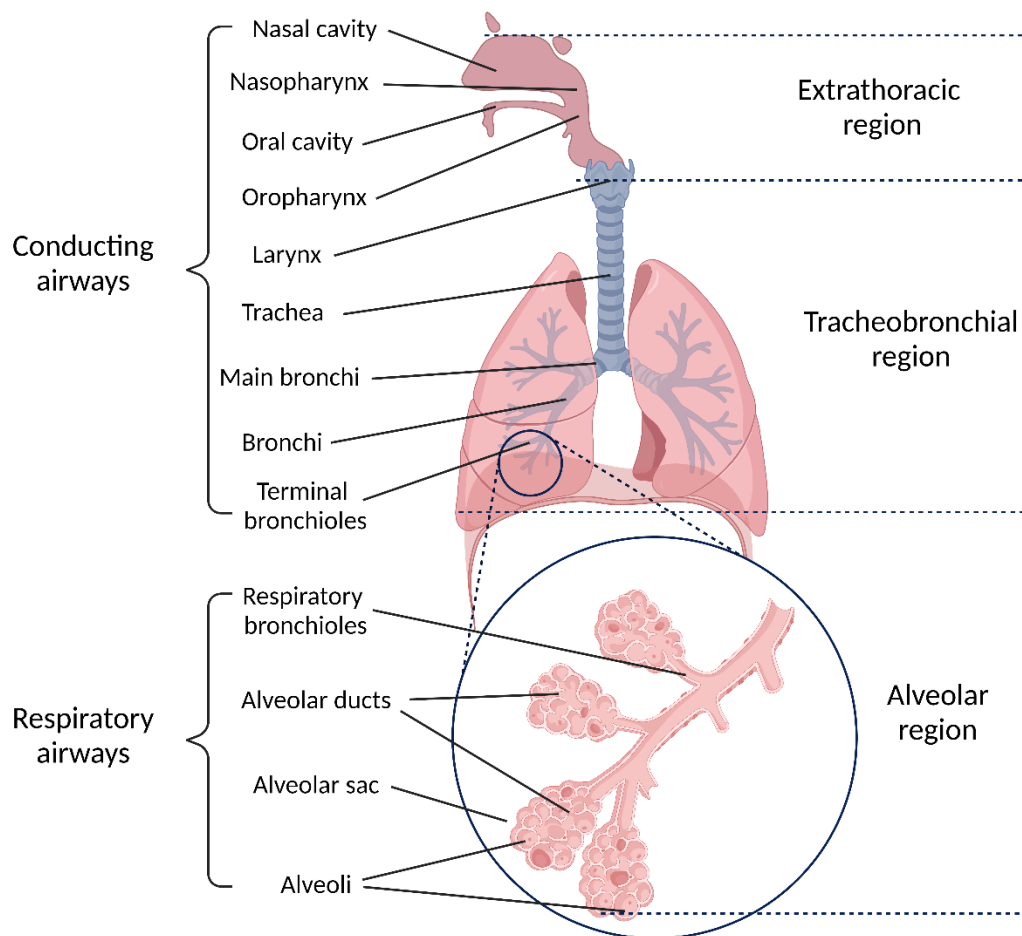
Figure 3. Illustration of the pulmonary tree showing its main anatomical regions (extrathoracic, tracheobronchial, and alveolar regions) and functional zones (conducting and respiratory airways). This figure was created with BioRender.com.

The tracheal epithelium consists of ciliated columnar cells, basal cells, and mucus-secreting goblet cells and glands. The cilia are submerged in the epithelial lining fluid, through which their tips protrude into the mucus layer that covers the inner surface of the trachea. The histological composition of the bronchial epithelium resembles that of the tracheal epithelium with the presence of non-ciliated cells (Clara or club cells as they are called today). Whereas the bronchiolar epithelium comprises ciliated cuboidal cells, more abundant club cells, less goblet cells, and no glands. Progressing distally through the bifurcations of bronchi and bronchioles, the ciliary coverage becomes less dense, and the mucus lining decreases in thickness. On the other hand, the alveolar epithelium is composed

of flat squamous cells, devoid of mucus, and lined with a thin layer of pulmonary surfactant [43, 47].

3.3.2   Mechanisms of aerosol deposition

Based on particle diameter, particles for inhalation are classified into coarse particles (> 5 μm), fine particles (between 0.1 and 5 μm) and ultrafine particles (< 0.1 μm). Upon inhalation, aerosol particles are deposited along the respiratory tract relying on various formulation related factors: particle diameter, shape, and density; and physiological factors: breathing pattern, inspiration flow rate, lung volume, inspiration volume, and disease state. These factors dictate the main deposition pattern **(Figure 4)**, whether it is impaction, sedimentation, interception, or diffusion, and accordingly the region of major deposition in the respiratory tract [48-50].
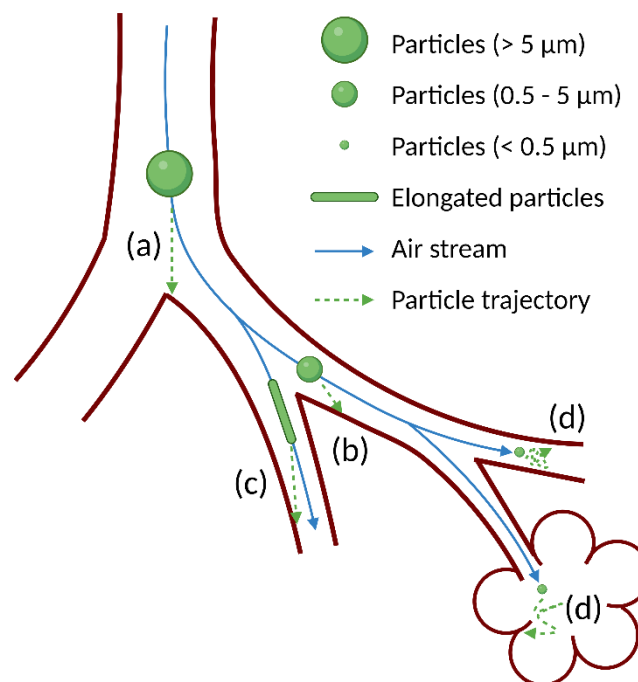
Figure 4. Particle deposition mechanisms in the respiratory tract. Predominant particle deposition mechanism is either (a) impaction, (b) sedimentation, (c) interception, or (d) diffusion for large particles (> 5 μm), smaller particles (0.5 – 5 μm), elongated particles, and small particles (< 0.5 μm), respectively. This figure was created with BioRender.com.

3.3.2.1 Impaction

Inertial impaction is the prevalent mechanism of deposition for large particles (> 5 μm). Due to their high inertia, large particles do not follow the trajectory of the high velocity air stream and impact the wall of the respiratory tract **(Figure 4a)** [48, 51]. Therefore, large particles deviate early from the inspired airstream and deposit at the upper airways (the oropharyngeal and tracheobronchial regions).

3.3.2.2 Sedimentation

Particles of smaller diameters (0.5 – 5 μm) mostly evade impaction at the upper airways and deposit by gravitational sedimentation at the lower airways (lower bronchial and alveolar regions), where the air velocity is slower **(Figure 4b)** [50]. The rate of sedimentation is directly proportional to the particle size and inversely proportional to the flow rate. Therefore, particles in the range from 3 to 5 μm deposit at the lower bronchial region, whereas particles smaller than 3 μm have greater chance to deposit at the deep alveoli [52].

3.3.2.3 Interception

Interception is specifically relevant for elongated particles (fibers). Unlike large spherical particles, elongated particles of comparable sizes do not impact out of the air stream and deposit later at smaller-diameter airways when they contact the airway wall **(Figure 4c)**. Therefore, these particles are characterized by smaller aerodynamic diameters in relation to their geometric dimensions [52, 53].

3.3.2.4 Diffusion

Particles of diameters smaller than 0.5 μm are most influenced by diffusion rather than impaction or sedimentation, causing the deposition of these small particles at the alveolar region **(Figure 4d)**. Diffusion occurs due to Brownian motion, which is inversely proportional to both particle diameter and flow rate. Diffusing particles move, driven by the concentration gradient across the airstream, and deposit once they contact the walls of

the airways. It is worth noting that diffusion is dependent on the geometric size of the particles and not their aerodynamic diameter [52, 54].

3.3.3 Pulmonary clearance mechanisms

Inhaled particles that are deposited in the lungs have different fates depending on their physicochemical properties and region of deposition [55]. Insoluble particles are cleared either by mucociliary escalation or phagocytosis, whereas soluble particles, after being dissolved, or released drugs can be absorbed into blood/lymphatic circulation or metabolized [56]. There are several clearance mechanisms along the regions of the pulmonary tract that will be briefly discussed in the following subsections.

3.3.3.1 Mechanical clearance

Large particles are subjected to mechanical clearance spontaneously after their deposition at the large upper airways. Mechanical clearance may occur by coughing, sneezing, or swallowing, where coughing for example is instantly triggered by inhalation of particles larger than 10 μm in size [43]. Therefore, the fraction of particles in an aerosol having particle sizes exceeding 10 μm should importantly be as low as possible [53], otherwise the deposited fraction of the whole inhaled powder would drop significantly through the stimulation of coughing and the consequent powder exhalation.

3.3.3.2 Mucociliary clearance

Mucociliary clearance is the main mechanism for removing insoluble foreign particles from the central airways. It occurs in the tracheobronchial region, where the particles are trapped within the mucus layer and the ciliated epithelium sweeps them towards the pharynx [57]. Additionally, the lining layer of mucus acts as a physical barrier to particle penetration. Inhaled particles that are deposited in the conducting zone are cleared through mucociliary escalator within 15 min to 2 h after inhalation [58].

3.3.3.3 Alveolar macrophages

Inhaled particles that bypassed the mucociliary clearance at the conducting zone are prone to phagocytosis by the alveolar macrophages, relying on their surface chemistry and

physicochemical properties [45, 59]. Alveolar macrophages can also move up assisted by the mucociliary escalator and contribute to particle phagocytosis at the conducting airways [60]. Engulfment of particles by alveolar macrophages is still the main obstacle to attain controlled release in the alveoli [43], where the particles are cleared before full drug release and exerting the anticipated therapeutic effect.

3.3.3.4 Enzymatic degradation

The extent of enzymatic degradation in the respiratory tract is in principle much lower compared to that in the liver or the gastrointestinal tract. Nevertheless, the lung epithelia comprise esterases, peptidases, and cytochrome P450 enzymes, from which some isoforms (such as CYP2S and CYP2F) have been recognized to be lung specific. The abundance of these enzymes and their concentration differs among the different cell types along the respiratory tract lining [61, 62].

3.4 Pulmonary delivery for lung cancer treatment

3.4.1 Advantages of inhaled chemotherapy

The delivery of chemotherapeutics through the pulmonary route has several advantages compared to conventional intravenous administration [63]. Inhalation could be regarded as a localized method of administration, where the inhaled substance (of suitable aerodynamic properties) is majorly deposited at the lungs. This direct access enables the delivery of higher doses of chemo- or targeted therapeutics to the cancerous lung tissue, as well as the reduction of off-target delivery and its associated side effects. Combining both effects is prospected to boost the therapeutic ratio of the administered treatment and accordingly increase its effectiveness [64]. Additionally, through minimizing the systemic toxic side effects, treatment interruptions, that are responsible for tumor cell repopulation, could be avoided. The inhalation route may also potentiate the drug penetration into the lung tumor, by maintaining a positive drug concentration gradient at the tumor site [65]. Pulmonary solid tumors located in the conducting or respiratory zone are fed by bronchial vascularization or pulmonary circulation, respectively. Accordingly, absorbed agents could recirculate in the local pulmonary circulation and reach solid tumor masses through the local blood stream [43, 63, 66]. With regard to patients, the pulmonary route of

administration is characterized by better patient compliance, as it is needle-free and may not require hospitalization.

3.4.2   Challenges and limitations of pulmonary delivery of anticancer drugs

Despite the attractive aspects of the pulmonary delivery of chemotherapeutics in lung cancer, it is still under investigation in clinical trials with no commercialized products yet. Inhalation of sole anticancer drugs results in transient high concentration in the lung tissue, leading to pulmonary toxicities [67-69]. The residence time of an inhaled chemotherapeutic agent at tumor sites might not be sufficient to exert its cytotoxic activity, where particles may be cleared by mucociliary clearance or alveolar macrophages, or they could be dissolved [67, 70, 71]. Whereas solubilized drug would be pharmacologically active, it is also very liable to enzymatic metabolism or pre-mature absorption in blood or lymphatic circulation [43, 71]. Inefficient deposition is another main encountered limitation, resulting in dose insufficiency and long administration time problems [63, 72]. In addition to those delivery related issues that could be tackled by formulation technological approaches, generation of aerosols during preparation or administration of inhaled anticancer treatment results in serious environmental contamination and health risks to the health care staff. Closed cabinets with HEPA filters and other effective measures have been studied to solve the environmental contamination and exposure problems [69, 73, 74].

3.4.3   The use of nanomedicine for pulmonary delivery to lung cancer

Utilization of nanocarriers for the pulmonary delivery of chemotherapeutics could circumvent several drawbacks of conventional inhalation chemotherapy (for example, in the form of solution or suspension), that were discussed in the previous subsection. Nanocarriers could sustain the release of the loaded anticancer drugs, thus avoiding abrupt high concentrations that induce lung toxicity. Moreover, they enable targeted and specific bioresponsive delivery through tailoring their design, composition, and physicochemical properties, which would potentially decrease or avoid non-specific interaction with healthy lung tissues. Furthermore, they suffer less from mucociliary clearance and phagocytosis compared to microparticles, thereby prolonging the residence time of inhaled therapeutics [75-77]. In addition, nanocarriers are in general physically stable enough to withstand

aerosolization, therefore nanosuspensions could be easily converted to an inhalable formulation via nebulization [78].

3.4.4 Inhaler devices and formulation aspects for pulmonary administration of chemotherapeutics

Inhalers are categorized into four main types: nebulizers, pressurized metered dose inhalers (pMDIs), soft mist inhalers (SMIs), and dry powder inhalers (DPIs) [79]. Pulmonary delivery using pMDIs and SMIs is in principle restricted to small drug doses in the range of micrograms and therefore, both devices are not easily adaptable to chemotherapeutics [63]. Nebulizers and DPIs are discussed in the following subsections.

3.4.4.1 Nebulizers

Until present, nebulization has been the most explored approach in lung cancer clinical trials [63, 67]. This is attributed to several reasons: (1) nebulizers do not require special patient coordination and can be even used by bed-ridden patients, (2) they can deliver large volumes of solutions or suspensions containing the required dose, (3) simple solutions or suspensions can be aerosolized by nebulizer; chemotherapy IV solutions for instance could be used with no need of additional formulation optimization. On the other hand, nebulization has several drawbacks with respect to portability, cleaning and disinfection, time consumption (for example, administration time reached 6 hours to deliver cisplatin liposomes [72]), environmental contamination, and formulation physical stability and contamination issues, that are particularly relevant to colloidal or particulate systems.

3.4.4.2 Dry powder inhalers (DPIs)

In contrast to nebulizers, a DPI delivers high doses in a short administration time, activated by the patient's inspiration. As its name implies, the formulation is in the solid state, thereby enhancing the formulation stability and shelf life. Additionally, anticancer drugs are mostly hydrophobic in nature and thus easier to formulate as dry powders. DPIs are portable, more economic, easier to be used by the patient with lower risk of environmental contamination, and less demanding in terms of maintenance. Therefore,

more studies have been focusing on the development of chemotherapeutics as dry powders for inhalation [80-83].

In general, the most common formulation strategy for inhalable dry powder is to use a mixture of micronized drug with coarse carrier (typically 50 – 100 μm lactose monohydrate particles), to control the strong surface forces of the drug particles and facilitate dose metering. The adhesive force between drug and carrier particles should be optimally balanced to be strong enough to endure manufacturing steps and storage, and at the same time weak enough so that the drug particles separate on inhalation [84, 85]. Due to the difficulty of achieving this balance, delivered doses with DPIs generally do not exceed 30% of the claimed dose. This poses a great limitation to the maximum doses that could be delivered to the lungs by DPIs [86, 87]. Carrier-free dry powder for inhalation has subsequently evolved and attracted much research interest. Herein, the particle composition and the powder production method control the particle size, density, shape, crystallinity, and surface charge. All these interdependent properties affect in turn the interparticle surface forces and the aerodynamic properties of the powder aerosol [85, 88], warranting extensive formulation optimization and development steps.

3.5 Spray drying and related technological aspects

Spray drying is one of the most commonly used methods for the production of inhalable powders. It is a simple and established single-step process, in which a liquid feedstock is transformed into dry powder with well-controlled properties. As a production method, spray drying possess many advantages, where it is easily scalable; robust; economical; and reproducible, it produces powders with uniform properties suitable for inhalation, and it can be used with both aqueous and organic solvent-based feed liquids. However, it may have some limitations with heat-sensitive substances, and the production yield might sometimes be unsatisfactory. The powder characteristics are governed by a multitude of factors: (1) liquid feed properties, such as viscosity, surface tension, composition, and solid material concentration, and (2) process parameters, such as nozzle type and dimensions, feed flow rate, atomization air flow, and inlet temperature [44, 85, 89].

3.5.1 Spray drying process

3.5.1.1 Feedstock preparation

The liquid feed **(Figure 5a)** is prepared by dissolving/dispersing the solid components (active substances, colloidal carriers, and/or excipients) in a suitable solvent/dispersant to yield a solution, colloidal dispersion, suspension, or emulsion [85]. The composition of the feedstock is selected based on the desired properties of the powder product and the physicochemical properties of the active substance. For colloidal dispersions, suspensions, or emulsions, the stability of the feedstock during spray drying is of particular importance to ensure the homogeneity of the produced particles. An additional point to be considered is the particle size or the presence of agglomerates, which could lead to nozzle blockage [89].

3.5.1.2 Atomization

After being pumped into the atomizer, the liquid feed is broken down into very small droplets as shown in **figure 5b**, thereby increasing the surface area and accordingly the drying efficiency. There are four main types of atomizers used in spray drying: rotary disk, single-fluid (hydraulic), two-fluid (pneumatic), and ultrasonic nozzle atomizers. Two-fluid nozzles are commonly utilized for the production of inhalable particles, in which atomization occurs by the disruption of liquid feed by high velocity gas stream [89, 90]. Compared to the other atomizers, they produce sprays with relatively uniform smaller droplet size (1 – 100 μm), where the droplet size is influenced by the feed flow rate and the spraying gas pressure and flow rate [91, 92]. Atomization is a critical step, not only affecting the drying time and efficiency, but also controlling the particle size of the final powder [85].

3.5.1.3 Drying

After the atomization step, drying occurs through combined heat and mass transfer between the atomized droplets and the drying gas inside the drying chamber **(Figure 5c)**. The drying kinetics proceed through three successive phases: (1) the early transient period, in which heating up of the droplets takes place, (2) the constant drying rate period, where the solvent evaporates from the surface of the droplets causing the droplet diameter to

decrease at a constant rate, and (3) the falling drying rate period, in which solidification starts at the air-liquid interface after reaching the critical moisture content and evaporation continues through the shell pores [93, 94].

3.5.1.4   Powder separation

Separation of the dried powder from the drying gas stream is the last step of the spray drying process **(Figure 5d)**. Cyclone separation is the main applied technique for the recovery of spray dried powder [85, 89]. The gas stream carrying the dried particles flows from the drying chamber into the top of the cyclone in a tangential direction, creating a downward vortex along the cyclone wall. Through centrifugal forces, the particles disengage from the gas at the bottom outlet of the cyclone into the collection vessel [95]. The efficiency of separation and hence the product yield depend largely on the cyclone design and dimensions in relation to the size range of the dried particles [89].
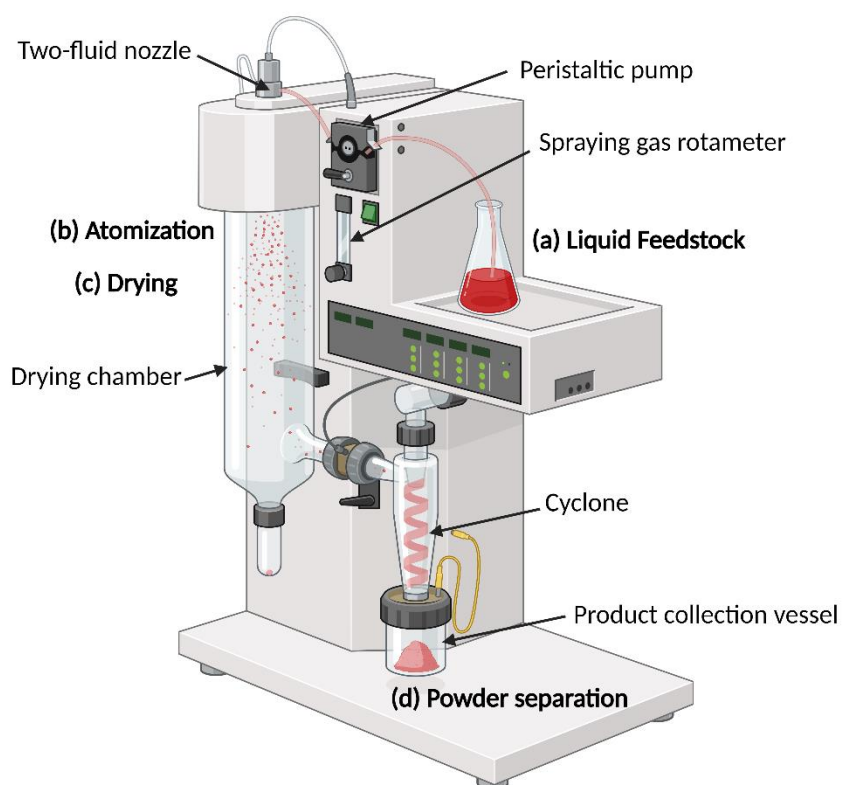
Figure 5. Illustration of Büchi B-290 Mini Spray Dryer showing the steps of spray drying process and the corresponding spray dryer main components. This figure was created with BioRender.com.

3.5.2 Particle formation

During the drying process, solutes and other solid components within the droplet are redistributed according to their physicochemical properties. The ongoing solvent evaporation at the droplet surface increases the local solute concentration. This developed concentration gradient between the surface and center of the droplet triggers the inward diffusion of the solute. The component redistribution and its effect on particle formation is described by the Peclet number (Pe): a dimensionless mass transport number which relates the solvent evaporation rate to the diffusion constant of the components [96-98].

$$Pe = \frac{\tau_{diff}}{\tau_{dry}} = \frac{R^2}{\tau_{dry}D_i} = \frac{\kappa}{8D_i} \qquad \textbf{Equation 1}$$

where τ_{diff} is the time required for a substance to move from the external interface to the center of a drying droplet, τ_{dry} is the droplet drying time, R is the droplet radius, D_i is the diffusion coefficient of dissolved or suspended components, and κ is the evaporation rate.
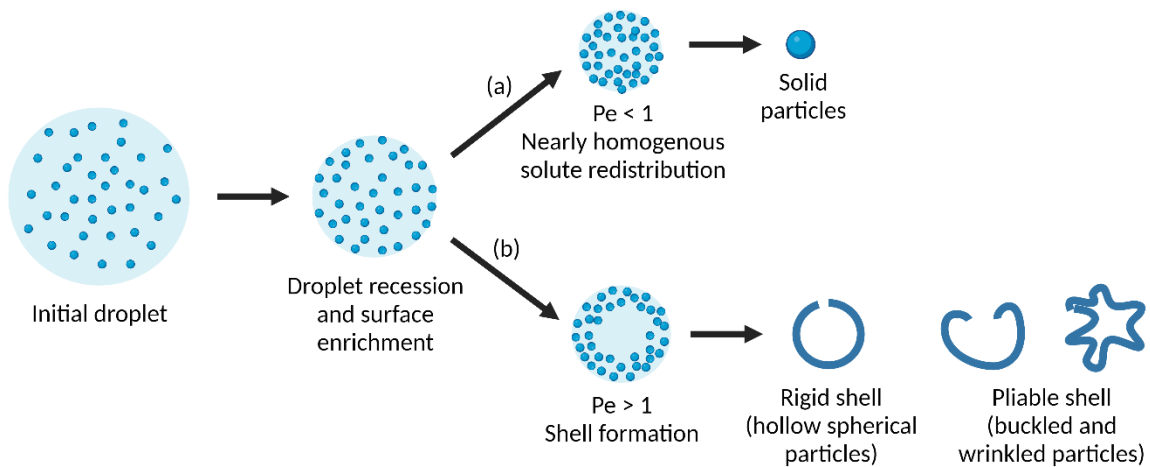
Figure 6. Particle formation mechanisms showing (a) low Peclet number and (b) high Peclet number particle formation and their different resulting particle morphologies. This figure was created with BioRender.com.

When Pe is smaller than unity **(Figure 6a)**, this means that the diffusional movement of the solutes is fast relative to the droplet surface recession due to solvent evaporation. Particles formed at Pe < 1 are characterized by spherical solid morphology with minimal

or no voids. On the other hand, a Pe larger than unity **(Figure 6b)** indicates slow diffusion of the solutes or suspended particles, accompanied by high surface enrichment and shell formation. Particles formed at Pe > 1 exhibit a range of morphologies based on their diameters and the shell properties at the terminal drying stages. If the shell solidifies quickly, solid hollow spheres are most likely to form. In contrast, viscoelastic or pliable shells undergo buckling or folding, leading to the formation of wrinkled, corrugated, or collapsed particles [96, 99, 100].

3.5.3 Influence of physicochemical properties of particle constituents

The physicochemical properties of the active ingredients and formulation additives significantly impact the final particle attributes, such as particle size, morphology, density, moisture content, and aerosol performance. Oligosaccharides (such as lactose, sucrose, and trehalose) and sugar alcohols (such as mannitol) are common matrix forming agents and fillers for spray dried particles. Due to their small molecular weight and high water solubility, they are characterized by high diffusion coefficients and hence, low Pe particle formation. On the contrary, high molecular weight excipients (such as proteins and polymers), as well as nanoparticles in general, have lower diffusion coefficients and favor the formation of high Pe hollow particles [85, 96, 101]. Leucine, a typical surface modifying agent, is a hydrophobic amino acid with a hydrophilic side chain. The amphiphilic leucine molecules accumulate at the droplet surface, producing a hydrophobic outer shell, that shrivels during drying yielding characteristic wrinkled particles [85, 102]. In addition to solubility, molecular weight and surface properties, glass transition temperature (T_g) is another critical parameter to be taken into account. Spray drying at temperatures higher than the T_g of a substance converts it to the rubbery state, leading to stickiness, material loss, and low production yields [103]. Therefore, understanding the key influencing parameters enables the production of particles with engineered properties.

3.5.4 Effect of particle properties on aerosol performance and powder formulation characteristics

The aerodynamic properties of the particles and hence their pulmonary deposition, are influenced by their size, shape and density as elaborated in **equation 2**.

$$D_{ae} = D_{geo} \sqrt{\frac{\rho_p}{\rho_0 X}} \qquad \textbf{Equation 2}$$

where D_{ae} is the aerodynamic diameter, D_{geo} is the geometric diameter, ρ_p is the particle density, ρ_0 is the unit density and X is the shape factor.

Therefore, hollow particles have lower densities and accordingly smaller aerodynamic diameter compared to solid particles with the same geometric diameter. Wrinkles and surface corrugations raise the shape factor of the particles, decrease the aerodynamic diameter, and improve pulmonary deposition. Furthermore, they increase the interparticle separation distance, decrease the interparticle surface forces, and improve the powder flowability as a result. Spherical particles have minimal contact areas and hence weaker interparticle adhesion compared to non-spherical counterparts. The presence of an outer hydrophobic layer (as in the case of leucine) reduces solid bridge formation between the particles as well as the surface forces, thereby improving the powder flowability and enhancing the physical stability through anti-hygroscopic effects [85, 104]. By controlling the interdependent aforementioned attributes, spray dried powder formulations with the desired features can be developed.

Aim of work

4. Aim of work

Exploiting the pulmonary route for the delivery of chemotherapeutics allows for more efficient localized delivery to the lungs with less undesirable systemic exposure. This would promote the therapeutic effectiveness of treatment and help reduce the toxic side effects, commonly experienced by lung cancer patients undergoing intravenous chemotherapy. In this context, this thesis aims to design an inhalable nano-structured microparticulate formulation and propose it as a potential delivery system for lung cancer.

In order to realize this, the first objective is to optimize the formulation on the nanoscale. The nanoparticle domain of the formulation is effectively responsible for the delivery of a chemotherapeutic agent to cancer cells. Importantly, the nanoparticles should be inherently non-toxic and metabolically biodegradable. Of specific relevance to cancer nanotherapeutics, acid-degradable nanoparticles would selectively release the loaded drug in acidic conditions, as in the case of the acidic tumor microenvironment or the lysosomal compartments of cancer cells. This would enable the tumor specific extracellular or the intracellular delivery of chemotherapeutics, governed by both the degradation and the cellular uptake kinetics. The nanoparticle compartment and its related aspects are addressed in the first two chapters as follows:

Chapter I: Synthesis and characterization of acetalated maltodextrin (AcMD), in which naturally abundant maltodextrin was chemically modified into hydrophobic acid degradable AcMD by conducting the following:

- Acetalation of water-soluble maltodextrin of different dextrose equivalent values into hydrophobic AcMD with different molecular weights.
- Quantification of the cyclic and acyclic acetal modification content by varying the reaction time.
- Further characterization of the AcMD polymers regarding their thermal decomposition and glass transition temperature.

Chapter II: Preparation, characterization, and cellular interaction of acetalated maltodextrin (AcMD) nanoparticles, where it focuses on the production of nanoparticles from AcMD and their features by addressing the following points:

- Investigating the key factors affecting the particle formation by nanoprecipitation and optimizing the particle production protocol to produce uniform nanoparticles with high production yields.
- Loading the AcMD nanoparticles with a hydrophobic model drug: resveratrol, and quantification of drug loading and entrapment efficiency percentages.
- Studying the AcMD nanoparticle degradation and *in vitro* release in physiological and acidic pH media (pH 7.4 and pH 5.0, respectively).
- Evaluation of cell viability after incubation with AcMD nanoparticles with human lung adenocarcinoma A549 cells and differentiated THP-1 monocytes, as well as their cellular uptake at different time points.

The second objective is to deliver the AcMD nanoparticles to the alveolar and bronchiolar compartments of the lungs, where the tumor masses develop in adenocarcinoma; the most common subtype of non-small cell lung cancer. This necessitates embedding the nanoparticles into microparticles with more favorable aerodynamic deposition. Exhibiting both features of the desired mass median aerodynamic diameter (MMAD from 0.5 to 5 μm) and sufficient redispersibility would enable the inhaled particles to bypass the two main barriers in pulmonary delivery, i.e., mucociliary clearance (through alveolar deposition) and extensive phagocytosis (through micro-to-nano transformation), respectively. Solid tumors set an additional barrier against intratumoral drug delivery, namely the dense extracellular matrix, which hinders the penetration and diffusion of therapeutic agents. Hence, collagenase was added to the microparticle matrix as an extracellular matrix modulator to enhance the nanoparticle intratumoral penetration. The formulation on the microscale is addressed in the second two chapters as follows:

Chapter III: Preparation and characterization of extracellular matrix (ECM)-modulating nano-structured microparticles, in which the AcMD nanoparticles were spray dried into microparticles comprising collagenase. Through this chapter, the following points were tackled:

- Optimizing the spray drying conditions and the formulation composition to produce AcMD nano-structured microparticles containing collagenase.
- Evaluation of the enzymatic activity of collagenase after spray drying.
- Characterization of the particle size, morphology, redispersibility into nanoparticles, residual moisture content after spray drying, as well as their aerodynamic properties.

Chapter IV: *In vitro* **tumor spheroid model for the evaluation of particle penetration,** which encompasses the following points:

- Evaluating the effect of the AcMD nano-structured microparticles containing increasing content of collagenase on human lung adenocarcinoma A549 cells and human fetal lung MRC-5 fibroblasts cell viability.
- Development of a three-dimensional lung cancer spheroid model, using a co-culture of lung adenocarcinoma A549 epithelial cells as the target cells, and MRC-5 fibroblasts as ECM secreting cells.
- Studying the effect of the collagenase loaded formulations on the spheroid integrity.
- Assessing the impact of collagenase on the AcMD nanoparticle penetration into the spheroid model.

Chapter I

Synthesis and characterization of acetalated maltodextrin (AcMD)

5. Chapter I: Synthesis and characterization of acetalated maltodextrin (AcMD)

5.1 Introduction

Polysaccharides represent a main class of natural polymers that have been growingly investigated for drug delivery and biomedical applications [105, 106]. They combine multiple merits such as high stability, safety, biocompatibility, and biodegradability [107, 108]. Moreover, they have sustainable and naturally abundant resources with low processing costs, rendering them environmentally and economically favorable materials [107, 109]. Maltodextrin (MD) is a polydisperse starch hydrolysate composed of dextrose monomers connected by α-glucosidic linkages. It is available in different grades classified according to the dextrose equivalent (DE) in the range from 3 to 20. The DE indicates the reducing power of MD, i.e., the content of reducing sugars. Hence, it is inversely proportional to the chain length and consequently the molecular weight [110, 111]. MD-based nanoparticles (NPs) have been reported in literature for several applications, for instance, crossing the blood brain barrier [112], nasal mucosal delivery [113, 114], protein/peptide delivery [111, 114], nanotheranostic agents for arterial disease [115] and thrombosed vessels [116], and vaccine delivery [117].

Stimuli-responsiveness is a frequently utilized approach to enhance the efficacy of drug delivery systems. Among these stimuli is the pH, where extracellular acidosis in case of inflamed tissues and solid tumors (pH: 5.7 - 7.0) [118] and the innately acidic environment (pH: 5.0 - 5.5) of late endosomes and lysosomes [119], compared to the normal physiological pH (7.4), constitute attractive targets for site specific drug release. Acetal formation reaction, i.e., acetalation, is a well-established method employed for hydroxyl group-containing compounds or polymers in this context [120, 121]. Acetal linkages are prone to acid mediated hydrolysis with a rate dependent on both the pH and the type of acetal, being cyclic or acyclic in conformation. Acyclic acetal linkage is less stable and hence degrades faster relative to its more stable cyclic counterpart, which can be formed when a second adjacent hydroxyl group is available for reaction [122].

Though only introduced in 2008 [121], acetalated dextran has proven to be successful for nanomedicine applications [123, 124]. It has been extensively utilized for nanoparticle production through single or double emulsion methods and employed for gene delivery [125, 126], vaccine delivery [127, 128], inflammation therapy [129, 130], cardiovascular diseases [131] and infectious diseases [132]; and recently through conventional nanoprecipitation [133], microfluidics [134] and electrospraying [135]. However, the particle formulation strategies were not yet systematically evaluated.

In the current work, water-soluble MD was selected to constitute a biocompatible and biodegradable polymer backbone, to which acetal moieties were built on. Through this modification, MD is hydrophobized into acetalated MD (AcMD) and attains tunable acid degradability. Fluorescently labelled AcMD was also synthesized, to be used for tracing and visualization experiments in the subsequent work packages. The acetal modification type and content were determined. The synthesized AcMD polymers were characterized for molecular weight after acetalation, as well as the thermal decomposition profiles and glass transition temperature (T_g), which are all essential characteristics to be considered upon exploiting a polymer for drug delivery system development.

5.2 Materials and methods

5.2.1 Materials

MD (DE: 4.0-7.0, 13.0-17.0 and 16.5-19.5), 2-methoxypropene, pyridinium *p*-toluene sulfonate (PPTS), triethylamine (TEA) and 1,8-diazabicyclo[5.4.0]undec-7-ene (DBU) were purchased from Sigma-Aldrich (Steinheim, Germany). NHS-rhodamine was purchased from Thermo Fisher Scientific (Darmstadt, Germany). Dimethyl sulfoxide (DMSO, analytical grade), acetone and ethanol (HPLC grade) were purchased from Fisher Scientific (Schwerte, Germany). Poly(methyl methacrylate) standards (PMMA) were purchased from Polymer Standards Service (PSS) (Mainz, Germany). All the other reagents used were purchased with HPLC or analytical grade.

5.2.2 Synthesis of acetalated maltodextrin (AcMD) with different molecular weights and cyclic/acyclic acetal ratios

AcMD was synthesized according to the method developed by Bachelder et al. [121] with slight modifications. A dry round-bottom flask was loaded with MD (1 g), purged with nitrogen and sealed. DMSO (10 ml) was added and allowed to stir till complete dissolution of MD. PPTS (15.5 mg, dissolved in 1 ml of DMSO) and 2-methoxypropene (3.6 ml) were injected into the reaction medium and the reaction was allowed to proceed for the desired reaction time (10, 30, 60 and 180 min). The reaction was then quenched with TEA (1 ml) and the product was precipitated by transferring the reaction solution to slightly alkaline water (0.004% TEA, 100 ml). The product was obtained by centrifugation at 20,000 g, 20 min, 20 °C (Multifuge X1R, Thermo Fisher Scientific, Osterode am Harz, Germany) and cross-washed through dissolution in ethanol, reprecipitation with water and centrifugation. After two additional washing cycles, the pellets were lyophilized (Alpha 3-4 LSCbasic, Christ, Osterode am Harz, Germany) and the product was collected and stored in a tightly closed container at -20 °C.

5.2.3 Synthesis of rhodamine-conjugated AcMD (Rhod-AcMD)

MD (100 mg) was dissolved in 0.5 ml of DMSO. NHS-rhodamine (10 mg, dissolved in 0.5 ml of DMSO) and 0.01 ml of DBU were added and stirred overnight at room temperature. Afterwards, the rhodamine-conjugated MD (Rhod-MD) was precipitated by adding the resulting solution into acetone (10 ml) followed by centrifugation (Multifuge X1R, Thermo Fisher Scientific, Osterode am Harz, Germany). The product was purified from the unconjugated dye through repetitive cycles (x5) of dissolution in water, reprecipitation with acetone and centrifugation. The pellets were lyophilized, and rhodamine was assayed fluorometrically ($\lambda_{ex/em}$: 565/600 nm) using microplate reader (Infinite M200, Tecan group, Männedorf, Switzerland) to determine the dye content in Rhod-MD. Finally, Rhod-MD was mixed with unlabeled MD at a concentration of 2% and acetalation was carried out as described.

5.2.4 Acetal modification analysis by ^{1}H-NMR

AcMD (12 mg) was mixed with 0.70 ml of D_2O and 0.03 ml of 38% DCl and hydrolyzed completely for 2 h prior to ^{1}H-NMR analysis (500 MHz, Avance Neo 500, TCI Prodigy CryoProbe, Bruker, Rheinstetten, Germany). The peak normalized integration of acetone, methanol and proton attached to the anomeric carbon of the glucose ring was utilized to quantify the cyclic and acyclic acetal modification content [136].

5.2.5 Molecular weight determination

Size exclusion chromatography (SEC) was performed with a system consisting of a RI Waters 2410 detector, a Waters 2487 detector working at 260 nm, two PSS GRAM 1000 columns and a PSS GRAM 30 column. Dimethyl formamide (with 1 g/l LiBr) was used as mobile phase at 1 ml/min flow rate at 60 °C and PMMA standards were used for calibration.

5.2.6 Thermogravimetric analysis (TGA)

TGA was carried out employing a thermogravimetric analyzer (TG 209 F1 Libra, Netzsch, Selb, Germany) under a nitrogen atmosphere. The analysis temperature was set from 30 to 600 °C, the heating rate was 10 °C/min and the sample masses were between 7 and 13 mg. Netzsch Proteus® Software was used to generate the thermograms and determine the onset decomposition temperature and the mass loss percentage of the investigated polymers.

5.2.7 Determination of glass transition temperature (T_g)

Differential scanning calorimetry (DSC) was carried out to measure the T_g using a differential scanning calorimeter (DSC 214 Polyma, Netzsch, Selb, Germany) with a heating rate of 10 °C/min. Netzsch Proteus® Software was used to determine the T_g of AcMD polymers.

5.3   Results and discussion

5.3.1   Synthesis of AcMD

The reaction between MD and 2-methoxypropene results in the coverage of hydroxyl groups with both cyclic and acyclic acetal groups **(Figure 7a)**. This modification reverses the solubility properties of MD and imparts to it an acid triggered degradability that can be tuned by varying the relative content of slow-degrading cyclic acetal and fast-degrading acyclic acetal groups [122, 137]. The reaction was performed using MD with DE of 4.0-7.0 (MDA), 13.0-17.0 (MDB) or 16.5-19.5 (MDC) to produce AcMD with different molecular weights or using MDB at different reaction time to obtain different cyclic/acyclic acetal ratios.

5.3.2   Synthesis of Rhod-AcMD

MD was fluorescently labeled through NHS-rhodamine conjugation **(Figure 7b)**. Adopting acetalation at a certain reaction time for this Rhod-MD after being diluted with unlabeled MD would yield the corresponding fluorescent Rhod-AcMD. The amount of rhodamine in the Rhod-MD was assayed fluorometrically ($\lambda_{ex/em}$: 565/600 nm, linearity range: 0.1 – 0.6 μg/ml, R^2: 0.9991) against MD blank and was found to be 1.49 $\pm$ 0.02%. The mass percentage of rhodamine in Rhod-AcMD was estimated, based on the dilution of labelled MD with the unlabelled MD and the molecular weight increase due to acetalation, to be 0.02%. Direct fluorometric determination of rhodamine in Rhod-AcMD yielded a lower mass content than expected, possibly due to partial fluorescence quenching by TEA in the acetalation reaction quenching step, as reported by Bakkialakshmi et al. [138]. Nevertheless, the remaining fluorescence was sufficient for visualization.
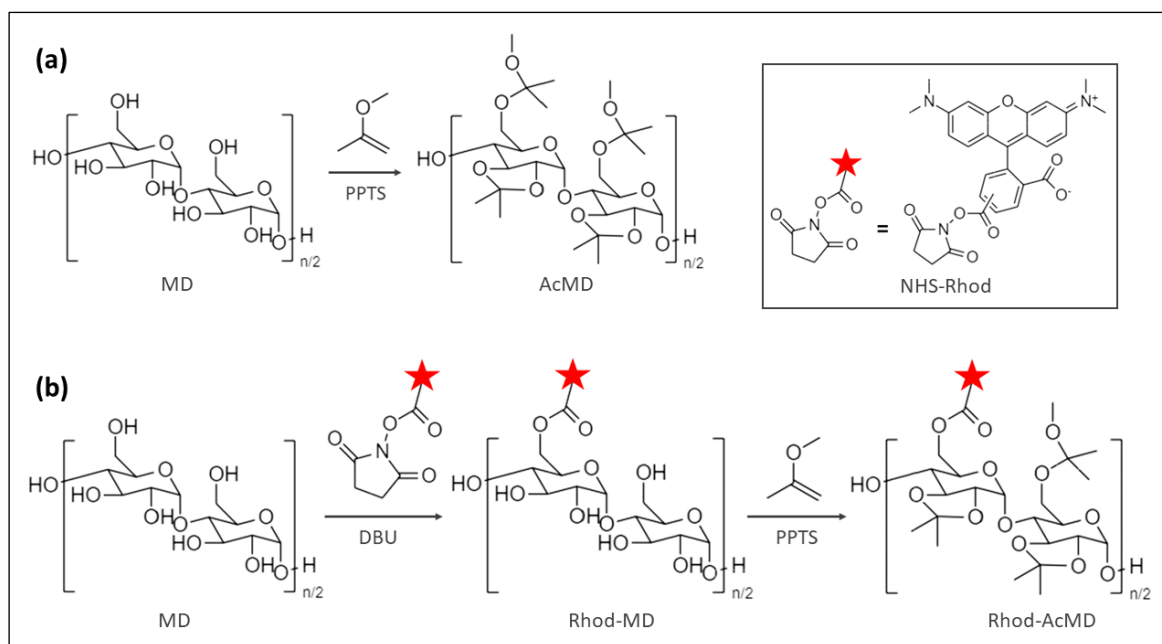
Figure 7. (a) Synthesis of AcMD using 2-methoxypropene as acetalating agent and PPTS as an acidic catalyst. (b) Fluorescent labeling of MD with NHS-rhodamine in presence of DBU as a catalyst, followed by acetalation of Rhod-MD.

5.3.3 Acetal modification analysis

Acetal functionalization could be analyzed and quantified based on the evaluation of the ^{1}H-NMR spectra of acid degraded AcMD. An example of the ^{1}H-NMR spectra for unmodified MDB and its acid degraded acetalated counterpart is shown in **figure 8**. Acetalation of MDA, MDB and MDC for 3 h lead to a cyclic acetal modification content approaching 50% **(Figure 9a)**, which is the maximum possible percentage of cyclic acetal modification for glucose subunits. Through decreasing the reaction time from 3 h to 10 min, cyclic acetal percentage decreased gradually from 46.97% (AcMDB$_{180}$) to 20.82% (AcMDB$_{10}$) as demonstrated in **figure 9b**.
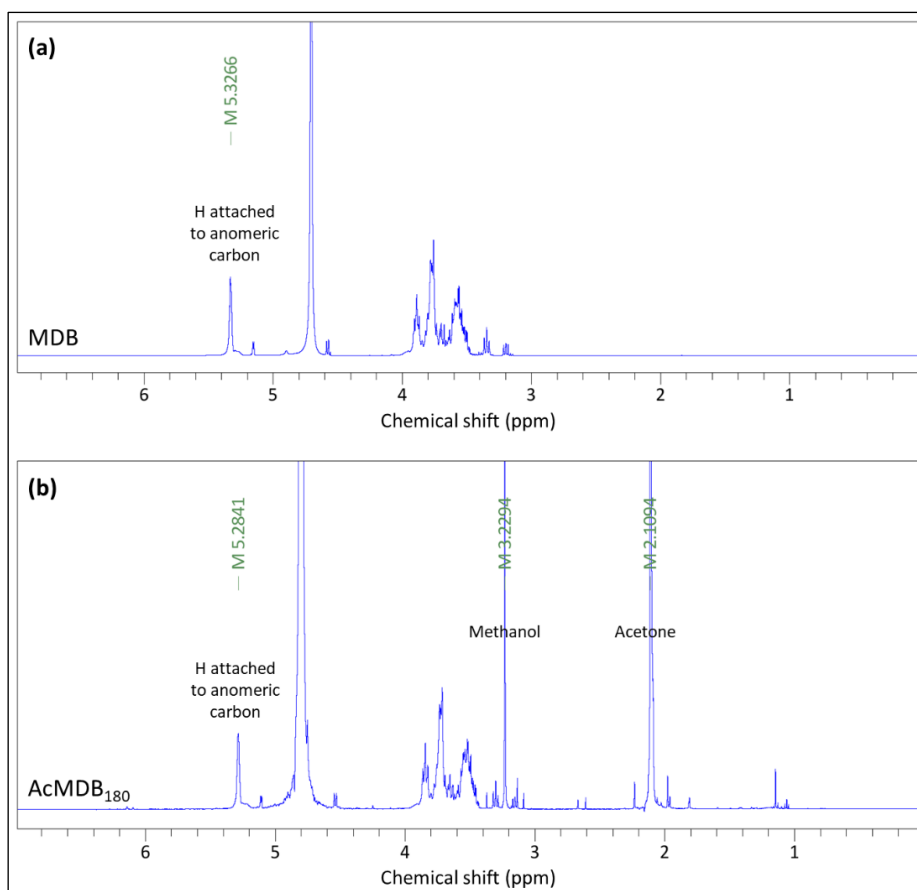
Figure 8. ^{1}H-NMR spectra of (a) unmodified MDB (D_2O, 500 MHz) and (b) acid degraded AcMDB$_{180}$ (D_2O/DCl, 500 MHz).
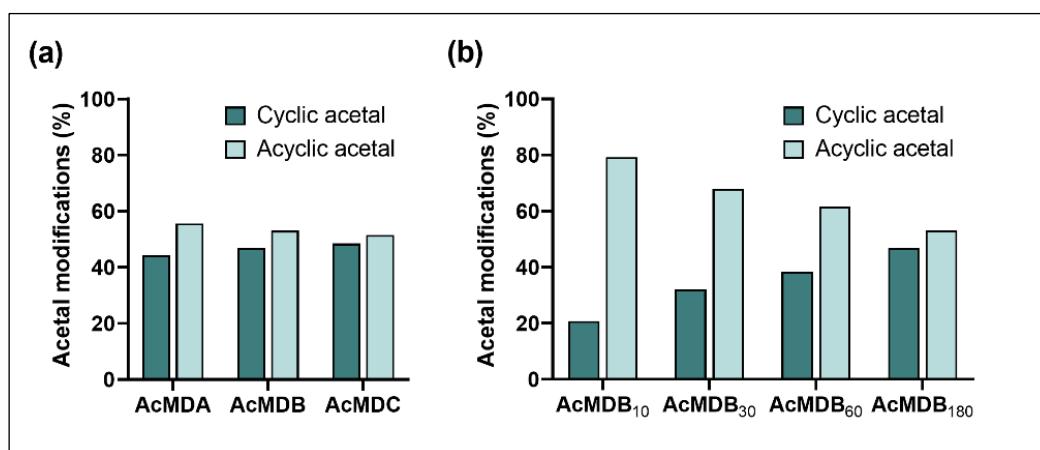
Figure 9. The percentage of cyclic and acyclic acetal modification of AcMD synthesized from (a) MDA, MDB and MDC at 3 h reaction time and (b) MDB at different reaction times (from 10 – 180 min) determined by ^{1}H-NMR analysis of the acid degraded polymers.

5.3.4 Molecular weight determination

The measured number average molecular weight (M_n), weight average molecular weight (M_w) and dispersity (Đ) for AcMD polymers are displayed in **table 1**. Expectedly, the higher the DE of MD, the lower the molecular weight of the respective AcMD. The AcMD polymers exhibited broad molecular weight distribution **(Figure 10)**, ascribed to the polydispersity of the parent MD polymers [139]. The results appear to be in a good agreement with the data reported by Castro et al. [140] for each equivalent MD, considering the assumed increase in molecular weight due to acetalation (approximately 1.7 times).

Table 1. Number average molecular weight (M_n), weight average molecular weight (M_w) and dispersity (Đ) of AcMD polymers determined by SEC using PMMA calibration standards.

Polymer	M_n (g/mol)	M_w (g/mol)	Đ
AcMDA	3114.6	52125.0	16.7
AcMDB	1556.1	8485.8	5.5
AcMDC	1547.0	7853.1	5.1
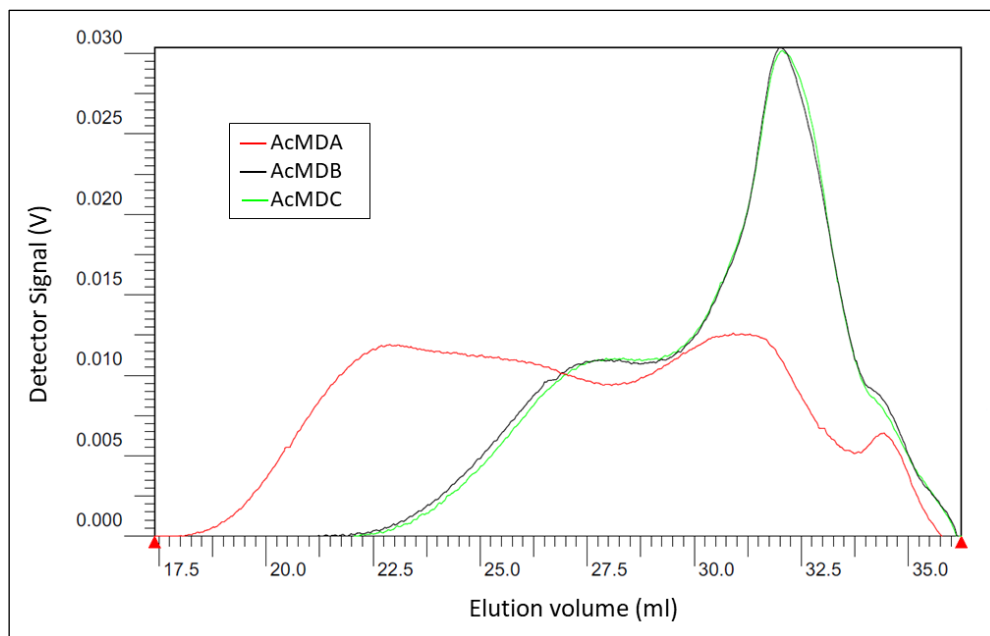
Figure 10. SEC chromatograms of AcMD polymers, determined using PMMA calibration standards.

5.3.5   Thermogravimetric analysis (TGA)

TGA was performed to evaluate the thermal stability of AcMD polymers relative to their MD counterparts. **Figure 11a** shows the MD thermograms exhibiting typical dehydration and decomposition phases, associated with minor and major mass loss respectively as reported in literature [140, 141]. On the other hand, the TGA profiles of AcMD polymers reveal a biphasic decomposition phase with a lower decomposition onset temperature **(Figure 11b)**. The first decomposition phase is speculated to be due to the degradation of the acetal moieties. The onset decomposition temperature was not in correlation with either the molecular weight or the cyclic/acyclic modification ratio **(Table 2, Figure 11b and c)**. However, comparing AcMDB polymers with different cyclic/acyclic modification ratios depicts a gradual increase in the mass loss percentage of the first degradation phase with increasing the acyclic acetal amount **(Table 2, Figure 11c)**. This suggests that the less stable acyclic acetal groups are primarily responsible for the appearance of this additional decomposition phase. The dehydration phase could not be detected in AcMD polymers profiles, indicating the elimination of the residual moisture at the lyophilization step of the polymer synthesis.
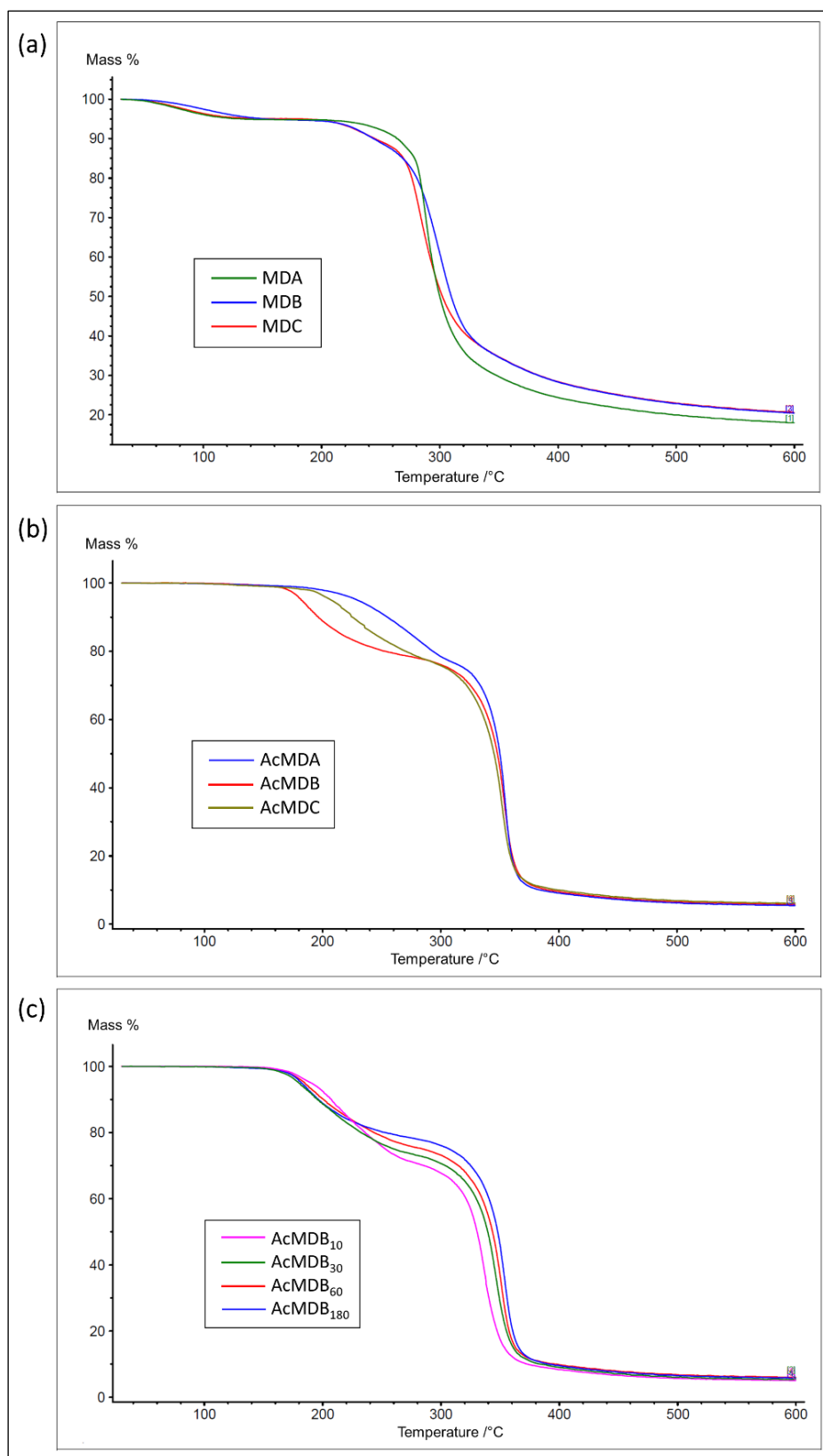
Figure 11. TGA thermograms of (a) MD polymers with different DE, (b) the corresponding AcMD polymers and (c) AcMDB prepared at different reactions times resulting in different cyclic/acyclic acetal ratios.

Table 2. Onset decomposition temperature (T_{onset}), mass loss percentage and glass transition temperature (T_g) of AcMD polymers having different molecular weights and cyclic/acyclic acetal ratios.

Polymer	T_{onset} (°C)	Mass loss[1] (%)	Mass loss[2] (%)	T_g (°C)
AcMDA$_{180}$	121.2	23.0	71.2	99.7
AcMDB$_{10}$	130.1	29.7	65.2	60.1
AcMDB$_{30}$	129.5	26.5	67.9	83.1
AcMDB$_{60}$	123.4	24.4	69.4	97.4
AcMDB$_{180}$	114.7	21.7	72.4	81.8
AcMDC$_{180}$	113.1	21.9	71.6	63.4

[1] Mass loss percentage of the first decomposition phase

[2] Mass loss percentage of the second decomposition phase

5.3.6 Determination of glass transition temperature (T_g)

The polymer T_g depends on the mobility and flexibility of polymer chains, where both the polymer backbone and the side groups are involved [142, 143]. According to the DSC results shown in **table 2** and **figure 12**, AcMD polymers exhibited lower T_g values, compared to the T_g values reported for MD by Avaltroni et al. and Siemons et al. [110, 139]. Introducing acetal groups to the polymer chains was anticipated to be accompanied by an increase in the T_g. However, the expected steric effect was probably opposed by masking of the hydroxyl groups, which were thought to contribute to the higher T_g of the MD through intra- and inter-molecular hydrogen bonding [144].
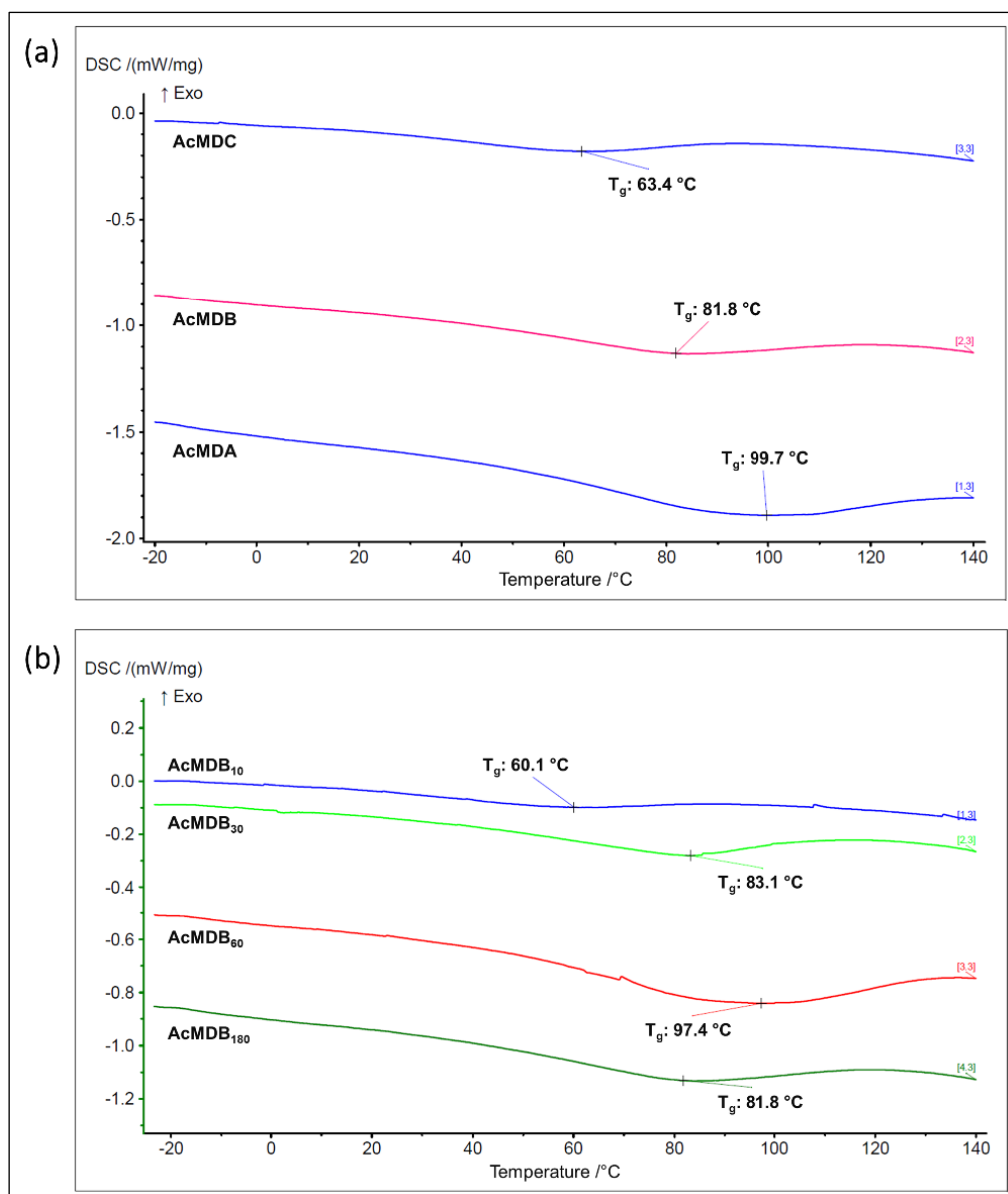
Figure 12. DSC thermograms of AcMD polymers with (a) different molecular weights and (b) different cyclic/acyclic acetal ratios, showing their T_g.

5.4 Conclusion

Through acetalation, water-soluble MD was modified into hydrophobic AcMD. The AcMD polymers exhibited broad molecular weight distributions, inherited from the precursor MD. This may affect the particle formation process or the dispersity of the formed particles. AcMD polymers of different cyclic/acyclic acetal ratios were produced, which can be used to produce particles with different degradation kinetics. The different synthesized AcMD polymers were found to have lower decomposition onset temperature and lower T_g

compared to the corresponding MDs. This should be considered upon using AcMD for different applications, in which high temperatures are required during preparation and/or processing. To this end, AcMD of different molecular weights and cyclic/acyclic modification ratios was prepared, of which the nanoparticle formation and characteristics would be studied in the following chapter.

Chapter II

Preparation, characterization, and cellular interaction of acetalated maltodextrin (AcMD) nanoparticles

6. Chapter II: Preparation, characterization, and cellular interaction of acetalated maltodextrin (AcMD) nanoparticles

6.1 Introduction

Nanomedicine has proven its potential to circumvent the treatment inconveniences that are usually encountered with chemotherapy, where using nanosystems as carriers for chemotherapeutic agents has multiple advantages compared to the conventional intravenous administration [145]. Nanovehicles could improve the pharmacokinetics of the poorly water-soluble anticancer drugs and protect them against pre-mature metabolism or inactivation [146]. Additionally, they might enable passive or active targeted delivery to the tumor sites and accordingly limit the unwanted systemic side effects and toxicities [147]. Nanosystems allow the multiple delivery of synergistic agents in the same cargo, which could maximize the treatment efficacy [148, 149]. Loading anticancer drugs on nanocarriers could evade the efflux transporters, involved in multi-drug resistance, through nanoparticle-mediated cellular uptake [150]. Therapeutic nanoparticles (NPs) must be non-toxic and biodegradable to avoid the unwanted accumulation upon repetitive administration. Therefore, natural lipid- and polymer-based nanocarriers have been extensively applied in anticancer delivery systems [145].

Polymeric NPs could be produced by several methods including emulsification, nanoprecipitation, coacervation and supercritical fluid technology [151-153]. Nanoprecipitation, also known as inverse precipitation, desolvation or solvent displacement, is a versatile method implying the addition of polymer solution to a miscible non-solvent system or vice versa, with or without the use of a stabilizer. Nanoparticle formation occurs through sequential steps of supersaturation, nucleation, particle growth and aggregation [154, 155]. The colloidal properties of the produced particles are governed by a vast range of factors such as polymer concentration, polymer saturation solubility in solvent and antisolvent, solvent-antisolvent interaction, stabilizer effect, volume ratio, sequence of addition, mixing conditions and temperature [154-156]. However, proper selection of the key influencing parameters provides good control over the production process, resulting in reproducible formation of nano-sized particles with narrow size

distribution. Furthermore, nanoprecipitation is the principal technique from which more recent technologies emerged namely, microfluidic-based nanoprecipitation [157] and flash nanoprecipitation [158], offering better process manipulation, higher reproducibility and potential for scaling-up [155, 159-161].

In the current study, the nanoprecipitation-based particle formation process of acetalated maltodextrin (AcMD) and the key influencing factors were studied. The loading of AcMD-NPs with resveratrol as a model hydrophobic molecule, their acid induced degradability, and *in vitro* release from the loaded NPs were investigated. Biocompatibility of AcMD-NPs with human adenocarcinoma lung epithelial A549 cells and differentiated human macrophage-like THP-1 (dTHP-1) cells was assessed, as examples for somatic and immune cells, respectively. Finally, cell internalization of AcMD-NPs with the aforementioned cells was traced at different time points. To this end, the aim of this work is to propose a well-defined protocol for the production of acid responsive AcMD-NPs which were not addressed before, and to provide a basic framework for their efficient implementation in drug delivery applications in general and anticancer drug delivery in particular.

6.2 Materials and methods

6.2.1 Materials

Maltodextrin (DE: 4.0-7.0, 13.0-17.0 and 16.5-19.5), 2-methoxypropene, pyridinium *p*-toluene sulfonate (PPTS), triethylamine (TEA), 1,8-diazabicyclo[5.4.0]undec-7-ene (DBU), polyethylene glycol 400 (PEG-400), RPMI-1640 cell culture medium, Dulbecco's phosphate buffered saline (DPBS), phorbol 12-myristate 13-acetate (PMA), trypsin-EDTA, penicillin-streptomycin and thiazolyl blue tetrazolium bromide were purchased from Sigma-Aldrich (Steinheim, Germany). Poloxamer 407 was purchased from Caesar and Loretz GmbH (Hilden, Germany). NHS-rhodamine, 4′,6-diamidino-2-phenylindole (DAPI) and Alexa Fluor™ 488 conjugate of Concanavalin A were purchased from Thermo Fisher Scientific (Darmstadt, Germany). Resveratrol was purchased from Carl Roth (Karlsruhe, Germany). Fetal calf serum (FCS) was purchased from Lonza (Basel, Switzerland). Dimethyl sulfoxide (DMSO, analytical grade), acetone and ethanol (HPLC grade) were purchased from Fisher

Scientific (Schwerte, Germany). All the other reagents used were purchased with HPLC or analytical grade.

6.2.2 Synthesis of AcMD

AcMD of different molecular weights (AcMDA, AcMDB and AcMDC) and different cyclic/acyclic acetal ratios (AcMDB$_{10}$, AcMDB$_{30}$, AcMDB$_{60}$ and AcMDB$_{180}$) were prepared as described in **chapter I, section 5.2.2**. Fluorescently labeled AcMD with lowest and highest cyclic acetal content (Rhod-AcMDB$_{10}$ and Rhod-AcMD$_{180}$) were prepared as described in **chapter I, section 5.2.3**.

6.2.3 Preparation of AcMD-NPs

The preparation procedure is based on the nanoprecipitation method originally introduced by Fessi et al. [162]. AcMD was dissolved in acetone to yield mass concentrations of 10, 25 and 50 mg/ml. The resulting solution (1 ml) was injected using a syringe pump (PHD 2000, Harvard Apparatus, Massachusetts, United States) into 0.5% poloxamer 407 aqueous solution (5 ml) at a rate of 1 ml/min under mild stirring. The formulations were left stirring for 3 h for acetone evaporation, as comparative amounts of acetone for nanoprecipitation procedures in general was found to be evaporated during the first hour. The produced NPs were purified through two cycles of centrifugation at 10,000-12,000 g, 20 min, 20 °C (Multifuge X1R, Thermo Fisher Scientific, Osterode am Harz, Germany), removal of supernatant and addition of fresh slightly alkaline water.

Resveratrol loaded AcMD-NPs were prepared following the same procedure at 25 mg/ml polymer mass concentration with addition of resveratrol (5% of the polymer mass) to the polymer solution. Fluorescent AcMD-NPs were prepared using Rhod-AcMD and the procedure was continued as described. All the formulations were prepared in triplicates.

6.2.4 Characterization of AcMD-NPs
6.2.4.1 Particle diameter, polydispersity index (PDI) and zeta potential

Particle size and zeta potential of AcMD-NPs were measured using dynamic light scattering (DLS) and laser doppler electrophoresis (Zetasizer Ultra, Malvern Panalytical,

Worcestershire, United Kingdom), respectively. Samples were diluted with 5 mM KCl solution to an approximate nanoparticle concentration of 0.05 mg/ml and 1 ml was placed in a zeta potential folded cuvette. Intensity-based hydrodynamic diameter measurement was performed at 25 °C with an angle of 173° in the back scattering mode. Zeta potential was measured based on electrophoretic mobility at 25 °C. The measurements were performed in triplicates.

6.2.4.2 Particle morphology using scanning electron microscope (SEM)

AcMD-NPs were visualized using SEM (Zeiss EVO HD15, Carl Zeiss, Oberkochen, Germany). A sample volume of 10 μl was placed on a silica waver fixed onto a metal stub. After 5 minutes, excess liquid was removed, and samples were air dried. The particles were sputter coated with 10 nm gold layer (Quorum Q150R ES, Quorum Technologies, East Sussex, United Kingdom) and examined at 20 kV under high vacuum conditions.

6.2.4.3 Entrapment efficiency (EE%) and drug loading (DL%)

A sample aliquot of 1 ml was washed twice using centrifugation at 40,000 g, 30 min, 20 °C (Sigma 3-30KS, Sigma, Osterode am Harz, Germany). Subsequently, the pellets were lyophilized (Alpha 3-4 LSCbasic, Christ, Osterode am Harz, Germany), and pellet masses were determined. The pellets were then dissolved using acetonitrile and loaded resveratrol was directly quantified through measuring its absorbance (λ_{max}: 308 nm) using UV-Star® 96 well F-bottom plates (Greiner Bio-One, Frickenhausen, Germany) and microplate reader (Infinite M200, Tecan group, Männedorf, Switzerland). The EE% and DL% were determined by calculating the percentage of loaded resveratrol relative to total added resveratrol or total mass of loaded NPs, respectively, as follows:

$$EE\% = \frac{Amount\ of\ loaded\ resveratrol\ (\mu g)}{Total\ amount\ of\ resveratrol\ added\ (\mu g)} \times 100 \qquad \text{Equation 3}$$

$$DL\% = \frac{Amount\ of\ loaded\ resveratrol\ (\mu g)}{Mass\ of\ loaded\ NPs\ (\mu g)} \times 100 \qquad \text{Equation 4}$$

6.2.5 Nanoparticle degradation experiments

AcMD-NPs were suspended in either phosphate buffered saline (PBS pH 7.4) or 0.1 M acetate buffer (pH 5.0) at 4 mg/ml particle concentration and incubated at 37 °C with agitation (Shaking incubator 3031, GFL, Burgwedel, Germany). At previously specified time points, 0.4 ml samples were withdrawn and centrifuged at 40,000 g, 15 min, 20 °C (Sigma 3-30KS, Sigma, Osterode am Harz, Germany) to separate the undegraded NPs. The supernatants were collected and stored at -20 °C till being analyzed for reducing sugars using BCA reductometric assay (QuantiPro™ BCA Assay Kit, Sigma-Aldrich, Taufkirchen, Germany) according to the manufacturer's protocol [122, 137]. All the experiments were carried out in triplicates.

6.2.6 *In vitro* release studies

Resveratrol-loaded AcMD-NPs were suspended in release media at 2 mg/ml concentration and incubated at 37 °C with agitation. The release medium was either PBS (pH 7.4) or 0.1 M acetate buffer (pH 5.0) to which PEG-400 was added at a concentration of 5% to achieve sink conditions, where PEG-400 was reported to be a superior solubilizing agent for resveratrol [163]. Samples (0.4 ml) were withdrawn at specified time intervals and centrifuged at 40,000 g, 15 min, 20 °C (Sigma 3-30KS, Sigma, Osterode am Harz, Germany). The released resveratrol in the separated supernatants was assayed as described in **section 6.2.4.3**. All the experiments were performed in triplicates.

6.2.7 *In vitro* biological experiments

6.2.7.1 Cell culture

Adenocarcinoma human alveolar epithelial cells (A549) and acute leukemia human monocytic cells (THP-1) were cultured in RPMI-1640 medium supplemented with 10% FCS. The cells were subcultured once a week and fresh media was applied twice a week. The cultures were maintained in a humidified incubator at 37 °C under 5% CO_2 atmosphere. Both cell lines were used within consecutive passages not later than passage 20.

6.2.7.2 Cell viability

The cytotoxicity and biocompatibility of AcMD-NPs were evaluated using MTT assay on A549 and dTHP-1 cells. A549 cells were seeded into a 96-well plate (10,000 cells/well) and grown for 48 h. THP-1 cell number was adjusted to 80,000 cells/well and PMA was added at a concentration of 30 ng/ml [164, 165]. The THP-1 cells were directly seeded and cultured for 48 h to allow for differentiation. Subsequently, old media were replaced with fresh media containing the tested AcMD-NPs at different concentrations (50, 100, 250, 500, 750 and 1000 μg/ml) and supplemented with 100 U/ml penicillin-streptomycin. Samples were tested against negative (live) and positive (dead) controls, where cells were treated with medium and 2% Triton-X, respectively. After 24 h incubation with the formulations, media were removed, cells were washed with DPBS and incubated with 10% MTT reagent (diluted in DPBS) for 4 h. This was followed by aspiration and incubation with DMSO for 20 min. Absorbance of formed formazan by live cells (OD) was measured at 550 nm and cell viability was calculated according to **equation 5**. The experiments were performed at least in triplicates.

$$\textit{Cell viability} \; (\%) = \frac{OD_{sample} - OD_{positive\;control}}{OD_{negative\;control} - OD_{positive\;control}} \times 100 \qquad \textbf{Equation 5}$$

6.2.7.3 Cellular interaction

A549 cells were seeded (20,000 cells/well) in 8-well imaging chamber (Ibidi, Gräfelfing, Germany) and grown for 48 h. THP-1 cells were seeded (80,000 cells/well) after being differentiated as previously mentioned. Afterwards, old media were aspirated and replaced with fresh media containing Rhod-AcMD-NPs at 1000 μg/ml concentration and supplemented with 100 U/ml penicillin-streptomycin. As negative control, cells were treated with plain medium. After incubation at 2, 4 and 24 h, media were aspirated, and cells were washed twice with DPBS. Fixation was carried out using 3% paraformaldehyde for 30 min at room temperature. Nuclei were stained using 3 nM DAPI for 20 min and cell membranes were stained using 5 μg/ml Concanavalin A Alexa Fluor™ 488 conjugate for 30 min. Cells were washed twice with DPBS after fixation and staining steps and stored in DPBS at 4 °C until examination.

Cell visualization for uptake evaluation was performed through confocal laser scanning microscope (CLSM) (LSM 710, Carl Zeiss AG, Jena, Germany) using 40x water immersion objective. The signals of DAPI, Alexa Fluor™ 488 and rhodamine were detected through excitation at 405, 488 and 561 nm and recording emission at 410-507, 496-603 and 566-703 nm, respectively. Recorded images from individual channels were merged. Image processing was performed using ZEN 3.0 (blue edition) software (Carl Zeiss Microscopy, 2019).

6.2.8 Statistical analysis

The results are expressed as mean $\pm$ standard deviation of the performed replicates. Statistical significance was tested using one-way or two-way analysis of variance (ANOVA) in case of one or two independent variables, respectively, followed by Tukey *post hoc* test to compare all pairs. The level of significance was set at a *p*-value of 0.05. Statistical analysis was implemented using GraphPad Prism (version 8.0.2) software (GraphPad Software, 2019).

6.3 Results and discussion

6.3.1 Preparation of AcMD-NPs

NPs of variable particle diameters and homogenous size distribution were prepared using one-step nanoprecipitation method with acetone as organic solvent and poloxamer 407 as stabilizer. Additionally, the high yield of produced NPs relative to the used polymer mass denotes the efficiency of preparation **(Figure 13)**. It is worth mentioning that other solvent/antisolvent volume ratios, injection rates, organic solvents (ethanol, isopropanol and DMSO), and stabilizers (polyvinyl alcohol (PVA), poloxamer 188 and tween 80) were also preliminarily investigated but the selected system was found to be superior in terms of the quality of particles, ease of purification and/or their physical stability in different buffered systems used later in the study (results not shown).
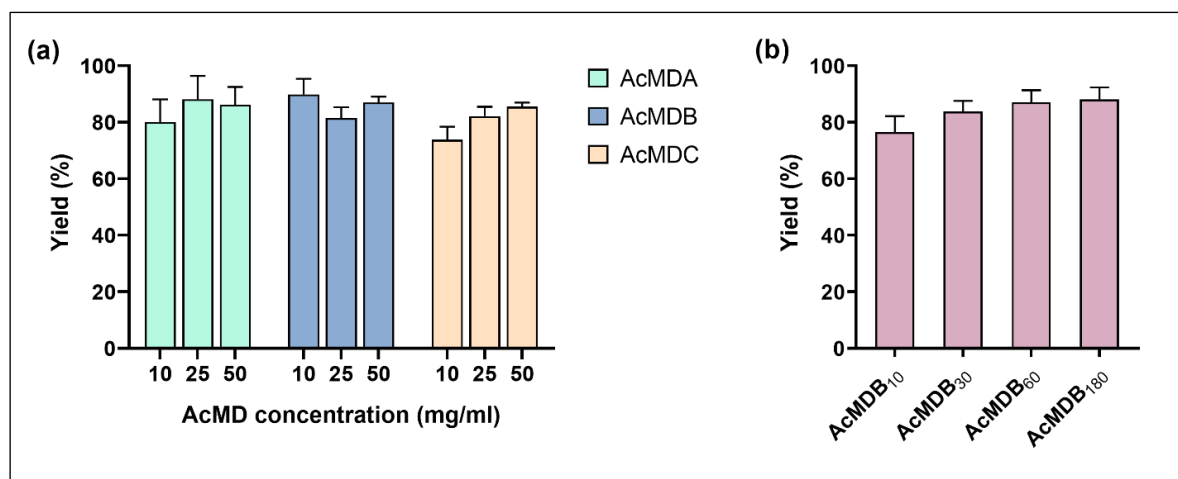
Figure 13. Nanoparticle production yield of (a) plain AcMD-NPs prepared at different polymer molecular weights and polymer solution mass concentrations (10, 25 and 50 mg/ml) and (b) resveratrol-loaded AcMDB-NPs prepared from AcMD with different cyclic/acyclic ratios at 25 mg/ml mass concentration. The results are mean values ± standard deviation from n = 3 independent experiments.

6.3.2   Characterization of AcMD-NPs

6.3.2.1   Particle size, PDI and zeta potential

Plain NPs were prepared using AcMDA, AcMDB and AcMDC at different polymer concentrations. The particle size varied significantly depending on both mass concentration **(Figure 14a)** and molecular weight **(Figure 14b)** of AcMD. Increasing the polymer mass concentration from 10 to 50 mg/ml resulted in a clear increase in particle size. This was expected due to higher nucleus collision frequency and hence an increased growth during particle formation [154]. Additionally, increasing the concentration may also be accompanied by an increase in viscosity, which in turn hinders the diffusion of the solvent within the antisolvent phase, causing less uniform supersaturation, slower nucleation rates, increased agglomeration and accordingly larger particles [166]. The effect of molecular weight can be attributed either to (a) viscosity effect, in case of AcMDA compared to its counterparts, or (b) higher supersaturation and therefore enhanced nucleation and smaller particles in case of AcMDB compared to AcMDC [154].

Except for NPs prepared with AcMDA at 50 mg/ml mass concentration, monodisperse NPs were produced with PDI values ranging from 0.016 to 0.051 **(Figure**

14a). The observed increase in PDI in the earlier case would be ascribed to the combined effect of increasing both molecular weight and mass concentration. This would negatively impact the efficiency of mixing and the homogeneity of supersaturation, causing increased agglomeration and less uniform particle formation. All the particles exhibited a very slight negative zeta potential ranging from -0.74 to -2.40 mV **(Figure 15)**, due to the coverage of the negative hydroxyl groups through acetalation.

AcMDB polymers of different cyclic/acyclic acetal ratio were then used to produce resveratrol-loaded NPs. Loading with resveratrol lead to a slight increase in particle diameter and did not affect the particle uniformity as shown in **figure 14c**. Furthermore, the variation in cyclic/acyclic acetal modification did not significantly affect the particle diameter. All particles prepared had sizes between 179 – 185 nm and very low PDI values in between 0.029 – 0.043.
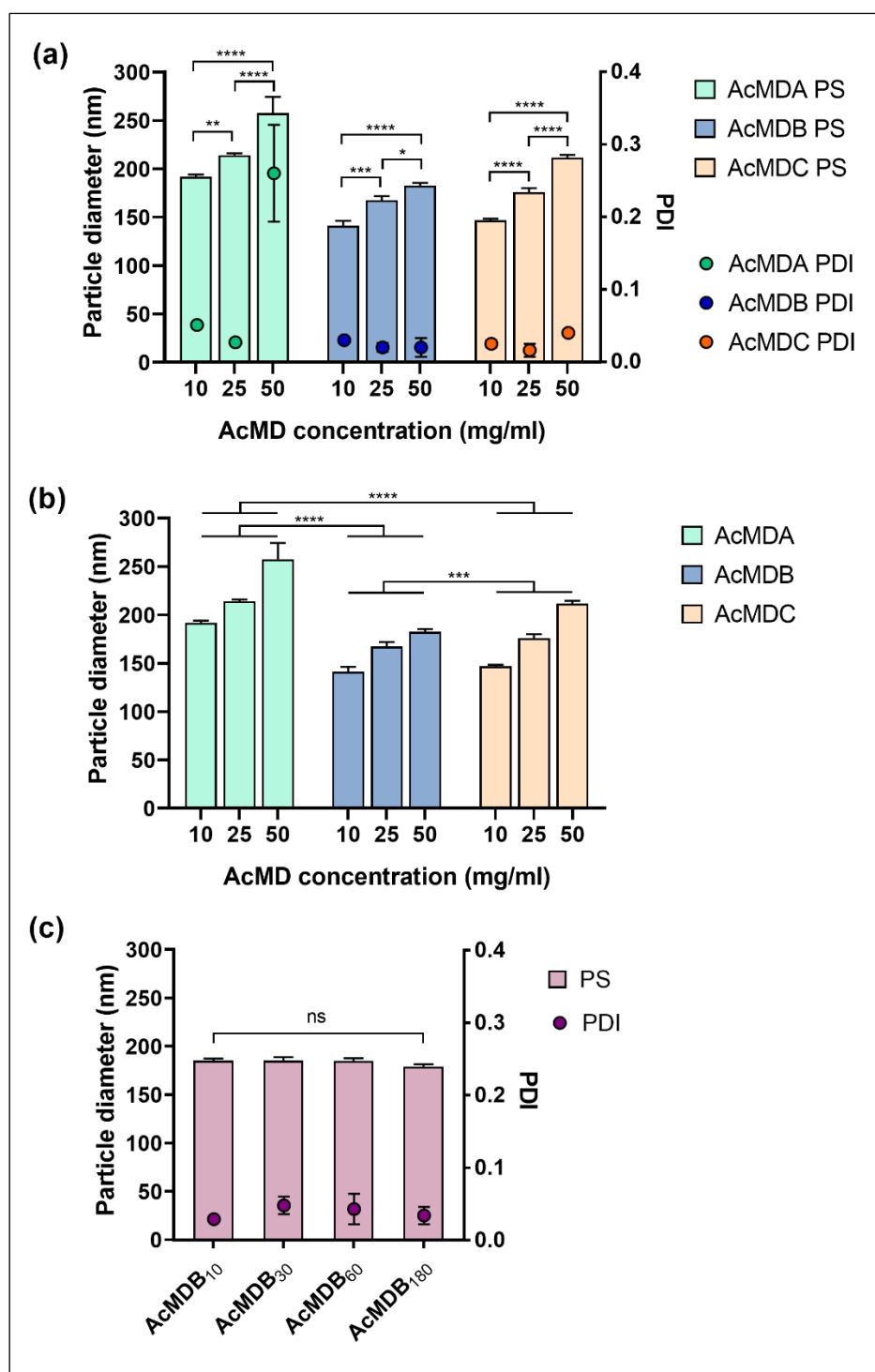
Figure 14. Particle size and PDI of plain AcMD-NPs showing the statistical significance of (a) AcMD mass concentration and (b) AcMD molecular weight. (c) Particle size and PDI resveratrol-loaded AcMD-NPs prepared from AcMDB with different cyclic/acyclic ratios. All data displayed are mean values ± standard deviation from n = 3 independent experiments. ****: $p < 0.0001$, ***: $p < 0.001$, **: $p < 0.01$, *: $p < 0.05$, and ns: $p > 0.05$.
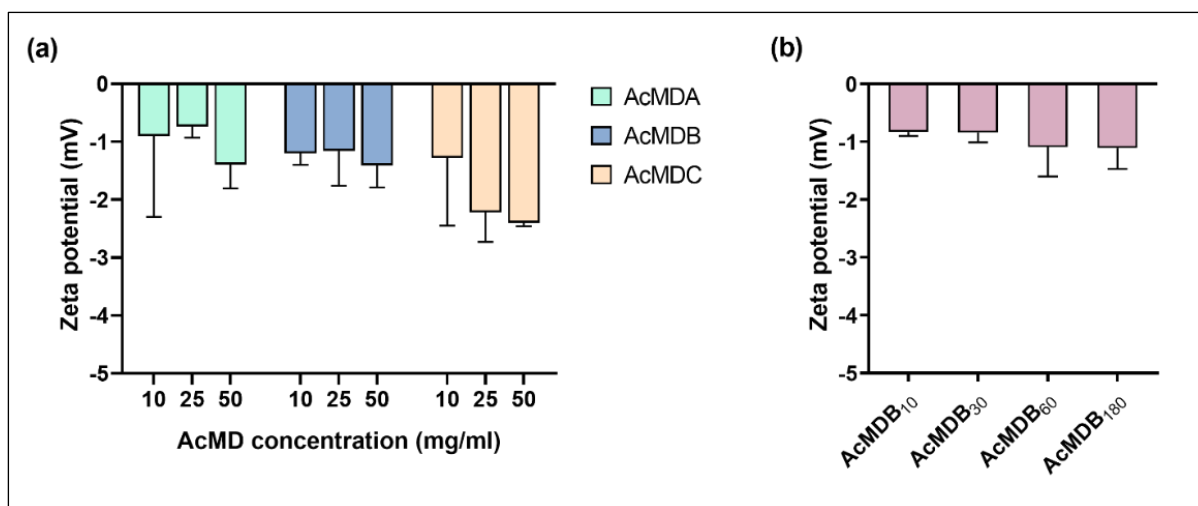
Figure 15. Zeta potential of (a) plain AcMD-NPs prepared at different polymer molecular weights and mass concentrations and (b) resveratrol-loaded AcMDB-NPs prepared from AcMD with different cyclic/acyclic ratios. All data represent mean values ± standard deviation from n = 3 independent experiments.

6.3.2.2 Nanoparticle morphology

SEM visualization revealed the spherical morphology of AcMD-NPs **(Figure 16)** with homogenous appearance and particle diameter comparable to that obtained by DLS measurement. The homogeneity of the particle ensemble and the small size distribution is also reflected in the SEM micrographs. The exclusive arrangement of the particles in two dimensions is also a clear support of the absence of agglomeration in the samples. The incorporation of the drug did not change the particles morphology and no free drug in crystalline form can be seen.
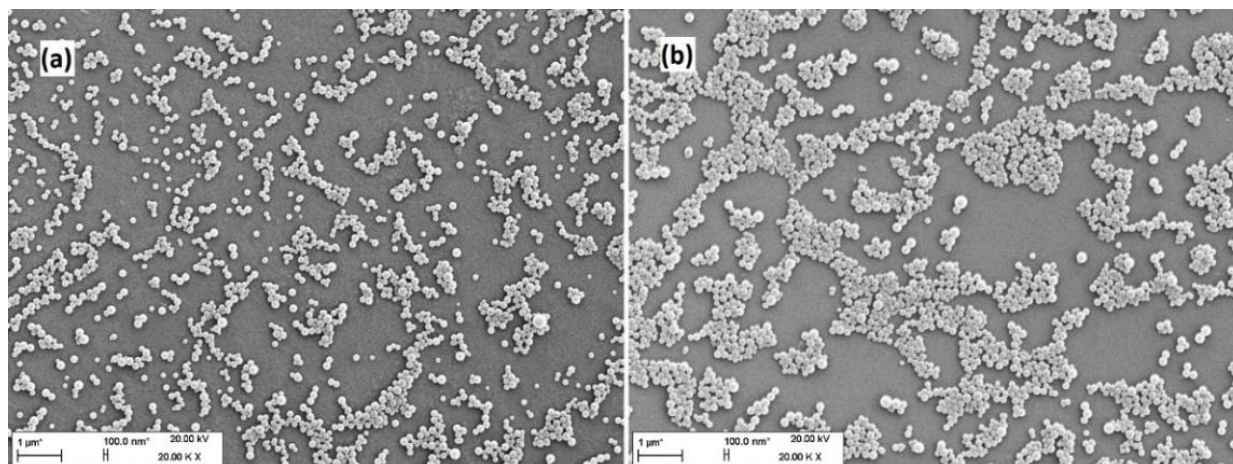
Figure 16. SEM images of (a) plain AcMDB-NPs prepared at 25 mg/ml polymer mass concentration and (b) the corresponding resveratrol-loaded AcMDB-NPs, examined at 20 kV using a magnification of 20,000x.

6.3.2.3 EE% and DL%

Nanoprecipitation could be considered as the method of choice for loading hydrophobic cargo within a hydrophobic matrix. It should be noted here that nearly 40% of the marketed drugs and 90% of drugs in development phase have poor water solubilities [167], signifying the usefulness of nanoprecipitation in this regard.

AcMDB-NPs with different cyclic/acyclic acetal ratios were successfully loaded with resveratrol with an overall mean EE% and DL% of 62.93 $\pm$ 5.8% and 3.51 $\pm$ 0.21%, respectively, where increasing the cyclic acetal proportion did not have any significant impact on the loading **(Figure 17)**. The supposed increase in the polymer hydrophobicity by increasing the cyclic acetal modifications and the expected effect on the encapsulation efficiency [122] was not seen. This was in accordance with measurements reported by Chen et al. [168] who proved that the polymer hydrophobicity, based on water contact angle measurements, does not strongly correlate to the cyclic/acyclic acetal ratio.
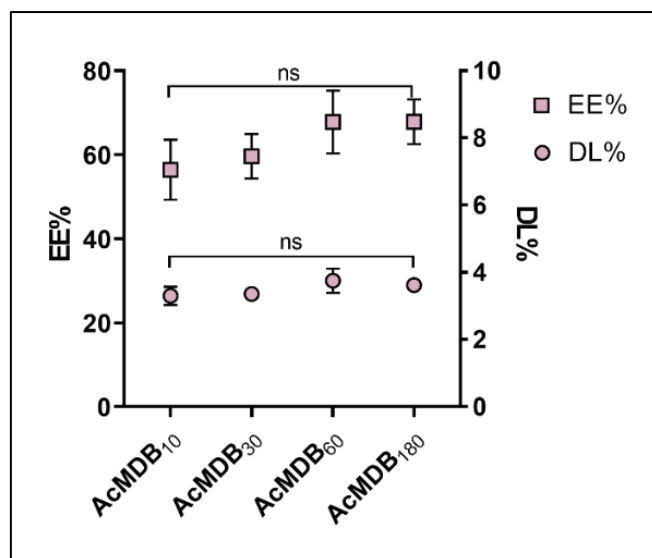
Figure 17. EE% and DL% of resveratrol-loaded AcMDB-NPs prepared from AcMD with different cyclic/acyclic ratios. All data displayed are mean values ± standard deviation from n = 3 independent experiments. ns: $p > 0.05$.

6.3.3 Nanoparticle pH-dependent degradation

Through the ongoing acid-driven nanoparticle degradation, increasing amounts of MD polysaccharide chains are produced at different rates, of which the reducing power was assayed using the BCA assay. Nanoparticle degradation was investigated with respect to molecular weight and cyclic/acyclic acetal ratio. **Figure 18a** depicts that the differences in molecular weight among AcMDA, AcMDB and AcMDC did not elicit a remarkable difference in their degradation rate. Slower degradation kinetics might have been expected for the higher molecular weight AcMDA, where longer polymer chains were thought to require more time for degradation and detachment from the nanoparticle matrices. However, another factor which may also play an important role in this regard and outweigh this anticipated delay is the polymer packing density. Shorter polymer chains, in case of AcMDB and AcMDC, could be more densely packed, impeding the diffusion of hydronium ions and water molecules through the nanoparticle matrix and decreasing the overall surface area exposed for hydrolysis [168].

On the other hand, increasing the cyclic acetal percentage from 20.82% (AcMDB10) to 46.97% (AcMDB180) slowed down the degradation kinetics at pH 5.0, where AcMDB10-,

AcMDB$_{30}$-, AcMD$_{60}$- and AcMD$_{180}$-NPs were fully degraded after 4, 6, 12 and 24 h, respectively **(Figure 18b)**. In both experiments, the particles could maintain a considerable integrity in pH 7.4 for 24 h and longer, confirming their acid mediated tunable degradation behavior.
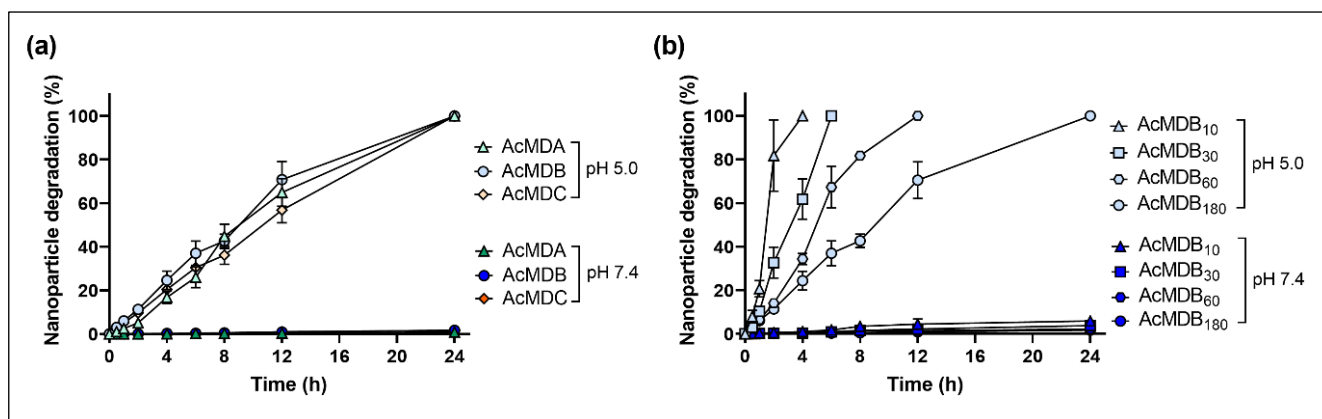
Figure 18. Nanoparticle degradation at pH 7.4 (PBS) and pH 5.0 (acetate buffer) at 37°C with respect to (a) polymer molecular weight and (b) cyclic/acyclic acetal modification ratio (20.82, 32.06, 38.42 and 46.97% for AcMDB$_{10}$, AcMDB$_{30}$, AcMDB$_{60}$ and AcMDB$_{180}$, respectively). The data are mean values $\pm$ standard deviation from n = 3 independent experiments.

6.3.4 *In vitro* release studies

In vitro release from resveratrol-loaded AcMD-NPs with different cyclic/acyclic acetal ratios was studied to evaluate their capability to control the release of resveratrol in a pH dependent manner. **Figure 19** shows that the maximum amount released in pH 7.4 at 24 h did not exceed 19.90 $\pm$ 2.18% to 36.27 $\pm$ 5.86% of the loaded resveratrol, in case of AcMDB$_{180}$ and AcMDB$_{10}$, respectively. It could be concluded that the release was limited to diffusion through the nanoparticle matrices. On the other hand, the release in pH 5.0 was both diffusion and erosion driven, where the rate of erosion decreased proportionally by increasing the cyclic acetal proportion, leading to slower resveratrol release in case of AcMDB$_{180}$ followed by AcMDB$_{60}$, AcMDB$_{30}$ and finally AcMDB$_{10}$.

It was also noticed that the overall release kinetics in acidic pH were relatively slower than the degradation kinetics. The nanoparticle degradation might have been affected by the

presence of resveratrol, that probably lead to changes in the nanoparticle physicochemical properties. Alternatively, the slower release kinetics may denote a central distribution of resveratrol within the nanoparticle matrices. Experimental set up differences might as well be a causative factor, where the presence of PEG-400 might have slowed down the diffusion of hydronium ions and water molecules to particle-medium interface.
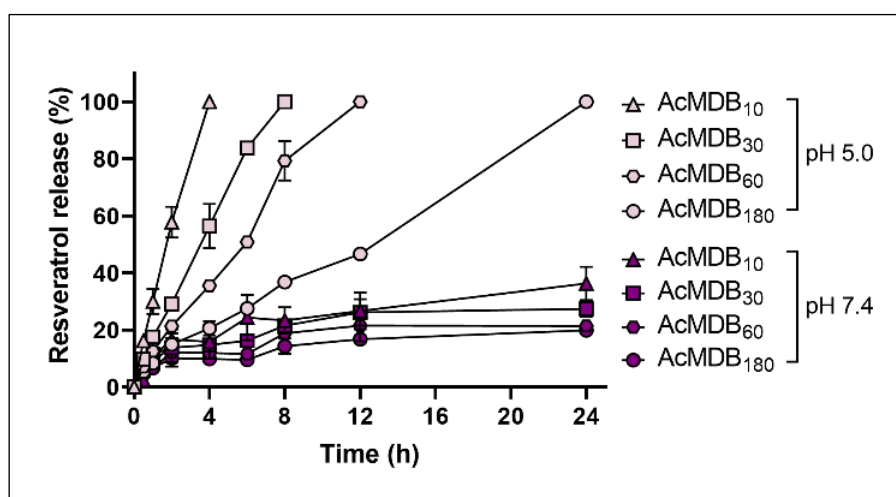
Figure 19. *In vitro* **release of resveratrol from loaded AcMDB-NPs with increasing cyclic acetal percentage (20.82, 32.06, 38.42 and 46.97% for AcMDB$_{10}$, AcMDB$_{30}$, AcMDB$_{60}$ and AcMDB$_{180}$, respectively) at pH 7.4 (PBS) and pH 5.0 (acetate buffer), and 37°C temperature. The data are mean values $\pm$ standard deviation from n = 3 independent experiments.**

6.3.5 *In vitro* biological experiments

6.3.5.1 Cell viability

Both fast degrading AcMDB$_{10}$-NPs and slow degrading AcMDB$_{180}$-NPs did not show any signs of acute cytotoxicity on A549 and dTHP-1 cells after 24 h incubation at concentrations as high as 1 mg/ml, as shown in **figure 20**. AcMD is in principle a modified biopolymer, consisting of biocompatible MD [111] and acetal groups that are hydrolyzed to acetone (a common by-product in metabolic pathways) and non-toxic amounts of methanol [137, 169].
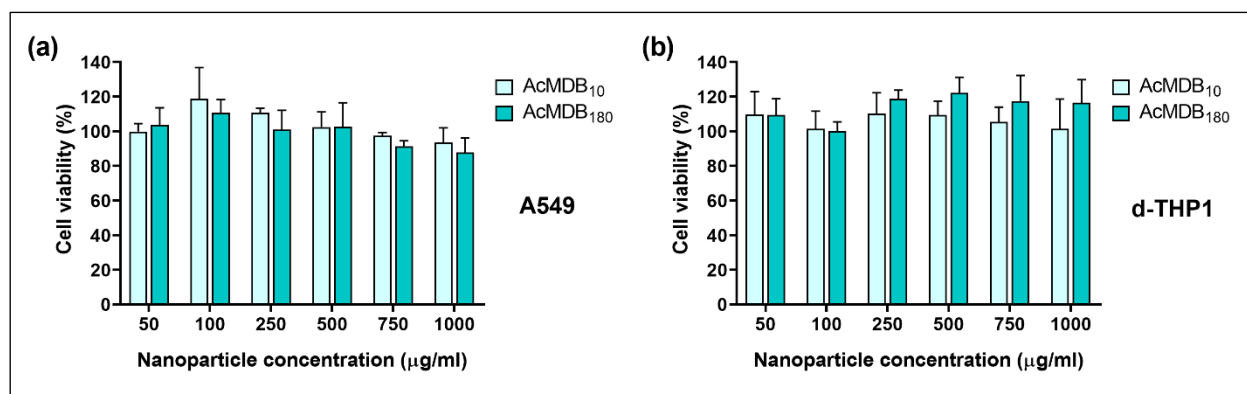
Figure 20. Cell viability of (a) A549 and (b) dTHP-1 cells after 24 h incubation with different concentrations (50 – 1000 μg/ml) of AcMDB$_{10}$-NPs and AcMDB$_{180}$-NPs determined using MTT assay. The data are mean values $\pm$ standard deviation from at least n = 3 independent experiments.

6.3.5.2 Cellular uptake

AcMDB NPs interacted differently with A549 and dTHP-1 cells. **Figure 21** shows that there was no noticeable interaction over the earlier intervals with the A549 cells, while the uptake could be clearly detected after 24 h. In contrast, dTHP-1 cells showed a noticeable uptake for both Rhod-AcMDB$_{10}$-NPs and Rhod-AcMDB$_{180}$-NPs even after 2 h, which is further increased after 24 h **(Figure 22)**. This could be explained by the different nature of either cell type, where dTHP-1 cells are inherently phagocytic cells and would easily engulf foreign particles [170]. It was also noted that the overall signal of Rhod-AcMDB$_{10}$-NPs was less prominent compared to Rhod-AcMDB$_{180}$-NPs, probably due to the faster degradation kinetics of the earlier prior to cellular uptake [137]. Alternatively, faster degradation after uptake would lead to a homogeneous distribution of the labeled polymer chains, reducing the intensity of specific spots in case of Rhod-AcMDB$_{10}$-NPs. Whereas for the slow degrading NPs, the particle architecture is conserved yielding a higher intensity signal at the nanoparticle location.
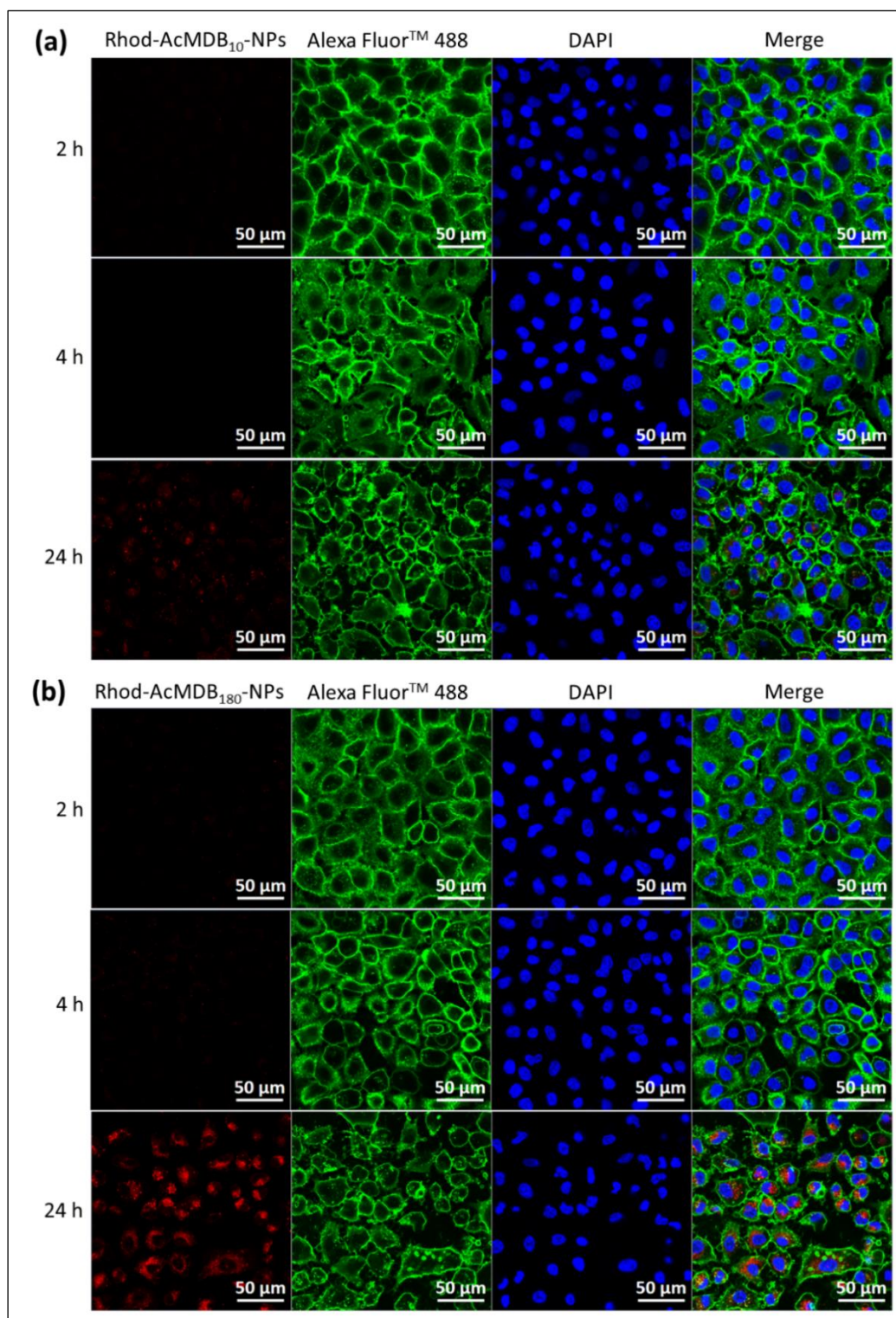
Figure 21. Cellular interaction of (a) Rhod-AcMDB$_{10}$-NPs and (b) Rhod-AcMDB$_{180}$-NPs with A549 cells at 2, 4, and 24 h incubation. Blue signal corresponds to nuclei stained with DAPI, green signal corresponds to cell membranes stained with Concanavalin A Alexa Fluor™ 488 conjugate, and red signal corresponds to rhodamine-labeled AcMDB-NPs.
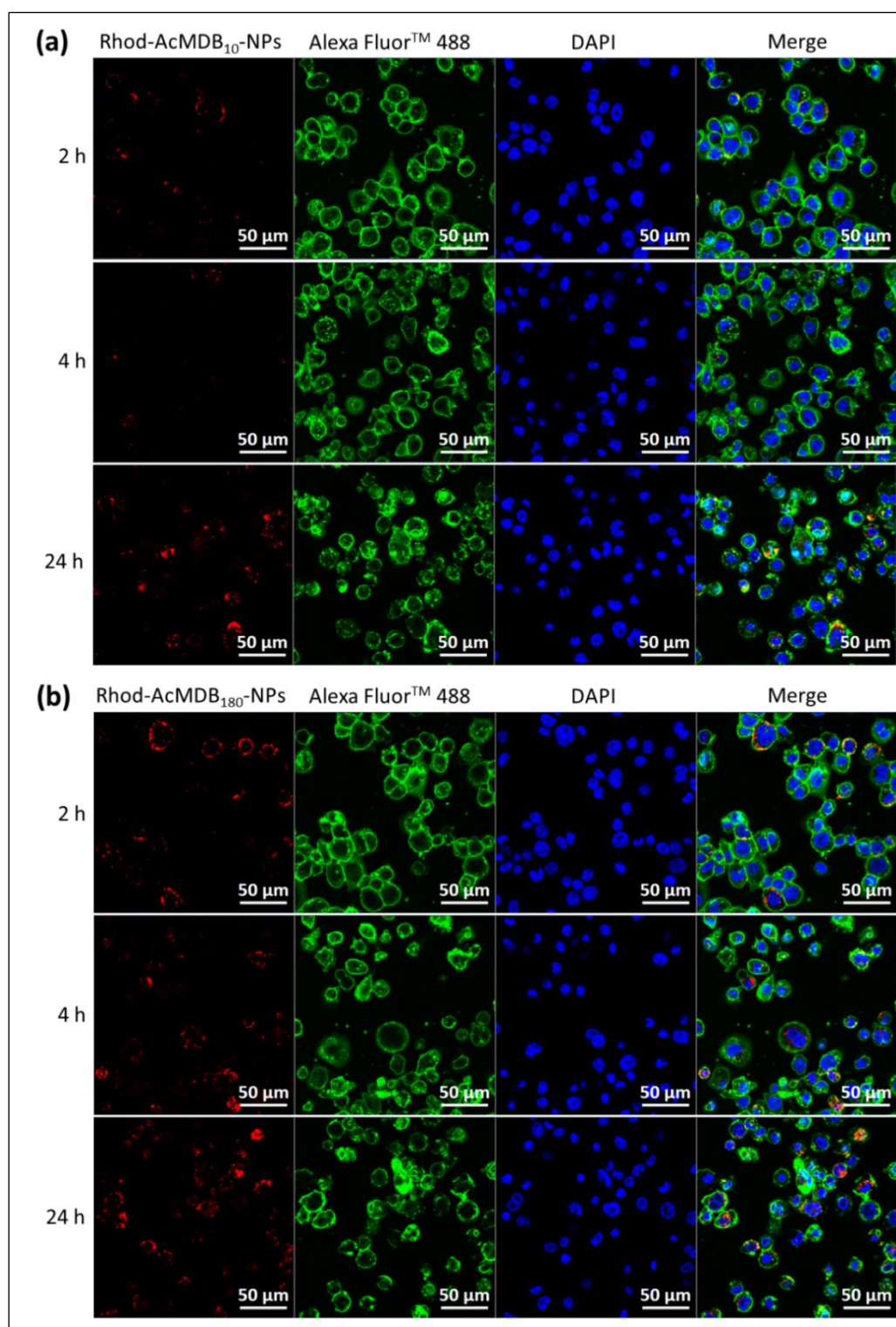
Figure 22. Cellular interaction of (a) Rhod-AcMDB$_{10}$-NPs and (b) Rhod-AcMDB$_{180}$-NPs with dTHP-1 cells at 2, 4, and 24 h incubation. Blue signal corresponds to nuclei stained with DAPI, green signal corresponds to cell membranes stained with Concanavalin A Alexa Fluor™ 488 conjugate, and red signal corresponds to rhodamine-labeled AcMDB-NPs.

6.4   Conclusion

Despite the broad molecular weight distribution of the hydrophobic derivative of MD presented in this work, AcMD could be used to produce monodisperse NPs with small diameters and tunable pH dependent degradability. This allows less intensive processing steps of the carbohydrates for application. Hence, this aspect is also relevant from an economic point of view and would keep additional production costs low. Loading AcMD-NPs with a model hydrophobic drug and their ability to control the release kinetics were demonstrated. The suggested nanoprecipitation procedure could be easily adapted for inclusion of desired hydrophobic cargo or also further extended to other technologies such as microfluidic nanoprecipitation. The tolerability of AcMD-NPs to the utilized somatic and immune cells indicates their safety and applicability. Whereas the different cell internalization behavior of AcMD-NPs proposes potential modifications based on the application of interest and whether extracellular or intracellular receptors are involved. For the scope of our project, we would explore the delivery of AcMD-NPs to the lungs through inhalation in the next chapter, proposing them as a potential pulmonary delivery system for the treatment of lung cancer.

Chapter III

Preparation and characterization of extracellular matrix (ECM)-modulating nano-structured microparticles

7. Chapter III: Preparation and characterization of extracellular matrix (ECM)-modulating nano-structured microparticles

7.1 Introduction

Upon inhalation, nanoparticles (NPs) would be rapidly exhaled due to their low gravitational sedimentation and inertial impaction, resulting in inefficient pulmonary deposition [48, 50, 171]. This raises the demand for a delivery method to optimally transport NPs to the pulmonary region of interest. One approach, that is simple from the formulation point of view, is to nebulize a nanoparticle suspension as an aerosol with the desired droplet size. However, nebulization has its shortcomings regarding the restricted portability, the lengthy time of administration and the formulation being in the liquid form, which may pose stability and contamination issues [79, 172]. Other inhalation devices that also implicate liquid dosage forms, such as pressurized metered-dose inhaler (pMDI) and soft mist inhaler (SMI), are not easily adaptable for lung cancer treatment, due to their limited capability to deliver drug doses in the microgram range [63]. The use of dry powder inhaler (DPI) provides several benefits over nebulizers, pMDIs and SMIs for pulmonary delivery in general, and for its application in lung cancer therapy in particular. Dry powder for inhalation, as a solid-state formulation, imparts better long-term physical stability to the formulation and the loaded drug. DPIs can deliver high drug doses, actuated by the patient's inhalation, in a short time and without the need for propellers or hand-breathing co-ordination [63, 85]. Moreover, they are handy, easy to maintain and disinfect, and can be produced as single-use inhalers to restrain the device and environmental contamination risks; which are common drawbacks of nebulizers [63].

To be formulated as dry powder for inhalation, NPs should be reversibly aggregated in the form of nano-structured or Trojan particles, that were firstly introduced by Tsapis et al. [98]. The aerodynamic diameter of the particles designed for inhalation, which is governed by the geometric diameter, particle density and shape, dictates the zone in which the particles would be deposited in the lungs. Particles exhibiting aerodynamic diameters between 0.5 and 5 μm would be majorly deposited in the lower respiratory airways, where an aerodynamic diameter below 3 μm is optimal for alveolar deposition [44, 50, 63]. The

nano-in-micro approach would not only enable the pulmonary delivery of NPs, but also circumvent clearance by alveolar macrophages, where particles in the size range from 0.5 to 5 μm suffer extensive phagocytosis [71, 173] (specifically in the range from 1.5 to 3 μm [66]). For this to be attained, the microparticles should readily redisperse into the constituting NPs upon hydration by the pulmonary fluids. Particle redispersibility, along with surface forces and powder properties (flowability, moisture content, hygroscopicity), necessitates the selection of the matrix-forming excipients, and the optimization of the spray drying conditions [85].

Delivery of NPs to the alveolar region, i.e., their availability at the vicinity of the tumor masses, does not necessarily ensure the efficacy of the treatment; the NPs should penetrate into the tumor to reach the target cancer cells. Solid tumors are characterized by the formation of a dense extracellular matrix (ECM), which impedes the diffusion of drug molecules or nanocarriers within the tumor interstitium and hence, results in treatment inadequacies [25, 38, 174, 175]. The ECM is composed of a highly organized network of fibrous proteins, proteoglycans, glycoproteins, glycosaminoglycans and other macromolecules [24]. Collagen is the most abundant protein and the main structural component of the ECM [22], where fibrillar collagen type I is the most prevalent and is generally linked to tumor cell survival and metastasis in many solid tumors [33]. Modulating the ECM through the intravenous or intratumoral administration of collagenase prior to treatment application has shown promising results for improving the treatment outcomes [174]. More recent studies explored the nano-based delivery of collagenase through physical adsorption, direct loading or surface chemical conjugation [38]. However, the release of collagenase with the desired kinetics and/or maintaining its enzymatic activity are potential difficulties to be tackled throughout the formulation design and evaluation steps.

Herein, our delivery system is composed of acetalated maltodextrin (AcMD)-NPs embedded in a collagenase-containing, water-soluble matrix, where collagenase would be released upon the matrix dissolution in the pulmonary fluid and enhance the penetration of the redispersed NPs into the tumor masses. The matrix composition as well as the spray drying conditions were optimized. The activity of collagenase after spray drying was

assessed. The microparticles (MPs) were characterized in terms of particle size, morphology, redispersibility, moisture content and *in vitro* pulmonary deposition.

7.2 Materials and methods

7.2.1 Materials

Maltodextrin (DE: 13.0-17.0), 2-methoxypropene, pyridinium *p*-toluene sulfonate (PPTS), triethylamine (TEA), 1,8-diazabicyclo[5.4.0]undec-7-ene (DBU), L-leucine, collagenase (obtained from *Clostridium histolyticum*, Type I), rhodamine B, fluorescein sodium salt and 1-octanol were purchased from Sigma-Aldrich (Steinheim, Germany). Poloxamer 407 was purchased from Caesar and Loretz GmbH (Hilden, Germany). Trehalose was purchased from Carl Roth (Karlsruhe, Germany). NHS-rhodamine was purchased from Thermo Fisher Scientific (Darmstadt, Germany). Dimethyl sulfoxide (DMSO, analytical grade), acetone and ethanol (HPLC grade) were purchased from Fisher Scientific (Schwerte, Germany). n-Hexane (HPLC grade) was purchased from VWR (Darmstadt, Germany). All the other reagents used were purchased with HPLC or analytical grade.

7.2.2 Preparation and characterization of AcMD-NPs

AcMD-NPs were prepared as described previously in **chapter II, section 6.2.3**. The preparation was carried out using AcMDB polymer and 25 mg/ml polymer solution mass concentration. Fluorescent AcMD-NPs were prepared by the same described procedure using Rhod-AcMDB$_{180}$ (synthesis demonstrated in **chapter I, section 5.2.3**). Based on the yield determined through freeze drying, the particles were suspended in a suitable volume of slightly alkaline Milli-Q water to have a particle concentration of 10 mg/ml. This nanoparticle stock suspension was used in spray drying step. The prepared NPs were characterized as described in **chapter II, section 6.2.4**.

7.2.3 Preparation of AcMD nano-structured MPs

Aqueous stock solutions of leucine (10 mg/ml) and trehalose (20 mg/ml) were prepared. Based on the required microparticle composition **(Table 3)**; stock suspension of AcMD-NPs, leucine and trehalose stock solutions were mixed in different proportions and

diluted with slightly alkaline Milli-Q water. When powder quantification was required, rhodamine B was added to the spray drying feed suspension at a concentration of 50 μg for each 100 mg of total solid mass. The final total solid concentration in the precursor suspensions to be sprayed was fixed at 1% (m/v). The nanoparticle aqueous suspension was spray dried using a Büchi Mini Spray Dryer (B-290, Büchi, Flawil, Switzerland) equipped with a standard two-fluid nozzle (0.7 mm hole diameter). Nitrogen was used as the spraying gas. The inlet temperature was adjusted at 50°C and the resulting outlet temperature was 38-42°C. The feed pump rate was set at 1.5 ml/min (5%), the spraying gas rotameter at 50 mm (601/1052 L/h), and the aspirator at 100% (35 m^3/h). Powder samples were collected and stored in a desiccator. Samples were prepared in triplicates.

For collagenase containing samples, required amounts of collagenase were weighed and added to the rest of formulation components directly before spray drying. The formulation suspension was magnetically stirred till dissolution of collagenase and spray drying was performed as described.

Table 3. Mass composition of the spray dried nano-structured MPs. The proportion of each component is expressed as the mass percentage of this component relative to the total powder mass (m%).

Sample	NP (m%)	leucine (m%)	Trehalose (m%)	Collagenase (m%)
$NP_{20}L_0$*	20	0	80	0
$NP_{10}L_{30}$	10	30	60	0
$NP_{20}L_{30}$	20	30	50	0
$NP_{30}L_{30}$	30	30	40	0
$NP_{20}L_{30}C_{10}$*	20	30	40	10
$NP_{20}L_{30}C_{30}$	20	30	20	30
$NP_{20}L_{30}C_{50}$	20	30	0	50

*NP_xL_x indicates the mixing ratio of the compounds used as stated in the table: NP: fraction of NPs, L: fraction of leucine, and C: fraction of collagenase

7.2.4 Assessment of collagenase activity after spray drying

The activity of collagenase was measured colorimetrically (Collagenase Activity Colorimetric Assay Kit, Sigma-Aldrich, St. Louis, United States), following the manufacturer's protocol and using microplate reader (Infinite M200, Tecan group, Männedorf, Switzerland) in the kinetic mode. The collagenase activity was first tested against different inlet temperatures (50, 60 and 70 °C). Second, it was tested at the selected inlet temperature for different collagenase mass content per dry powder (10, 30 and 50%). It is expressed as percentage of retained activity, relative to a freshly prepared collagenase solution of an equivalent concentration to the reconstituted powder sample of interest.

7.2.5 Particle size and size distribution determination

The particle size was measured using laser diffractometer (Master sizer 2000 Ver. 2.00, Malvern Instruments, Malvern, UK). The samples were dispersed in 1-octanol/n-hexane (20:80% v/v) at a concentration of 1 mg/ml. This proportion of 1-octanol was found to produce a good dispersion of the MPs, whereas they agglomerated strongly when n-hexane was used solely as a dispersant. The particle suspension was added slowly to the measurement chamber under stirring till the optimum obscuration was reached. The stirring function was used at 1500 rpm. The median volume diameter ($D_{v0.5}$) and the span value were used to describe the particle size and the polydispersity, respectively. The measurements were performed in triplicates and the mean values were used.

7.2.6 Particle morphology using scanning electron microscope (SEM) and confocal laser scanning microscope (CLSM)

The particles were visualized using SEM (Zeiss EVO HD15, Carl Zeiss, Oberkochen, Germany). The powder sample was applied to silica wavers attached to a metal stub. Excess powder was air blown. The MPs were sputter coated with 10 nm gold layer (Quorum Q150R ES, Quorum Technologies, East Sussex, United Kingdom) and examined at 10 kV under high vacuum.

For the visualization of nanoparticle regional distribution within the microparticle matrix, rhodamine-labeled AcMD-NPs were used, and the matrix was labeled with sodium

fluorescein. The MPs were dispersed in immersion oil (Immersol^{TM} 518 F, Carl Zeiss, Jena, Germany) and placed between two glass covers. The visualization was performed using CLSM (LSM 710, Carl Zeiss AG, Jena, Germany) using EC Plan-Neofluar 100x oil immersion objective. Fluorescein and rhodamine were excited at 488 and 561 nm using argon laser and the emission was recorded at 493 – 562 and 566 – 703 nm for each dye, respectively. Signals from both channels were merged and the images were processed using Zen 3.0 (blue edition) software (Carl Zeiss Microscopy, 2019).

7.2.7   Evaluation of redispersibility

7.2.7.1   Qualitative evaluation of redispersibility

The redispersibility was qualitatively evaluated using SEM (Zeiss EVO HD15, Carl Zeiss, Oberkochen, Germany). A thin film of powder was deposited on a silica waver fixed on a metal stub. A volume of 10 μl of water was added on top of the powder and left for 5 minutes. Afterwards, the excess water was carefully wicked using Kimtech® tissue and the sample was air dried. The MPs were sputter coated and examined as described in **section 7.2.6** in this chapter.

7.2.7.2   Quantitative evaluation of redispersibility

The redispersibility was evaluated as previously described in literature with minor modifications [172]. A sample amount of approximately 10 mg (m_1) was weighed into a pre-weighed Eppendorf tube. A volume of 2 ml of simulated lung fluid (SLF 3 [176]) was added and the tubes were incubated, horizontally aligned, in a shaking water bath at 37°C, 100 rpm for 30 min (Shaking incubator 3031, GFL, Burgwedel, Germany). Afterwards, the samples were centrifuged at 2000 g for 5 min (Sigma 3-30KS, Sigma, Osterode am Harz, Germany) to separate the redispersed NPs in the supernatant from the pelleted unredispersed particles or fragments. The supernatants were separated and the size and the polydispersity index (PDI) of the redispersed NPs were measured (Zetasizer Ultra, Malvern Panalytical, Worcestershire, United Kingdom). The pellets were washed by carefully adding water and the centrifugation/washing step was repeated twice. The pellets were frozen at -80 °C, lyophilized (Alpha 2-4 LSC, Christ, Osterode am Harz, Germany) and the masses

were determined after lyophilization (m_2). The redispersed powder fraction was determined using **equation 6**.

$$Redispersed\ powder\ fraction\ (\%) = \frac{m_1 - m_2}{m_1} \times 100 \qquad Equation\ 6$$

Assuming the complete dissolution of the water-soluble matrix components, the pellet would be considered to represent the non-redispersed NPs. Therefore, the mass fraction of redispersed NPs was calculated by relating the redispersed nanoparticle mass to the total theoretical mass of NPs in the formulation (m_{NP}), as follows:

$$Redispersed\ NP\ fraction\ (\%) = \frac{m_{NP} - m_2}{m_{NP}} \times 100 \qquad Equation\ 7$$

7.2.8 Determination of moisture content

The moisture content was determined by thermogravimetric analysis, using a thermogravimetric analyzer (TG 209 F1 Libra, Netzsch, Selb, Germany) under a nitrogen atmosphere. The analysis was carried out from 30 to 300 °C at a heating rate of 5 °C/min. The sample mass was about 5 mg and the percentage mass loss from 30 to 150 °C was used to calculate the residual moisture content. The thermograms were generated and processed using Netzsch Proteus® Software.

7.2.9 Evaluation of aerodynamic properties
7.2.9.1 Next generation impactor (NGI) experiment

The aerodynamic properties were determined using NGI (Copley Scientific, Nottingham, UK) [172, 177, 178]. A mass of approximately 10 mg of rhodamine B-labelled powder samples were weighed into hard gelatin capsules (size 3) and the capsules were securely closed. The filled capsule was placed in a HandiHaler® (Boehringer Ingelheim, Ingelheim, Germany) and punctured prior to aerosolization. The impactor cups were coated with a mixture of 15% Brij 35 ethanolic solution and glycerol (40:60) and the pre-separator was filled with 5 ml Milli-Q water. The gas flow was preadjusted by a flowmeter (M1A, Copley Scientific, Nottingham, UK). After the full assembly of the impactor, the inhaler was fitted at the induction port and the powder was aerosolized at 60 L/min gas flow for 4 seconds using a vacuum pump and critical flow controller (Erweka, Heusenstamm,

Germany). The deposited powder at the induction port and the cups were collected by thorough rinsing with a definite volume of Milli-Q water. The experiment was performed in independent triplicates for all the tested formulations.

7.2.9.2 Powder quantification

The concentration of the deposited powder was determined through measuring the fluorescence of rhodamine B (λ_{ex}: 565 nm and λ_{em}: 625) using microplate reader (Infinite M200, Tecan group, Männedorf, Switzerland). For each powder sample, the mass of the powder collected from the induction port, the preseparator, the stages, as well as the capsule shell, was determined against its own calibration plot in water (20 - 1000 μg/ml concentration range) and the respective cumulative powder masses were calculated.

7.2.9.3 Aerodynamic properties calculation

The effective cut-off diameters of the NGI stages at 60 L/min flow rate were used as specified in the European Pharmacopeia and the USP (cut-off diameter from the micro-orifice collector (MOC) to stage 1: 0.34, 0.55, 0.94, 1.66, 2.82, 4.46 and 8.06 μm in order). The cumulative powder mass percentage deposited at each stage (relative to the cumulative mass at stage 1) was calculated and transformed into probit values. The probit values were plotted against the log cut-off diameters of each stage, where a calibration range including probit of 5 and log cut-off diameter of 0.7 was used for setting the linear regression equation. The emitted dose (ED), which describes the percentage of the powder emitted from the capsule, was calculated using **equation 8** [179]. The mass median aerodynamic diameter (MMAD) was calculated from the linear regression equation, as the diameter corresponding to the cumulative mass fraction of 50% (probit value of 5). The geometric standard deviation (GSD) was calculated based on the 84% (d_{84}) and 16% (d_{16}) cut-off diameters (probit values of 5.99 and 4.01, respectively) using **equation 9**. The fine particle fraction (FPF) was calculated using the cumulative mass fraction corresponding to cut off diameter of 5 μm (probit value of 0.7), relative to the ED [172, 180].

$$ED = \frac{Initial\ powder\ mass\ -\ Remaining\ mass\ in\ empty\ capsules}{Initial\ powder\ mass} \times 100 \qquad \textbf{Equation 8}$$

$$GSD = \left(\frac{d_{84}}{d_{16}} \right)^{1/2} \qquad \text{Equation 9}$$

7.2.10 Statistical analysis

The results are expressed as mean $\pm$ standard deviation of three independent replicates. Statistical significance was tested using one-way analysis of variance (ANOVA), followed by Tukey or Dunnett *post hoc* tests for multiple comparisons between all pairs or with respect to standard sample, respectively. The level of significance was set at a *p*-value of 0.05. Statistical analysis was implemented using GraphPad Prism (version 8.0.2) software (GraphPad Software, 2019).

7.3 Results and discussion

7.3.1 Preparation of AcMD nano-structured MPs

Different matrix forming agents were first preliminarily tested for the particle formation; mannitol, trehalose and leucine, with an initial nanoparticle mass content of 10%, feed concentration of 1%, feed flow rate of 10%, and inlet temperature of 70 °C. The spray dried MPs were characterized in terms of morphology, redispersibility, and aerodynamic properties. Leucine nano-structured MPs were found to be superior in terms of redispersibility and aerodynamic properties followed by trehalose and mannitol. However, the SEM pictures of the leucine nano-structured MPs showed relatively large, cracked particles with obvious broken fragments. Accordingly, a mixture of trehalose and leucine was selected for the matrix formation to support the mechanical strength of the particles. The spray drying conditions were also investigated by changing the feed concentration at 0.5 and 1% and the feed flow rate at 5 and 10%. It was found that using 1% feed concentration at lower flow rate yielded smaller MPs with better deposition characteristics. Leucine mass content was also tested; 30% mass content was found sufficient for improving the redispersibility and the aerodynamic properties. The selection of the inlet temperature and the nanoparticle mass content would be described in the following sections.

7.3.2 Collagenase activity after spray drying

In order to select the optimum inlet temperature for spray drying, the activity of collagenase was assayed after spray drying at 50, 60 and 70 °C inlet temperatures. **Figure 23a** shows that the effect of temperature in this range was minimal, with no significant difference among the inlet temperatures tested. The retained activity was as high as 89.5 ± 6.7% when spray drying was performed at an inlet temperature of 50 °C. This result was further confirmed by spray drying formulations with increasing collagenase mass content (10, 30 and 50%), where they all exhibited comparable preservation of collagenase activity after spray drying at 50 °C **(Figure 23b)**.

Exposure to high temperatures during spray drying was supposed to pose a challenge against spray drying of collagenase, due to heat-mediated denaturation and enzyme inactivation [181]. However, the results support that spray drying is very mild to cause a dramatic decrease in enzyme activity. This may be ascribed to the brief exposure to high temperatures, immediately followed by evaporative cooling and loss of moisture [182]. One other contributing factor is the presence of leucine and trehalose, with their protective effects due to water replacement through hydrogen bond formation [183, 184]. The retainment of activity among the formulations containing increasing amounts of collagenase, and accordingly decreasing amounts of trehalose, suggests that leucine alone was sufficient for enzyme activity preservation. In addition to hydrogen bond formation, orientation of hydrophobic groups of leucine towards the liquid-air interface would further protect the enzyme against denaturation [182].
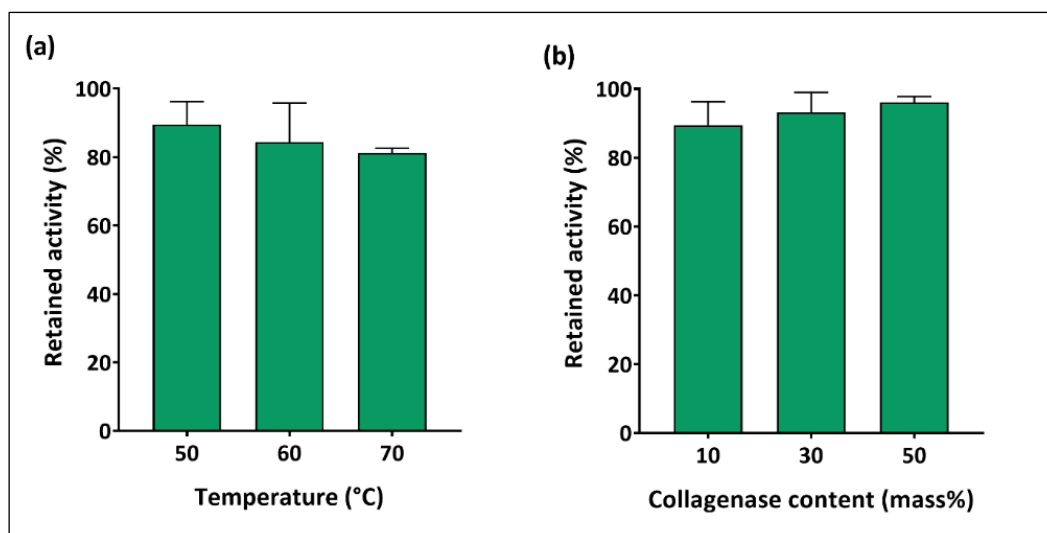
Figure 23. Percentage of retained activity of collagenase after spray drying at (a) different inlet temperatures (50, 60 and 70 °C) and (b) increasing collagenase mass content (10, 30 and 50%). The activity was assayed by collagenase activity colorimetric kit and the data represent mean values ± standard deviation of independent triplicates.

7.3.3 Particle size and size distribution

It is generally known that the smaller the particle size of the powder, the higher its potential for alveolar deposition. However, the particle diameter measured by laser diffraction does not consider the particle density nor the morphology. Therefore, the MMAD is a better indication of the deposition [185], and the results of its evaluation are discussed in **section 7.3.7** in this chapter. The particles size was found to be affected by the formulation composition **(Table 4)**. Addition of leucine in formulations $NP_{10}L_{30}$, $NP_{20}L_{30}$ and $NP_{30}L_{30}$ was found to increase the particle size relative to the leucine-free formulation $NP_{20}L_0$. This would be attributed to the surface properties of leucine, where it accumulates at the droplet surface during the drying step forming a crust that would resist shrinkage [186]. However, changing the nanoparticle mass content from 10 to 30% does not appear to considerably impact the particle size distribution. Comparing collagenase-containing nano-structured MPs ($NP_{20}L_{30}C_{10}$, $NP_{20}L_{30}C_{30}$ and $NP_{20}L_{30}C_{50}$) to their collagenase-free counterpart ($NP_{20}L_{30}$), inclusion of collagenase was found to shift the particle size distribution towards smaller diameters.

Table 4. Particle size distribution of spray dried nano-structured MPs. The results show 10, 50, and 90 percentile volume diameters ($D_{v0.1}$, $D_{v0.5}$ and $D_{v0.9}$, respectively) and the Span index. The displayed results represent the mean $\pm$ standard deviation of three independent volume-based light scattering measurements.

Sample	$D_{v0.1}$ (μm)	$D_{v0.5}$ (μm)	$D_{v0.9}$ (μm)	Span
$NP_{20}L_0$	0.56 $\pm$ 0.13	1.67 $\pm$ 0.19	5.70 $\pm$ 0.75	3.08 $\pm$ 0.17
$NP_{10}L_{30}$	0.68 $\pm$ 0.05	6.55 $\pm$ 0.54	13.03 $\pm$ 0.25	1.89 $\pm$ 0.12
$NP_{20}L_{30}$	0.61 $\pm$ 0.01	6.82 $\pm$ 0.61	11.89 $\pm$ 1.12	1.65 $\pm$ 0.02
$NP_{30}L_{30}$	0.51 $\pm$ 0.11	4.43 $\pm$ 0.72	9.40 $\pm$ 0.07	2.04 $\pm$ 0.32
$NP_{20}L_{30}C_{10}$	0.41 $\pm$ 0.04	2.99 $\pm$ 0.54	8.48 $\pm$ 1.9	2.67 $\pm$ 0.31
$NP_{20}L_{30}C_{30}$	0.35 $\pm$ 0.04	2.58 $\pm$ 1.35	7.14 $\pm$ 1.47	2.89 $\pm$ 0.73
$NP_{20}L_{30}C_{50}$	0.33 $\pm$ 0.02	3.01 $\pm$ 0.68	8.03 $\pm$ 0.91	2.81 $\pm$ 0.81

7.3.4 Particle morphology using SEM and CLSM

The AcMD nano-structured MPs were visualized by SEM **(Figure 24)**. Leucine, as a formulation component, was found to have a remarkable influence on the particle size and morphology. Compared to the leucine-free $NP_{20}L_0$ **(Figure 24a)**, $NP_{20}L_{30}$ SEM images **(Figure 24b)** show unaggregated, hollow particles with some surface corrugations and a more obvious presence of larger-sized population. This last observation conforms with the different particle size distribution detected by laser diffraction for both samples **(Table 4)**. It is worth mentioning that surface corrugations improve the aerosol performance of the particles, where this reduces the inter-particle contact points and hence their cohesiveness and adhesiveness [185]. The presence of surface corrugations would also raise the shape factor (*X*), and hence decrease the aerodynamic diameter of the particles in comparison to the geometric diameter [102]. The presence of collagenase in $NP_{20}L_{30}C_{10}$, $NP_{20}L_{30}C_{30}$ and $NP_{20}L_{30}C_{50}$ **(Figure 24c, d, and e, respectively)** does not seem to affect the particle surface morphology. Close observation of the MPs' surface reveals protruding NPs, which discloses the spatial accumulation of NPs at the surface and indicates surface roughness of the nano-

structured MPs. Surface roughness is assumed to positively contribute to the reduction of the inter-particulate surface forces, by increasing the distance between the adjacent particles and decreasing the area of contact [187]. The presence of leucine (with its interfacial accumulation) and NPs (with their low diffusion constant) would raise the Peclet number of the spray dried particles, leading to the formation of those characteristic buckled, hollow particles [188], as shown in **figure 24b - e**.
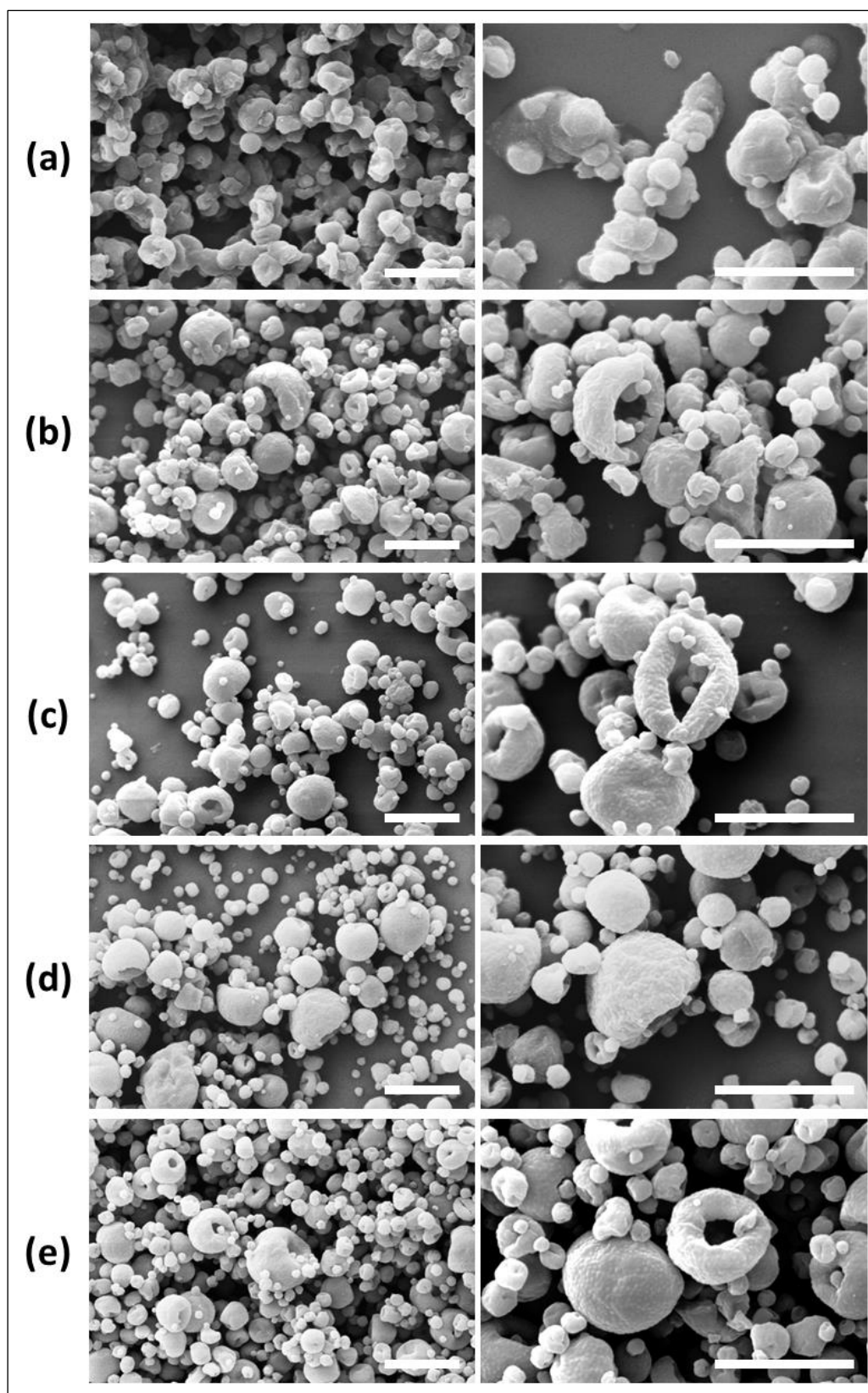
Figure 24. SEM pictures of (a) NP$_{20}$L$_0$, (b) NP$_{20}$L$_{30}$, (c) NP$_{20}$L$_{30}$C$_{10}$, (d) NP$_{20}$L$_{30}$C$_{30}$, and (e) NP$_{20}$L$_{30}$C$_{50}$ powder samples. Right panel images were captured at higher magnification. Scale bars are equivalent to 5 μm.

Figure 25 displays the CLSM pictures of the collagenase-free NP$_{20}$L$_{30}$ and the collagenase-containing NP$_{20}$L$_{30}$C$_{30}$ formulations. It can be observed that the rhodamine signal (corresponding to the AcMD-NPs) is well-defined at the periphery of the particles, in contrast to the fluorescein signal (corresponding to the matrix) that appears to be more diffuse. This verifies the surface distribution of the AcMD-NPs that was seen in the SEM images. The shapes exhibited by the matrix-localized fluorescein signal additionally confirm the hollowness of the MPs.
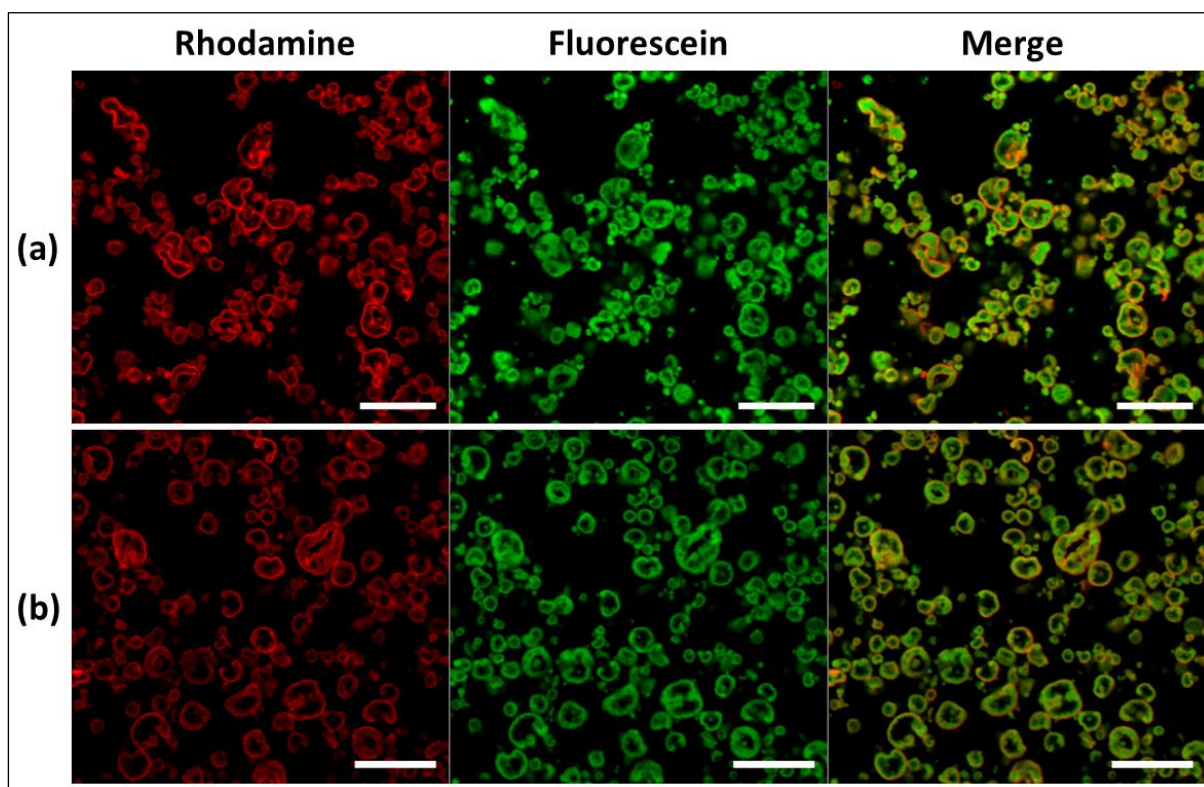
Figure 25. CLSM pictures of (a) NP$_{20}$L$_{30}$ and (b) NP$_{20}$L$_{30}$C$_{30}$ nano-structured MPs showing the distribution of the NPs within the MPs' matrix. Rhodamine and fluorescein signals correspond to Rhod-AcMD-NPs and microparticle matrix, respectively. Scale bars represent 10 μm.

7.3.5 Redispersibility evaluation

Sufficient redispersibility of MPs into NPs in SLF is a prerequisite, so that the effects of the latter could be realized. **Figure 26** shows the morphology of redispersed particles after hydration of MPs for 5 minutes. It could be observed from the SEM pictures that the fully

redispersed NPs are well separated with no major aggregation and comparable morphology to the NPs before spray drying **(Chapter II, section 6.3.2.2, figure 16)**.
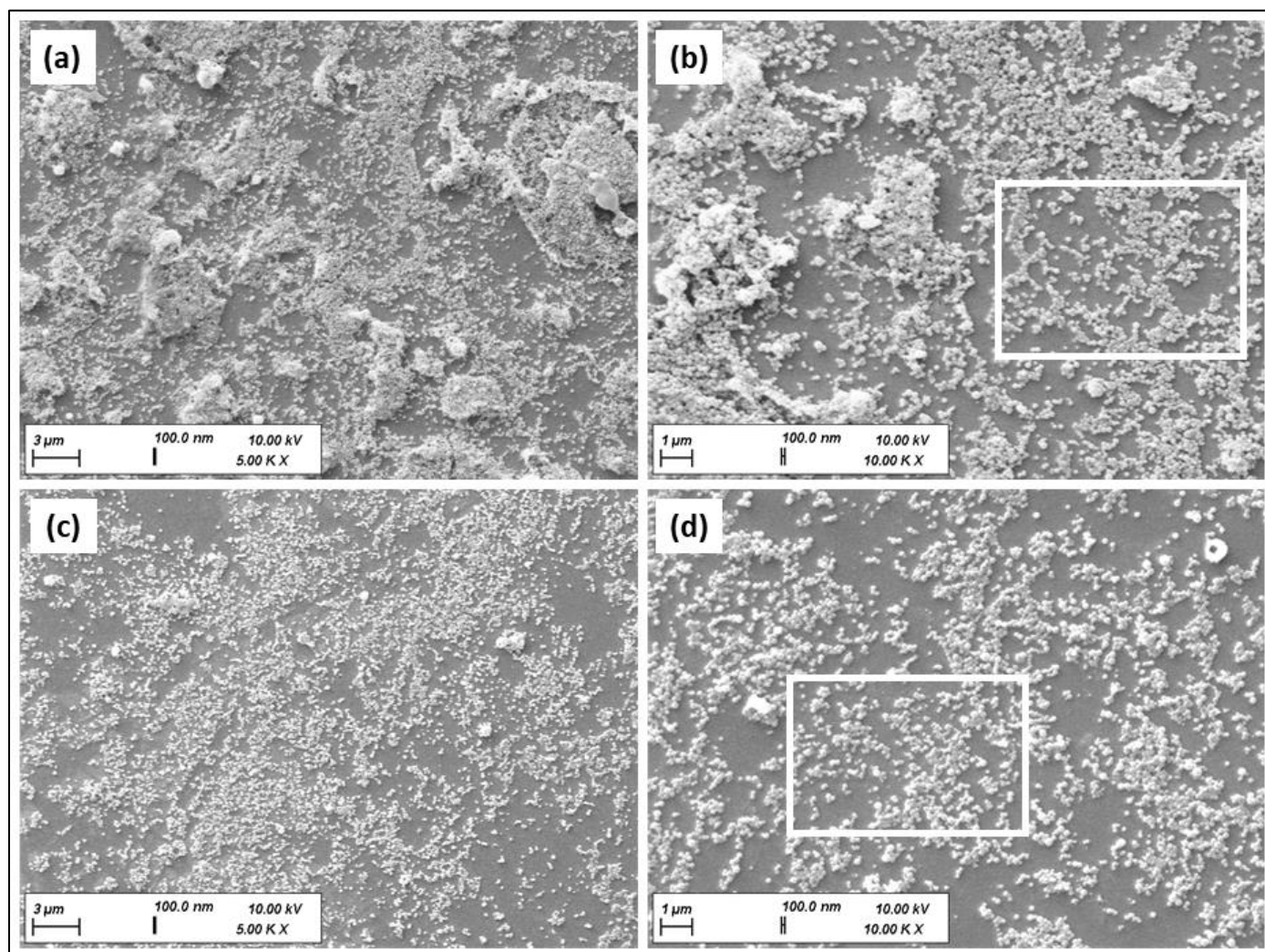
Figure 26. NP$_{20}$L$_{30}$ (a and b) and NP$_{20}$L$_{30}$C$_{30}$ (c and d) redispersed MPs after hydration with water for 5 min. The magnification power in images (a and c) is 5,000x and that of images (b and d) is 10,000x. Well defined redispersed NPs (as within the indicated frames) could be clearly seen for both powder samples, in addition to some aggregates of not fully redispersed particles.

The influence of nanoparticle mass content was first investigated by increasing it at 10, 20, and 30% in formulations NP$_{10}$L$_{30}$, NP$_{20}$L$_{30}$, and NP$_{30}$L$_{30}$, respectively. While increasing the nanoparticle content from 10 to 20% did not affect the redispersed powder fraction significantly, increasing it further to 30% lead to a significant decrease in redispersed powder fraction **(Figure 27a)**. The positive effect of leucine on the redispersibility could be

clearly observed by comparing $NP_{20}L_{30}$ to its leucine-blank analogue, $NP_{20}L_0$ (**Figure 27a**). Both the redispersed powder and nanoparticle fractions were significantly improved by the addition of leucine, where they reached 91.6 ± 0.4% and 58.1 ± 1.8%, respectively, for the leucine- containing formulation, $NP_{20}L_{30}$. Introducing collagenase to the best redispersing formulation, $NP_{20}L_{30}$ maintained its redispersibility attributes, with no significant differences among the individual formulations $NP_{20}L_{30}C_{10}$, $NP_{20}L_{30}C_{30}$ and $NP_{20}L_{30}C_{50}$ (with increasing collagenase mass content at 10, 30 and 50%). **Figure 27b** shows that except for $NP_{20}L_0$, the redispersed NPs from all the investigated samples exhibited comparable particle size distribution to that before spray drying, with slightly increased diameters and acceptable polydispersity.
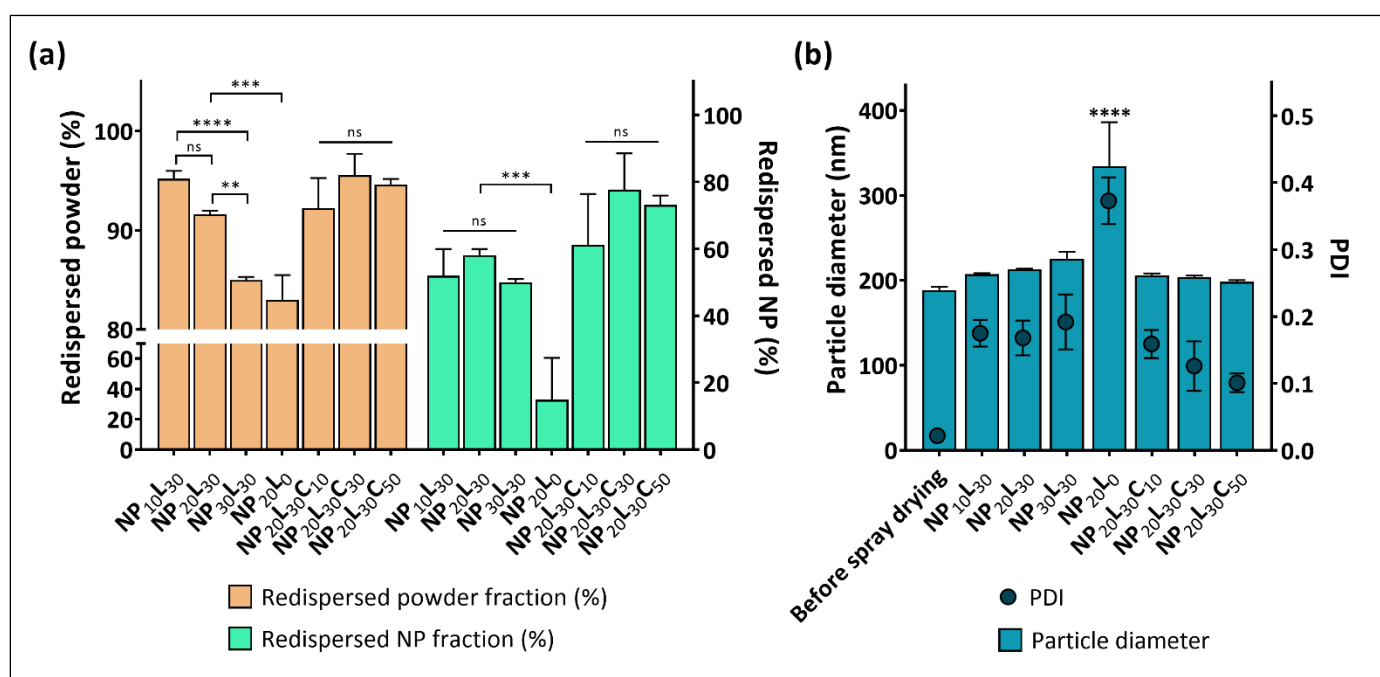
Figure 27. (a) Redispersed powder and nanoparticle percentages after dispersion of the tested MPs in SLF. MPs containing increasing content of NPs ($NP_{10}L_{30}$, $NP_{20}L_{30}$, and $NP_{30}L_{30}$), increasing amount of collagenase ($NP_{20}L_{30}C_{10}$, $NP_{20}L_{30}C_{30}$, and $NP_{20}L_{30}C_{50}$) as well as leucine-free MPs ($NP_{20}L_0$) were tested. (b) Particle diameter and PDI of NPs released after microparticle dispersion in SLF compared to particle size and PDI of AcMD-NPs before spray drying. The results represent mean ± standard deviation of independent triplicates. ****: $p < 0.0001$, ***: $p < 0.001$, **: $p < 0.01$, and ns: $p > 0.05$.

7.3.6 Moisture content

The moisture content of the spray dried collagenase-free ($NP_{20}L_{30}$) and collagenase-containing ($NP_{20}L_{30}C_{10}$, $NP_{20}L_{30}C_{30}$ and $NP_{20}L_{30}C_{50}$) formulations ranged from 2.03 $\pm$ 0.50 to 3.10 $\pm$ 0.20% **(Table 5)**. A residual moisture content of less than 5% is sufficiently low to protect the particles against the polymorphic changes, crystal formation and growth, and changes in particle size distribution upon storage [185, 186, 189]. Additionally, the residual moisture content should be as low as possible not only to avoid the pre-mentioned changes, but also to preserve collagenase from inactivation. Although the spray drier was operated at a relatively low inlet temperature of 50 °C, the obtained low moisture content shows the positive impact of the utilized low feed rate and maximal aspiration on the efficiency of moisture elimination. Moreover, the formation of a hydrophobic outer shell layer due to the presence of leucine is assumed to have an anti-hygroscopic effect and enhance the physical and chemical stability of the particles [186, 190, 191].

Table 5. Moisture content in spray dried collagenase-free ($NP_{20}L_{30}$) and collagenase-containing ($NP_{20}L_{30}C_{10}$, $NP_{20}L_{30}C_{30}$ and $NP_{20}L_{30}C_{50}$) powder samples. The moisture content was determined using TGA analysis and the results are expressed as triplicate mean $\pm$ standard deviation.

Sample	Moisture content (%)
$NP_{20}L_{30}$	2.03 $\pm$ 0.50
$NP_{20}L_{30}C_{10}$	2.71 $\pm$ 0.17
$NP_{20}L_{30}C_{30}$	3.01 $\pm$ 0.20
$NP_{20}L_{30}C_{50}$	3.10 $\pm$ 0.20

7.3.7 Aerodynamic properties

For alveolar pulmonary deposition, the powder should have a MMAD below 3 μm [79]. **Table 6** depicts that the MMAD of all the investigated powder formulations was within the required limit, with an acceptable distribution around the MMAD. A GSD of around 2 is acceptable for specific deposition in a certain region of the lungs [192], which supports the

feasibility of the prepared formulations. The FPF, which describes the amount of the powder that reaches the deep lungs, approached 70% for the collagenase-containing formulations ($NP_{20}L_{30}C_{10}$, $NP_{20}L_{30}C_{30}$ and $NP_{20}L_{30}C_{50}$). It could be noted that the FPF of the collagenase-free formulation ($NP_{20}L_{30}$) is lower than the collagenase-containing counterparts. This can be related to the larger particle size of the powder as was shown by the laser diffraction measurements, which is reflected as well by the relatively larger GSD of $NP_{20}L_{30}$. The high ED measured for all the formulations indicates sufficiently minimal adhesive forces between the powder and the capsule.

Table 6. Aerodynamic properties (ED, MMAD, GSD and FPF) of spray dried nano-structured MPs determined by NGI. The results represent mean $\pm$ standard deviation of independent triplicates.

Sample	ED (%)	MMAD (μm)	GSD (μm)	FPF (%)
$NP_{20}L_{30}$	96.33 $\pm$ 1.01	2.22 $\pm$ 0.28	2.36 $\pm$ 0.33	60.59 $\pm$ 4.72
$NP_{20}L_{30}C_{10}$	94.35 $\pm$ 0.32	1.93 $\pm$ 0.06	2.19 $\pm$ 0.03	69.62 $\pm$ 2.01
$NP_{20}L_{30}C_{30}$	94.90 $\pm$ 1.11	2.80 $\pm$ 0.10	1.78 $\pm$ 0.02	68.79 $\pm$ 4.80
$NP_{20}L_{30}C_{50}$	92.20 $\pm$ 3.76	2.72 $\pm$ 0.39	1.79 $\pm$ 0.02	68.02 $\pm$ 6.86

7.4 Conclusion

Spray drying of AcMD-NPs into inhalable nano-structured MPs using a combination of water-soluble matrix forming agents; trehalose and leucine, was successfully realized. The formulation composition and process parameters were optimized to yield particles exhibiting three main essential features: the desired aerodynamic properties to reach the alveolar region, sufficient redispersibility into NPs upon hydration, and nonimpaired collagenase activity after spray drying. The pulmonary delivery system presented herein, which comprises collagenase together with acid-degradable AcMD-NPs, represent a very promising carrier for anticancer drugs for lung adenocarcinoma treatment. The effect of collagenase on the penetration of AcMD-NPs through cellular spheroids would be assessed in the following chapter.

Chapter IV

In vitro tumor spheroid model for evaluation of particle penetration

8. Chapter IV: *In vitro* tumor spheroid model for evaluation of particle penetration

8.1 Introduction

Conventional two-dimensional (2D) monolayer cultures are the primary platform employed for *in vitro* cellular testing of novel drug molecules and delivery systems in cancer research. However, 2D monolayer cultures do not reflect the complex environment of solid tumors, leading to poor and incomparable therapeutic response in *in vivo* animal experiments or clinical trials [193, 194]. To date, three dimensional (3D) multicellular spheroids have been regarded as tumor-imitating *in vitro* models, that could serve as an intermediate stage between 2D cell cultures and *in vivo* testing, and hence reduce the extensively performed animal experiments [195, 196]. Depending on the constituting cells and culturing conditions, multicellular spheroids could mimic several pathological hallmarks of lung cancer, such as inter-cell signaling, hypoxic core formation, immunosuppression, dense extracellular matrix (ECM) formation, clonal heterogeneity, and expression of cancer-specific markers [197].

Lung cancer multicellular spheroids can be produced from the monoculture of a cancer cell line, yielding a simple homotypic spheroid model. Alternatively, heterotypic spheroids can be generated from the co-culture of cancer cells with one or more other cell types, such as immune cells, fibroblasts and other stromal cells, providing a better representation for the complex tumor microenvironment (TME) [197]. One main element of the TME is the ECM, which is strongly connected to chemoresistance; by raising the interstitial pressure within the tumor stroma and limiting the permeation of therapeutic agents into the tumor mass [25, 26, 38, 198]. Cancer associated fibroblasts are majorly responsible for the secretion and remodeling of tumor-specific ECM, that actively contributes to tumor initiation, angiogenesis, tumor promotion, metastasis, and chemotherapeutic resistance [199]. Co-culturing of fibroblasts in lung cancer spheroid models was depicted to cause a remarkable increase in the expression of certain ECM components, including collagen type I [200], and produce more treatment-resistant lung cancer spheroids [201].

In the current work, we explored the formation of lung cancer spheroids through co-culturing of human lung adenocarcinoma cells (A549) with human lung fibroblasts (MRC-5). This model was utilized as an ECM-expressing lung adenocarcinoma model for the evaluation of the collagenase-containing acetalated maltodextrin (AcMD) nano-structured microparticles (MPs), presented in the previous chapter. The spheroid growth was monitored via measuring the spheroid size and shape determinants, i.e., diameter and circularity respectively, over the spheroid culturing duration. Before conducting the penetration experiments on the spheroids, the selection of collagenase content and formulation concentration was first based on the viability assessment on both A549 and MRC-5 cells independently. The choice was further refrained through testing the changes in spheroid size and shape. Finally, we evaluated the penetration of the rhodamine-labeled AcMD-NPs (Rhod-AcMD-NPs) with and without collagenase as a constituent of the microparticle formulation.

8.2   Materials and methods

8.2.1   Materials

Maltodextrin (DE: 13.0-17.0), 2-methoxypropene, pyridinium *p*-toluene sulfonate (PPTS), triethylamine (TEA), 1,8-diazabicyclo[5.4.0]undec-7-ene (DBU), L-leucine, collagenase (obtained from Clostridium histolyticum, Type I), RPMI-1640 cell culture medium, Dulbecco's phosphate buffered saline (DPBS), trypsin-EDTA, penicillin-streptomycin and thiazolyl blue tetrazolium bromide were purchased from Sigma-Aldrich (Steinheim, Germany). Poloxamer 407 was purchased from Caesar and Loretz GmbH (Hilden, Germany). Trehalose was purchased from Carl Roth (Karlsruhe, Germany). NHS-rhodamine, 4′,6-diamidino-2-phenylindole (DAPI), Gibco™ MEM α (Glutamax™ Supplement) cell culture medium, Gibco™ Opti-MEM™ serum reduced medium, and fetal bovine serum (FBS) were purchased from Thermo Fisher Scientific (Darmstadt, Germany). Dimethyl sulfoxide (DMSO, analytical grade), acetone and ethanol (HPLC grade) were purchased from Fisher Scientific (Schwerte, Germany). All the other reagents used were purchased with HPLC or analytical grade.

8.2.2 Preparation of AcMD-NPs and nano-structured MPs

AcMD-NPs were prepared as described in **chapter II, section 6.2.3** using AcMDB at 25 mg/ml polymer solution concentration. Fluorescent AcMD-NPs (Rhod-AcMD$_{180}$-NPs) were prepared by the same procedure using Rhod-AcMDB$_{180}$ **(Chapter I, section 5.2.3)**. Collagenase-free (NP$_{20}$L$_{30}$) and collagenase-containing (NP$_{20}$L$_{30}$C$_{10}$, NP$_{20}$L$_{30}$C$_{30}$ and NP$_{20}$L$_{30}$C$_{50}$) AcMD nano-structured MPs were prepared as described in **chapter III, section 7.2.3**.

8.2.3 Cell culture

Adenocarcinoma human alveolar epithelial cells (A549) were cultured in RPMI-1640 medium supplemented with 10% FBS. Human fetal lung fibroblasts (MRC-5) were cultured in MEM α medium with GlutaMAX™, supplemented with 10% FBS. The cells were subcultured once a week and the media were replaced with fresh media every other day. The cultures were maintained at 37 °C temperature in a humidified atmosphere containing 5% CO_2 (BD 260 Standard Incubator, Binder, Tuttlingen, Germany). A549 cells were used within passages 6 and 20 and MRC-5 cells were used within passages 3 and 10.

8.2.4 Cell viability assay

The effect of AcMD nano-structured MPs on cell viability was evaluated using MTT assay on A549 and MRC-5 2D cultures. A549 and MRC-5 cells were seeded into 96-well plates (20,000 and 40,000 cells/200 μl/well, respectively) and grown for 48 h. Afterwards, media were replaced with fresh media containing the tested microparticles at different concentrations (100, 250, 500, 750 and 1000 µg/ml) and supplemented with 100 U/ml penicillin-streptomycin. Samples were tested against negative and positive controls, in which cells were treated with medium and 2% Triton-X, respectively. After 24 h incubation with the formulations, media were removed, cells were washed with DPBS and incubated with 10% MTT reagent for 4 h. This was followed by aspiration and incubation with DMSO for 20 min to dissolve formazan crystals formed by living cells. Absorbance of formed formazan by live cells was measured at 550 nm and cell viability was calculated according to **equation 5 (Chapter II, section 6.2.7.2)**. The experiments were performed in triplicates.

8.2.5 Formation of spheroids

Spheroids were produced by adopting liquid overlay technique in ultra-low adhesion 96-well plates (Nuclon™ Sphera™ 96-well U-shaped-bottom microplates, Thermo Scientific). A549 and MRC-5 monoculture as well as co-culture spheroids were grown. The cells were seeded at 2000 cells/100 μl/well. For monoculture spheroids, the seeded cells were 100% A549 or MRC-5 cells. For co-culture spheroids, the seeding ratio of A549 to MRC-5 cells was 30:70 and cell seeding was performed sequentially, where A549 cells were seeded first, followed by MRC-5 cells after 24 h [202]. The spheroids were allowed to grow for 10 days. The media were renewed by adding 100 μl fresh media at day 5 and exchanging 100 μl at day 8. For all the spheroid experiments, the media were supplemented by 100 U/ml penicillin-streptomycin.

8.2.6 Size and circularity measurements

To monitor the spheroid growth, bright field images were recorded at day 2, 3, 5, 8 and 10 (LSM 710, Carl Zeiss AG, Jena, Germany) using 10x objective. Spheroid diameter was determined as the average of 3 diameters measured for each spheroid using ImageJ software. The circularity parameter was measured by the aid of ImageJ software, where it is calculated based on **equation 10** [203]. Six spheroids were examined for each experiment.

$$Circularity = 4\pi \left(\frac{area}{perimeter^2} \right) \qquad \text{Equation 10}$$

8.2.7 Application of treatments to the spheroids

After the spheroids were grown for 10 days, the medium was washed once with DPBS and once with opti-MEM medium through exchanging 150 μl in each washing step. Subsequently, the microparticle components were added at a concentration of 1 mg/ml in opti-MEM medium and allowed to incubate with the spheroids for 4 h. Afterwards, the spheroids were washed twice with opti-MEM medium, and NPs alone were re-applied at the same concentration. Two controls were used at this experiment, a negative control in which the spheroids were treated with opti-MEM medium (referred to as medium control), and a

collagenase-negative control, in which the spheroids were treated with collagenase-free formulation. The incubation was allowed to continue till a total duration of 24 h.

8.2.8 Spheroid fixation and staining

After incubating the spheroids with the treatments, they were washed twice with DPBS. The spheroids were fixed with 4% paraformaldehyde for 30 min at room temperature then washed twice with DPBS. Nuclei were stained with DAPI for 1 h, followed by 2 washing steps with DPBS. In each washing and addition step, 150 μl were exchanged.

8.2.9 Effect of collagenase on the integrity of spheroids

Bright field images (LSM 710, Carl Zeiss AG, Jena, Germany) using 10x objective were recorded for the fixed spheroids and the diameters were measured as described. To test the effect of collagenase on the integrity of spheroids, the diameter and circularity of the spheroids treated with collagenase-free and collagenase-containing formulations were compared to the medium control spheroids.

8.2.10 Evaluation of nanoparticle penetration

The spheroids were visualized with confocal laser scanning microscope (CLSM) (LSM 710, Carl Zeiss AG, Jena, Germany) using 10x objective. The signals of DAPI and rhodamine were detected through excitation at 405 and 561 nm and recording emission at 410-507 and 566-703 nm, respectively. In confocal mode, the first and last planes at which cells could be observed (guided by DAPI signal) were used as the first and last visualization constraints. Through this determined depth, the rhodamine signal in 4 optical sections at equal steps (approximately 40 μm apart from each other according to the individual spheroid dimensions) was recorded. The medium control spheroids were used as a blank for setting the microscopical settings. Image processing was performed using ZEN 3.0 (blue edition) software (Carl Zeiss Microscopy, 2019). The fluorescence intensity in the consecutive planes were assessed and compared for the collagenase-free and the collagenase-containing formulations. The corrected total fluorescence (CTF) and normalized CTF were calculated using the integrated density (IntDen) and surface area (A) measured by ImageJ for the individual cross sections as follows:

$$CTF = IntDen - (Mean\ background\ fluorescence \times A) \qquad \text{Equation 11}$$

$$Normalized\ CTF = \frac{CTF}{A} \qquad \text{Equation 12}$$

8.2.11 Statistical analysis

The results are described as mean values $\pm$ standard deviation. Statistical significance was tested using one-way analysis of variance (ANOVA), followed by Bonferroni *post hoc* test to compare all pairs. The level of significance was set at a *p*-value of 0.05. Statistical analysis was implemented using GraphPad Prism (version 8.0.2) software (GraphPad Software, 2019).

8.3   Results and discussion

8.3.1   Cell viability assay

The effect of AcMD nano-structured MPs containing increasing amounts of collagenase ($NP_{20}L_{30}C_{10}$, $NP_{20}L_{30}C_{30}$ and $NP_{20}L_{30}C_{50}$) on the viability of the two cell lines used in this study: A549 and MRC-5 cells, was tested using MTT viability assay on 2D monocultures. Similar to the collagenase-free AcMD nano-structured MPs ($NP_{20}L_{30}$), $NP_{20}L_{30}C_{10}$ did not show signs of cytotoxicity even at high application concentrations on both tested cell lines **(Figure 28)**. However, increasing the collagenase content to 30% caused the viable fraction of MRC-5 cells to drop below 80% at 1000 μg/ml concentration **(Figure 28b)**, where a viability of 80% is often considered as the lower limit for claiming non-cytotoxicity [204]. Further, $NP_{20}L_{30}C_{50}$ was toxic to both cell lines at concentrations higher than 500 μg/ml **(Figure 28a and b)**. Aside from collagenase, the MPs' constituents, including the AcMD-NPs [205], are not assumed to induce cell toxicity. Collagenase was reported to induce toxicities in animals at doses exceeding 500 μg [206, 207]. To maximize the amount of the delivered AcMD-NPs, using the formulation with the least collagenase content ($NP_{20}L_{30}C_{10}$) at the highest application concentration (1000 μg /ml) was selected for subsequent testing.
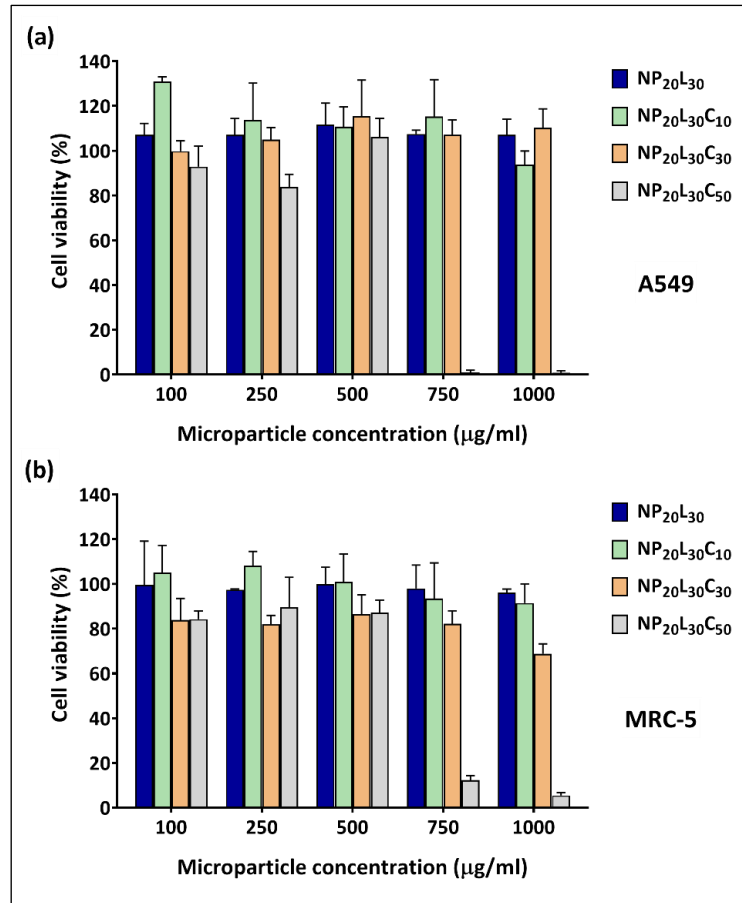
Figure 28. Cell viability of (a) A549 cells and (b) MRC-5 fibroblasts after 24 h incubation with NP$_{20}$L$_{30}$, NP$_{20}$L$_{30}$C$_{10}$, NP$_{20}$L$_{30}$C$_{30}$, and NP$_{20}$L$_{30}$C$_{50}$ spray dried nano-structured MPs at increasing concentrations (100 – 1000 μg/ml), determined using MTT assay. The data represents mean values $\pm$ standard deviation from n = 3 independent experiments.

8.3.2 Spheroid formation and growth

Different seeding densities (from 1000 to 4000 cells/100 μl/well) were preliminary experimented (data not shown) and 2000 cells/100 μl/well was found suitable to produce the required spheroids with diameters exceeding 500 μm at 10th day of growth. Spheroids of diameters larger than 500 μm are generally regarded as representative models for solid tumors, exhibiting their characteristic proliferation gradients of a central necrotic core, surrounded by viable quiescent cells, and finally proliferating cells at the periphery [208]. Co-culturing the fibroblasts at 70% (compared to 50 and 90%) of the seeded cells was also

found to yield a good compromise regarding the growth rate and circularity (data not shown), where the circularity was set as an indicative for the spheroid compactness [209].

The influence of the MRC-5 fibroblasts on the spheroid development can be clearly observed in **figure 29**. At the second day of growth prior to the addition of fibroblasts, a loose cell aggregation with undefined shape was detected **(Figure 29a)**. The spheroid morphology was eminently altered by the fibroblast seeding; the loose aggregates were transformed into tight and perfectly spherical spheroids at the third day of growth **(Figure 29a)**, displaying a gradual increase in diameter **(Figure 30a)** and yet a preserved circular shape over the growth period **(Figure 30b)**. The development pattern of the A549 monoculture spheroids was dissimilar to that of the co-culture spheroids **(Figure 29b)**. Loose, large, and irregular-shaped aggregates were initially formed, that gradually got denser and tighter over the growth period, with a less notable increase in diameter **(Figure 30a)** and an improving circularity **(Figure 30b)**. On the other hand, the MRC-5 monoculture spheroids were highly compact and small in diameters irrespective of the incubation time **(Figure 29c)**. This may be explained by the longer doubling time and the limited doubling cycles of the non-malignant MRC-5 cells, restricting their 3D culturing (related finding was reported by Yakavets et al. [202]). As a whole, the results depicts the impact of cell type, seeding and culturing conditions on the characteristics of the produced spheroids [203, 210].
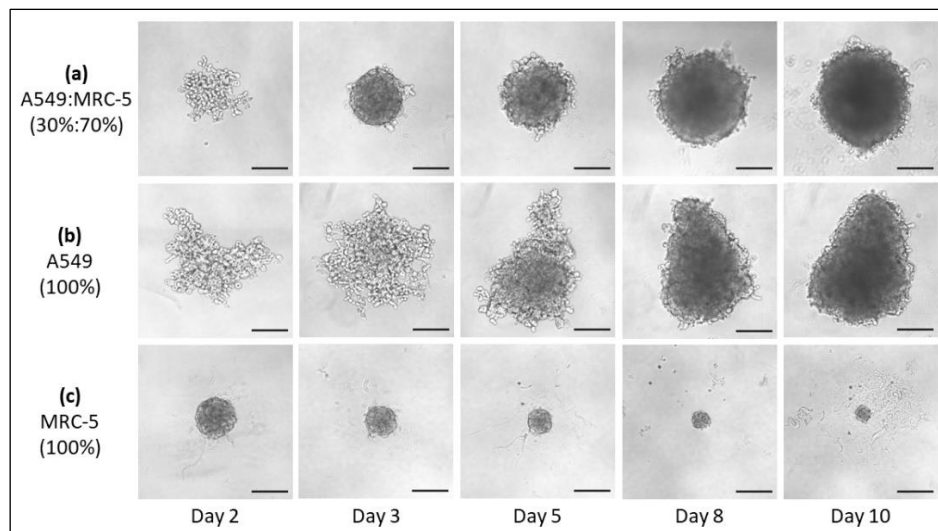
Figure 29. Bright field images of (a) A549:MRC-5 (30%:70%), (b) A549 (100%), and MRC-5 (100%) spheroids on day 2, 3, 5, 8, and 10 of spheroid growth. Scale bar in all pictures equals to 200 μm.
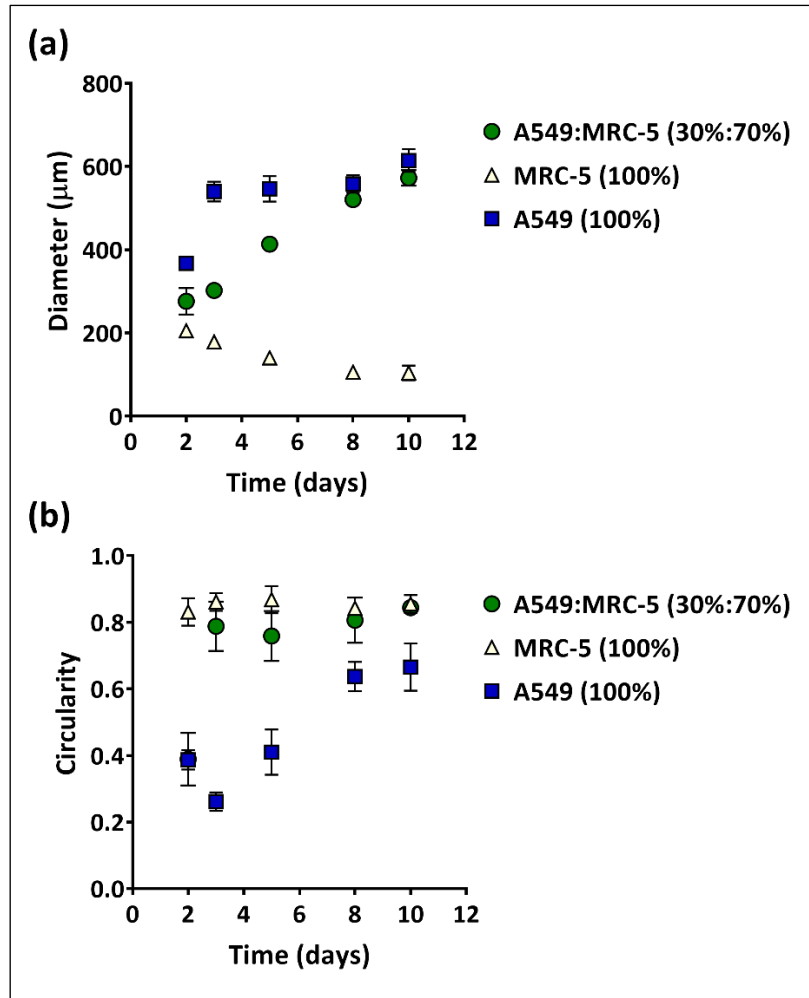
Figure 30. (a) Diameter and (b) circularity of co-culture and monoculture spheroids over 10 days of spheroid growth. The results represent mean ± standard deviation of 6 independent replicates.

8.3.3   Effect of collagenase on spheroid integrity

Based on the cell viability testing, it was concluded that applying $NP_{20}L_{30}C_{10}$ at 1 mg/ml concentration (effective concentration of collagenase is 0.1 mg/ml) was well tolerated by both A549 and MRC-5 cells. However, the effect of the ECM-degrading collagenase on the architecture of the spheroids is an additional main concern, where considerable detachment of cancer cells from the spheroid surface may correspond to metastasis [174]. Therefore, we evaluated the application of collagenase at 0.1, as well as 0.05 mg/ml concentrations (denoted as $NP_{20}L_{30}C_{10}$ and $NP_{20}L_{30}C_{05}$, respectively). **Figure 31a** shows that the two tested collagenase concentrations caused a slight decrease in the spheroid diameter,

which was statistically significant in case of the higher concentration. The significant change in circularity in case of the higher concentration **(Figure 31b)** also implies a certain degree of deformation due to cell loosening or separation. The effects encountered may also be ascribed to the periphery of the spheroids being less rich in fibroblasts and hence in ECM, i.e., more prone to collagenase treatment. Although sequential seeding was carried out to circumvent this problem, it is speculated to improve the fibroblasts distribution only to a certain extent and render it more homogenous. Nevertheless, the lower collagenase concentration was regarded as apt to apply on the spheroids with no significant degenerating effects.
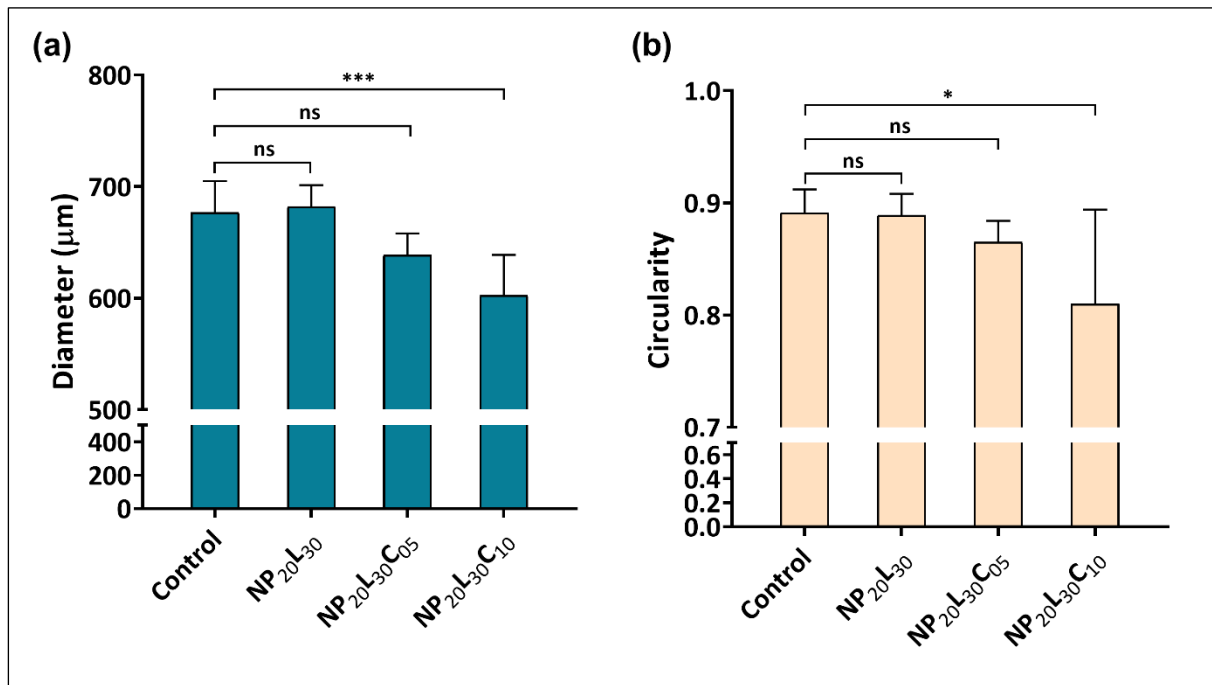
Figure 31. (a) Diameter and (b) circularity of the spheroids after incubation with collagenase-free (NP$_{20}$L$_{30}$) and collagenase-containing (NP$_{20}$L$_{30}$C$_{05}$ and NP$_{20}$L$_{30}$C$_{10}$) formulation constituents relative to medium control spheroids. The results represent mean ± standard deviation of 6 independent replicates. ***: $p = 0.0003$, *: $p = 0.0171$, and ns: $p > 0.05$.

8.3.4   Evaluation of particle penetration

Figure 32 demonstrates that nanoparticle fluorescence detected in the z-stack planes was more intense in case of the combined treatment of collagenase with Rhod-AcMD-NPs

relative to the sole nanoparticle application (more obvious in the middle planes). This qualitative result was verified by the quantitative measurement of the fluorescent intensity of the sections, of which the results are displayed in **figure 33**. Despite the comparable fluorescence in the outer-most plane, collagenase could effectively increase the penetration of Rhod-AcMD-NPs through the spheroids to reach a depth of 120 μm. The outer-most layer is mainly comprised of actively proliferating cells and hence the particles could have been included or uptaken during the cell division. The last examined plane showed more fluorescence in the collagenase-treated sample, but the difference was not significant between the two treatments, which may be as well ascribed to the limited visualization ability of CLSM in deeper tissue sections [211].
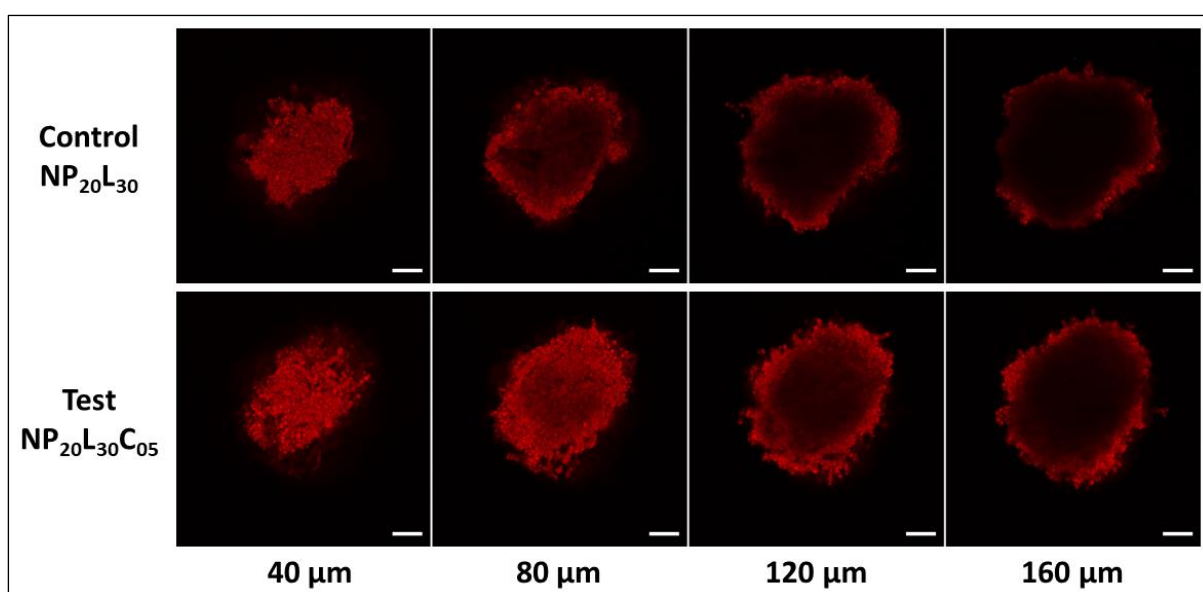
Figure 32. Z-stack images of successive optical sections recorded at ≈ 40 μm steps. Upper and lower panels display sections of spheroids treated with NP$_{20}$L$_{30}$ (collagenase-free) and NP$_{20}$L$_{30}$C$_{05}$ (collagenase-containing) formulation components, respectively. Red signal corresponds to rhodamine in Rhod-AcMD-NPs. Scale bars are equivalent to 100 μm.
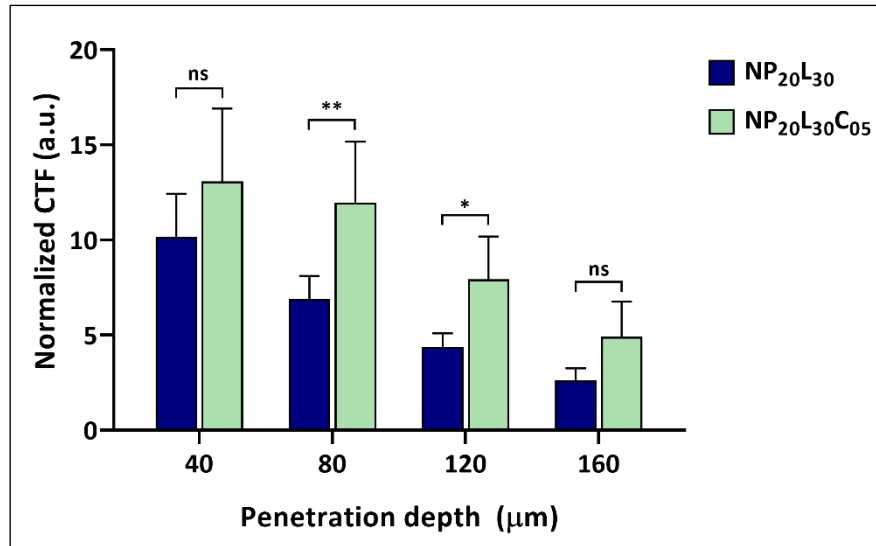
Figure 33. The normalized CTF recorded from the different planes of spheroids ranging from 40 to 160 μm depth after incubation with NP$_{20}$L$_{30}$ (collagenase-free) and NP$_{20}$L$_{30}$C$_{05}$ (collagenase-containing) formulation constituents. The results represent mean $\pm$ standard deviation of 6 independent replicates. **: p = 0.0014, *: p = 0.0386 and, ns: p > 0.05.

8.4 Conclusion

The inclusion of collagenase in the nano-structured microparticle formulation was depicted to enhance the penetration of AcMD-NPs into the utilized spheroid model. In other words, our proposed formulation strategy enabled the delivery of higher amount of AcMD-NPs into deeper areas of the spheroids. Considering that the tested AcMD-NPs are relatively large ($\approx$ 170 - 180 nm), the penetration could probably be further improved by decreasing the particle size of the embedded NPs. Interestingly, partial degradation of AcMD-NPs in acidic tumor microenvironment (TME) may result in decreasing their particle size and improving their diffusion through the ECM network. However, premature extracellular drug release should be avoided, which demands further formulation optimization and biological evaluation. The design of the carrier system introduced in this work opens several pathways for future studies investigating therapeutics effects. The dual enhancing impact of ECM modulation and nanoparticle acid-degradability on the delivery efficacy of chemotherapeutics would potentially attain the anticipated treatment outcomes.

General conclusion and future perspectives

9. General conclusion and future perspectives

Throughout the work presented in this thesis, an inhalable composite delivery system was developed aiming to optimize drug delivery for lung cancer treatment and enhance the penetration of therapeutics into adenocarcinoma solid tumors. We attempted to fulfill this goal through successive work packages presented in the thesis chapters, starting from synthesis and characterization of the nanoparticle constituting polymer **(Chapter I)**, followed by optimization of nanoparticle formation, characterizing their properties as nanocarriers, and investigating their interaction with cell lines of interest **(Chapter II)**. To enable adequate pulmonary deposition and enhance the intratumoral delivery, the developed nanoparticles were afterwards aggregated into nano-structured microparticles comprising collagenase **(Chapter III)**. Finally, the developed nano-structured microparticles were evaluated using *in vitro* adenocarcinoma spheroid model **(Chapter IV)**.

With the advantages of being naturally abundant, non-toxic, and economic to produce, maltodextrin (MD) was selected for nanoparticle formation. Maltodextrin of different dextrose equivalents was chemically modified through acetalation to acetalated maltodextrin (AcMD). This modification is associated with reversing its solubility property from water-soluble to hydrophobic and imparting it pH-responsive degradation behavior. By increasing the reaction time, AcMDs with increasing cyclic to acyclic acetal ratio were produced. The molecular weight of the produced AcMD polymers is higher than the parent MDs due to the addition of acetal moieties, whereas the molecular weight distribution is similarly broad. Thermogravimetric analysis and glass transition temperature determination revealed lower decomposition onset temperature and glass transition temperature of AcMD with respect to MD. The studied polymer characteristics are essential upon exploiting AcMD for the development of drug carriers, where it could be subjected to immoderate processing conditions with undesirable effects.

Through comprehensive investigation of the factors affecting nanoparticle formation, monodisperse AcMD nanoparticles were produced with high production yields, regardless of the AcMD molecular weight heterogeneity. The AcMD nanoparticles were demonstrated to maintain their integrity at physiological pH (7.4) and degrade at slightly

acidic pH (5.0), where the degradation kinetics are not influenced by molecular weight and significantly affected by cyclic to acyclic acetal ratio of AcMD. The AcMD nanoparticles were proven to be adequate drug nanocarriers; (1) they could be loaded with resveratrol as a model hydrophobic drug with acceptable drug loading and entrapment efficiency, (2) they showed pH-dependent tunable *in vitro* release of resveratrol, and (3) they induced no cytotoxicity upon being tested on lung adenocarcinoma A549 cells and differentiated THP-1 monocytes, as examples of somatic and immune cells, respectively. Therefore, the AcMD nanoparticles are very promising carriers for anticancer drugs, that are mostly hydrophobic molecules, with their aforementioned features and exhibited considerable uptake in lung adenocarcinoma A549 cells.

AcMD nano-structured microparticles were afterwards developed by spray drying AcMD nanoparticles with trehalose and leucine as matrix forming agents. Collagenase was loaded into the microparticle matrix to enhance the delivery of AcMD nanoparticles through circumventing the dense extracellular matrix in solid tumors. Importantly, the enzymatic activity of collagenase was largely retained after spray drying. The collagenase-loaded nano-structured microparticles exhibited good redispersibility into nanoparticles upon hydration and optimally low residual moisture content. The assessed aerodynamic properties were adequate for deposition in the bronchioloalveolar region, which is the pulmonary region of interest in adenocarcinoma. The microparticles with low collagenase content were highly tolerable to A549 cells and lung MRC-5 fibroblasts with no notable cytotoxicity, indicating their biological applicability. The inclusion of collagenase was found to improve the penetration of AcMD nanoparticles in the utilized lung adenocarcinoma spheroid model with respect to the collagenase-free formulation.

Based on the findings disclosed and discussed throughout the current work, the following points are raised for perspective investigation:

- Extending the nanoprecipitation production of AcMD nanoparticles to other platforms, for example microfluidics, that could produce particles with smaller diameters and accordingly better diffusion and penetration properties.

- Decorating the surface of AcMD with targeting ligands to accelerate the specific uptake in lung cancer cells and reaching the intracellular targets, before being cleared by pulmonary macrophages.

- Studying the nanoparticle uptake and/or the therapeutic efficacy of AcMD nanoparticles loaded with a cytotoxic agent (also with targeting ligands) in normal physiological and slightly acidic pH conditions, where different acid-triggered degradation and cellular uptake kinetics are expected to have complex effects.

- Evaluating the nano-structured microparticle physical stability and collagenase enzymatic activity after long-term storage.

- Investigating the therapeutic effects of collagenase-containing AcMD nano-structured microparticles after loading them with a chemotherapeutic agent on spheroid models or *in vivo* animal models for the promising formulations.

References

10.   References

[1] J. Ferlay, M. Colombet, I. Soerjomataram, D.M. Parkin, M. Piñeros, A. Znaor, F. Bray, Cancer statistics for the year 2020: An overview, International Journal of Cancer, 149 (2021) 778-789.

[2] H. Sung, J. Ferlay, R.L. Siegel, M. Laversanne, I. Soerjomataram, A. Jemal, F. Bray, Global Cancer Statistics 2020: GLOBOCAN Estimates of Incidence and Mortality Worldwide for 36 Cancers in 185 Countries, CA: A Cancer Journal for Clinicians, 71 (2021) 209-249.

[3] C.S. Dela Cruz, L.T. Tanoue, R.A. Matthay, Lung cancer: epidemiology, etiology, and prevention, Clinics in chest medicine, 32 (2011) 605-644.

[4] B.C. Bade, C.S. Dela Cruz, Lung Cancer 2020: Epidemiology, Etiology, and Prevention, Clinics in chest medicine, 41 (2020) 1-24.

[5] N. Duma, R. Santana-Davila, J.R. Molina, Non–Small Cell Lung Cancer: Epidemiology, Screening, Diagnosis, and Treatment, Mayo Clinic Proceedings, 94 (2019) 1623-1640.

[6] K. Inamura, Lung Cancer: Understanding Its Molecular Pathology and the 2015 WHO Classification, Front Oncol, 7 (2017) 193.

[7] S. Blandin Knight, P.A. Crosbie, H. Balata, J. Chudziak, T. Hussell, C. Dive, Progress and prospects of early detection in lung cancer, Open biology, 7 (2017).

[8] M.G. Raso, N. Bota-Rabassedas, Wistuba, II, Pathology and Classification of SCLC, Cancers, 13 (2021).

[9] S. Qu, P. Fetsch, A. Thomas, Y. Pommier, D.S. Schrump, M.M. Miettinen, H. Chen, Molecular Subtypes of Primary SCLC Tumors and Their Associations With Neuroendocrine and Therapeutic Markers, Journal of Thoracic Oncology, 17 (2022) 141-153.

[10] A. Schwendenwein, Z. Megyesfalvi, N. Barany, Z. Valko, E. Bugyik, C. Lang, B. Ferencz, S. Paku, A. Lantos, J. Fillinger, M. Rezeli, G. Marko-Varga, K. Bogos, G. Galffy, F. Renyi-Vamos, M.A. Hoda, W. Klepetko, K. Hoetzenecker, V. Laszlo, B. Dome, Molecular profiles of small cell lung cancer subtypes: Therapeutic implications, Molecular Therapy - Oncolytics, 20 (2021) 470-483.

[11] A.G. Nicholson, M.S. Tsao, M.B. Beasley, A.C. Borczuk, E. Brambilla, W.A. Cooper, S. Dacic, D. Jain, K.M. Kerr, S. Lantuejoul, M. Noguchi, M. Papotti, N. Rekhtman, G. Scagliotti, P. van Schil, L. Sholl, Y. Yatabe, A. Yoshida, W.D. Travis, The 2021 WHO Classification of Lung Tumors: Impact of Advances Since 2015, Journal of Thoracic Oncology, 17 (2022) 362-387.

[12] Z. Khodabakhshi, S. Mostafaei, H. Arabi, M. Oveisi, I. Shiri, H. Zaidi, Non-small cell lung carcinoma histopathological subtype phenotyping using high-dimensional multinomial multiclass CT radiomics signature, Computers in Biology and Medicine, 136 (2021) 104752.

[13] W.D. Travis, E. Brambilla, A.G. Nicholson, Y. Yatabe, J.H.M. Austin, M.B. Beasley, L.R. Chirieac, S. Dacic, E. Duhig, D.B. Flieder, K. Geisinger, F.R. Hirsch, Y. Ishikawa, K.M. Kerr, M. Noguchi, G. Pelosi, C.A. Powell, M.S. Tsao, I. Wistuba, The 2015 World Health Organization Classification of Lung Tumors: Impact of Genetic, Clinical and Radiologic Advances Since the 2004 Classification, Journal of Thoracic Oncology, 10 (2015) 1243-1260.

[14] M. Zheng, Classification and Pathology of Lung Cancer, Surgical oncology clinics of North America, 25 (2016) 447-468.

[15] N. Alhajj, C.F. Chee, T.W. Wong, N.A. Rahman, N.H. Abu Kasim, P. Colombo, Lung cancer: active therapeutic targeting and inhalational nanoproduct design, Expert Opinion on Drug Delivery, 15 (2018) 1223-1247.

[16] C. Zappa, S.A. Mousa, Non-small cell lung cancer: current treatment and future advances, Translational lung cancer research, 5 (2016) 288-300.

[17] H. Lemjabbar-Alaoui, O.U.I. Hassan, Y.-W. Yang, P. Buchanan, Lung cancer: Biology and treatment options, Biochimica et Biophysica Acta (BBA) - Reviews on Cancer, 1856 (2015) 189-210.

[18] E. Felip, R. Rosell, J.A. Maestre, J.M. Rodríguez-Paniagua, T. Morán, J. Astudillo, G. Alonso, J.M. Borro, J.L. González-Larriba, A. Torres, C. Camps, R. Guijarro, D. Isla, R. Aguiló, V. Alberola, J. Padilla, A. Sánchez-Palencia, J.J. Sánchez, E. Hermosilla, B. Massuti, Preoperative chemotherapy plus surgery versus surgery plus adjuvant chemotherapy versus surgery alone in early-stage non-small-cell lung cancer, Journal of clinical oncology : official journal of the American Society of Clinical Oncology, 28 (2010) 3138-3145.

[19] J.P. Pignon, H. Tribodet, G.V. Scagliotti, J.Y. Douillard, F.A. Shepherd, R.J. Stephens, A. Dunant, V. Torri, R. Rosell, L. Seymour, S.G. Spiro, E. Rolland, R. Fossati, D. Aubert, K. Ding, D. Waller, T. Le Chevalier, Lung adjuvant cisplatin evaluation: a pooled analysis by the LACE Collaborative Group, Journal of clinical oncology : official journal of the American Society of Clinical Oncology, 26 (2008) 3552-3559.

[20] H. Weaver, A.S. Coonar, Lung cancer: diagnosis, staging and treatment, Surgery (Oxford), 35 (2017) 247-254.

[21] K.A. Ruiz-Ceja, Y.I. Chirino, Current FDA-approved treatments for non-small cell lung cancer and potential biomarkers for its detection, Biomedicine & pharmacotherapy = Biomedecine & pharmacotherapie, 90 (2017) 24-37.

[22] T.R. Cox, The matrix in cancer, Nature reviews. Cancer, 21 (2021) 217-238.

[23] C. Bonnans, J. Chou, Z. Werb, Remodelling the extracellular matrix in development and disease, Nature Reviews Molecular Cell Biology, 15 (2014) 786-801.

[24] K.C. Valkenburg, A.E. de Groot, K.J. Pienta, Targeting the tumour stroma to improve cancer therapy, Nature reviews. Clinical oncology, 15 (2018) 366-381.

[25] J. Huang, L. Zhang, D. Wan, L. Zhou, S. Zheng, S. Lin, Y. Qiao, Extracellular matrix and its therapeutic potential for cancer treatment, Signal Transduction and Targeted Therapy, 6 (2021) 153.

[26] N. Subrahmanyam, H. Ghandehari, Harnessing Extracellular Matrix Biology for Tumor Drug Delivery, Journal of personalized medicine, 11 (2021).

[27] T. Rozario, D.W. DeSimone, The extracellular matrix in development and morphogenesis: a dynamic view, Developmental biology, 341 (2010) 126-140.

[28] K.M. Yamada, J.W. Collins, D.A. Cruz Walma, A.D. Doyle, S.G. Morales, J. Lu, K. Matsumoto, S.S. Nazari, R. Sekiguchi, Y. Shinsato, S. Wang, Extracellular matrix dynamics in cell migration, invasion and tissue morphogenesis, International journal of experimental pathology, 100 (2019) 144-152.

[29] M.J. Bissell, H.G. Hall, G. Parry, How does the extracellular matrix direct gene expression?, Journal of theoretical biology, 99 (1982) 31-68.

[30] F. Kai, A.P. Drain, V.M. Weaver, The Extracellular Matrix Modulates the Metastatic Journey, Developmental cell, 49 (2019) 332-346.

[31] C.T. Mierke, Mechanical Cues Affect Migration and Invasion of Cells From Three Different Directions, Frontiers in cell and developmental biology, 8 (2020) 583226.

[32] M.W. Pickup, J.K. Mouw, V.M. Weaver, The extracellular matrix modulates the hallmarks of cancer, EMBO reports, 15 (2014) 1243-1253.

[33] T.R. Cox, J.T. Erler, Molecular pathways: connecting fibrosis and solid tumor metastasis, Clinical cancer research : an official journal of the American Association for Cancer Research, 20 (2014) 3637-3643.

[34] B. Piersma, M.K. Hayward, V.M. Weaver, Fibrosis and cancer: A strained relationship, Biochimica et biophysica acta. Reviews on cancer, 1873 (2020) 188356.

[35] S. Ricard-Blum, The collagen family, Cold Spring Harbor perspectives in biology, 3 (2011) a004978.

[36] S. Xu, H. Xu, W. Wang, S. Li, H. Li, T. Li, W. Zhang, X. Yu, L. Liu, The role of collagen in cancer: from bench to bedside, J Transl Med, 17 (2019) 309.

[37] M. Fang, J. Yuan, C. Peng, Y. Li, Collagen as a double-edged sword in tumor progression, Tumour biology : the journal of the International Society for Oncodevelopmental Biology and Medicine, 35 (2014) 2871-2882.

[38] X. Xu, Y. Wu, X. Qian, Y. Wang, J. Wang, J. Li, Y. Li, Z. Zhang, Nanomedicine Strategies to Circumvent Intratumor Extracellular Matrix Barriers for Cancer Therapy, Advanced Healthcare Materials, 11 (2022) 2101428.

[39] A.I. Minchinton, I.F. Tannock, Drug penetration in solid tumours, Nature reviews. Cancer, 6 (2006) 583-592.

[40] R.K. Jain, T. Stylianopoulos, Delivering nanomedicine to solid tumors, Nature reviews. Clinical oncology, 7 (2010) 653-664.

[41] K.P. Olive, M.A. Jacobetz, C.J. Davidson, A. Gopinathan, D. McIntyre, D. Honess, B. Madhu, M.A. Goldgraben, M.E. Caldwell, D. Allard, K.K. Frese, G. Denicola, C. Feig, C. Combs, S.P. Winter, H. Ireland-Zecchini, S. Reichelt, W.J. Howat, A. Chang, M. Dhara, L. Wang, F. Rückert, R. Grützmann, C. Pilarsky, K. Izeradjene, S.R. Hingorani, P. Huang, S.E. Davies, W. Plunkett, M. Egorin, R.H. Hruban, N. Whitebread, K. McGovern, J. Adams, C. Iacobuzio-Donahue, J. Griffiths, D.A. Tuveson, Inhibition of Hedgehog signaling enhances delivery of chemotherapy in a mouse model of pancreatic cancer, Science (New York, N.Y.), 324 (2009) 1457-1461.

[42] A. Pluen, Y. Boucher, S. Ramanujan, T.D. McKee, T. Gohongi, E. di Tomaso, E.B. Brown, Y. Izumi, R.B. Campbell, D.A. Berk, R.K. Jain, Role of tumor-host interactions in interstitial diffusion of macromolecules: cranial vs. subcutaneous tumors, Proceedings of the National Academy of Sciences of the United States of America, 98 (2001) 4628-4633.

[43] R.K. Verma, M. Ibrahim, L. Garcia-Contreras, Lung Anatomy and Physiology and Their Implications for Pulmonary Drug Delivery, Pulmonary Drug Delivery2015, pp. 1-18.

[44] B. Chaurasiya, Y.Y. Zhao, Dry Powder for Pulmonary Delivery: A Comprehensive Review, Pharmaceutics, 13 (2020).

[45] P. Muralidharan, M. Malapit, E. Mallory, D. Hayes, H.M. Mansour, Inhalable nanoparticulate powders for respiratory delivery, Nanomedicine: Nanotechnology, Biology and Medicine, 11 (2015) 1189-1199.

[46] W. Hofmann, Modelling inhaled particle deposition in the human lung—A review, Journal of Aerosol Science, 42 (2011) 693-724.

[47] Y.S. Khan, D.T. Lynch, Histology, Lung, StatPearls, StatPearls Publishing

Copyright © 2023, StatPearls Publishing LLC., Treasure Island (FL) ineligible companies. Disclosure: David Lynch declares no relevant financial relationships with ineligible companies., 2023.

[48] J. Heyder, J. Gebhart, G. Rudolf, C.F. Schiller, W. Stahlhofen, Deposition of particles in the human respiratory tract in the size range 0.005–15 µm, Journal of Aerosol Science, 17 (1986) 811-825.

[49] J. Heyder, Alveolar deposition of inhaled particles in humans, American Industrial Hygiene Association Journal, 43 (1982) 864-866.

[50] J. Heyder, Deposition of inhaled particles in the human respiratory tract and consequences for regional targeting in respiratory drug delivery, Proceedings of the American Thoracic Society, 1 (2004) 315-320.

[51] J. Heyder, Particle transport onto human airway surfaces, European journal of respiratory diseases. Supplement, 119 (1982) 29-50.

[52] C.S. Kim, S.C. Hu, Regional deposition of inhaled particles in human lungs: comparison between men and women, Journal of applied physiology (Bethesda, Md. : 1985), 84 (1998) 1834-1844.

[53] M. Lippmann, D.B. Yeates, R.E. Albert, Deposition, retention, and clearance of inhaled particles, British journal of industrial medicine, 37 (1980) 337-362.

[54] H.C. Yeh, G.M. Schum, Models of human lung airways and their application to inhaled particle deposition, Bulletin of mathematical biology, 42 (1980) 461-480.

[55] K.P. O'Donnell, H.D.C. Smyth, Macro- and Microstructure of the Airways for Drug Delivery, in: H.D.C. Smyth, A.J. Hickey (Eds.) Controlled Pulmonary Drug Delivery, Springer New York, New York, NY, 2011, pp. 1-19.

[56] Q. Liu, J. Guan, L. Qin, X. Zhang, S. Mao, Physicochemical properties affecting the fate of nanoparticles in pulmonary drug delivery, Drug Discovery Today, 25 (2020) 150-159.

[57] E. Houtmeyers, R. Gosselink, G. Gayan-Ramirez, M. Decramer, Regulation of mucociliary clearance in health and disease, The European respiratory journal, 13 (1999) 1177-1188.

[58] F. Taherali, F. Varum, A.W. Basit, A slippery slope: On the origin, role and physiology of mucus, Adv Drug Deliv Rev, 124 (2018) 16-33.

[59] R.M. Kannan, E. Nance, S. Kannan, D.A. Tomalia, Emerging concepts in dendrimer-based nanomedicine: from design principles to clinical applications, Journal of internal medicine, 276 (2014) 579-617.

[60] B. Patel, N. Gupta, F. Ahsan, Particle engineering to enhance or lessen particle uptake by alveolar macrophages and to influence the therapeutic outcome, European journal of pharmaceutics and biopharmaceutics : official journal of Arbeitsgemeinschaft fur Pharmazeutische Verfahrenstechnik e.V, 89 (2015) 163-174.

[61] T. Thum, V.J. Erpenbeck, J. Moeller, J.M. Hohlfeld, N. Krug, J. Borlak, Expression of xenobiotic metabolizing enzymes in different lung compartments of smokers and nonsmokers, Environmental health perspectives, 114 (2006) 1655-1661.

[62] G.I. Somers, N. Lindsay, B.M. Lowdon, A.E. Jones, C. Freathy, S. Ho, A.J. Woodrooffe, M.K. Bayliss, G.R. Manchee, A comparison of the expression and metabolizing activities of phase I and II enzymes in freshly isolated human lung parenchymal cells and cryopreserved human hepatocytes, Drug metabolism and disposition: the biological fate of chemicals, 35 (2007) 1797-1805.

[63] R. Rosière, K. Amighi, N. Wauthoz, Chapter 10 - Nanomedicine-Based Inhalation Treatments for Lung Cancer, in: P. Kesharwani (Ed.) Nanotechnology-Based Targeted Drug Delivery Systems for Lung Cancer, Academic Press2019, pp. 249-268.

[64] F. Gagnadoux, J. Hureaux, L. Vecellio, T. Urban, A. Le Pape, I. Valo, J. Montharu, V. Leblond, M. Boisdron-Celle, S. Lerondel, C. Majoral, P. Diot, J.L. Racineux, E. Lemarie, Aerosolized chemotherapy, J Aerosol Med Pulm Drug Deliv, 21 (2008) 61-70.

[65] H.D. Smyth, I. Saleem, M. Donovan, C.F. Verschraegen, Pulmonary delivery of anti-cancer agents, Advanced drug formulation design to optimize therapeutic outcomes, 160 (2007) 81.

[66] B. Olsson, E. Bondesson, L. Borgström, S. Edsbäcker, S. Eirefelt, K. Ekelund, L. Gustavsson, T. Hegelund-Myrbäck, Pulmonary Drug Metabolism, Clearance, and Absorption, in: H.D.C.

Smyth, A.J. Hickey (Eds.) Controlled Pulmonary Drug Delivery, Springer New York, New York, NY, 2011, pp. 21-50.

[67] P. Zarogoulidis, E. Chatzaki, K. Porpodis, K. Domvri, W. Hohenforst-Schmidt, E.P. Goldberg, N. Karamanos, K. Zarogoulidis, Inhaled chemotherapy in lung cancer: future concept of nanomedicine, International journal of nanomedicine, 7 (2012) 1551-1572.

[68] P. Zarogoulidis, C. Giraleli, N.K. Karamanos, Inhaled chemotherapy in lung cancer: safety concerns of nanocomplexes delivered, Therapeutic delivery, 3 (2012) 1021-1023.

[69] P. Zarogoulidis, E. Eleftheriadou, I. Sapardanis, V. Zarogoulidou, H. Lithoxopoulou, T. Kontakiotis, N. Karamanos, G. Zachariadis, M. Mabroudi, A. Zisimopoulos, K. Zarogoulidis, Feasibility and effectiveness of inhaled carboplatin in NSCLC patients, Investigational new drugs, 30 (2012) 1628-1640.

[70] T. Luo, C. Loira-Pastoriza, H.P. Patil, B. Ucakar, G.G. Muccioli, C. Bosquillon, R. Vanbever, PEGylation of paclitaxel largely improves its safety and anti-tumor efficacy following pulmonary delivery in a mouse model of lung carcinoma, Journal of Controlled Release, 239 (2016) 62-71.

[71] C.A. Ruge, J. Kirch, C.-M. Lehr, Pulmonary drug delivery: from generating aerosols to overcoming biological barriers—therapeutic possibilities and technological challenges, The Lancet Respiratory Medicine, 1 (2013) 402-413.

[72] B.P.H. Wittgen, P.W.A. Kunst, K. van der Born, A.W. van Wijk, W. Perkins, F.G. Pilkiewicz, R. Perez-Soler, S. Nicholson, G.J. Peters, P.E. Postmus, Phase I Study of Aerosolized SLIT Cisplatin in the Treatment of Patients with Carcinoma of the Lung, Clinical Cancer Research, 13 (2007) 2414-2421.

[73] E. Lemarie, L. Vecellio, J. Hureaux, C. Prunier, C. Valat, D. Grimbert, M. Boidron-Celle, B. Giraudeau, A. le Pape, E. Pichon, P. Diot, A. el Houfia, F. Gagnadoux, Aerosolized gemcitabine in patients with carcinoma of the lung: feasibility and safety study, J Aerosol Med Pulm Drug Deliv, 24 (2011) 261-270.

[74] G.A. Otterson, M.A. Villalona-Calero, W. Hicks, X. Pan, J.A. Ellerton, S.N. Gettinger, J.R. Murren, Phase I/II study of inhaled doxorubicin combined with platinum-based therapy for advanced non-small cell lung cancer, Clinical cancer research : an official journal of the American Association for Cancer Research, 16 (2010) 2466-2473.

[75] H.M. Mansour, Y.S. Rhee, X. Wu, Nanomedicine in pulmonary delivery, International journal of nanomedicine, 4 (2009) 299-319.

[76] H.M. Abdelaziz, M. Gaber, M.M. Abd-Elwakil, M.T. Mabrouk, M.M. Elgohary, N.M. Kamel, D.M. Kabary, M.S. Freag, M.W. Samaha, S.M. Mortada, K.A. Elkhodairy, J.Y. Fang, A.O. Elzoghby, Inhalable particulate drug delivery systems for lung cancer therapy: Nanoparticles, microparticles, nanocomposites and nanoaggregates, Journal of controlled release : official journal of the Controlled Release Society, 269 (2018) 374-392.

[77] J.C. Sung, B.L. Pulliam, D.A. Edwards, Nanoparticles for drug delivery to the lungs, Trends in Biotechnology, 25 (2007) 563-570.

[78] M. Beck-Broichsitter, O.M. Merkel, T. Kissel, Controlled pulmonary drug and gene delivery using polymeric nano-carriers, Journal of Controlled Release, 161 (2012) 214-224.

[79] M. Ibrahim, R. Verma, L. Garcia-Contreras, Inhalation drug delivery devices: technology update, Medical devices (Auckland, N.Z.), 8 (2015) 131-139.

[80] R. Rosière, M. Van Woensel, V. Mathieu, I. Langer, T. Mathivet, M. Vermeersch, K. Amighi, N. Wauthoz, Development and evaluation of well-tolerated and tumor-penetrating polymeric micelle-based dry powders for inhaled anti-cancer chemotherapy, Int J Pharm, 501 (2016) 148-159.

[81] V. Levet, R. Rosière, R. Merlos, L. Fusaro, G. Berger, K. Amighi, N. Wauthoz, Development of controlled-release cisplatin dry powders for inhalation against lung cancers, International Journal of Pharmaceutics, 515 (2016) 209-220.

[82] S.A. Meenach, K.W. Anderson, J. Zach Hilt, R.C. McGarry, H.M. Mansour, Characterization and aerosol dispersion performance of advanced spray-dried chemotherapeutic PEGylated phospholipid particles for dry powder inhalation delivery in lung cancer, European Journal of Pharmaceutical Sciences, 49 (2013) 699-711.

[83] N. Wauthoz, P. Deleuze, A. Saumet, C. Duret, R. Kiss, K. Amighi, Temozolomide-Based Dry Powder Formulations for Lung Tumor-Related Inhalation Treatment, Pharmaceutical research, 28 (2011) 762-775.

[84] T. Peng, S. Lin, B. Niu, X. Wang, Y. Huang, X. Zhang, G. Li, X. Pan, C. Wu, Influence of physical properties of carrier on the performance of dry powder inhalers, Acta Pharmaceutica Sinica B, 6 (2016) 308-318.

[85] N. Alhajj, N.J. O'Reilly, H. Cathcart, Designing enhanced spray dried particles for inhalation: A review of the impact of excipients and processing parameters on particle properties, Powder Technology, 384 (2021) 313-331.

[86] S. Yeung, D. Traini, A. Tweedie, D. Lewis, T. Church, P.M. Young, Limitations of high dose carrier based formulations, International Journal of Pharmaceutics, 544 (2018) 141-152.

[87] I. Sibum, P. Hagedoorn, A.H. de Boer, H.W. Frijlink, F. Grasmeijer, Challenges for pulmonary delivery of high powder doses, International Journal of Pharmaceutics, 548 (2018) 325-336.

[88] P. Kulkarni, P.A. Baron, K. Willeke, Fundamentals of Single Particle Transport, Aerosol Measurement2011, pp. 15-30.

[89] M. Malamatari, A. Charisi, S. Malamataris, K. Kachrimanis, I. Nikolakakis, Spray Drying for the Preparation of Nanoparticle-Based Drug Formulations as Dry Powders for Inhalation, Processes, 8 (2020) 788.

[90] I.C. Kemp, R. Wadley, T. Hartwig, U. Cocchini, Y. See-Toh, L. Gorringe, K. Fordham, F. Ricard, Experimental Study of Spray Drying and Atomization with a Two-Fluid Nozzle to Produce Inhalable Particles, Drying Technology, 31 (2013) 930-941.

[91] D.A. Miller, D. Ellenberger, M. Gil, Spray-Drying Technology, in: R.O. Williams Iii, A.B. Watts, D.A. Miller (Eds.) Formulating Poorly Water-soluble Drugs, Springer International Publishing, Cham, 2016, pp. 437-525.

[92] A.H. Lefebvre, V.G. McDonell, Atomization and sprays, CRC press2017.

[93] N. Carrigy, R. Vehring, Engineering Stable Spray-Dried Biologic Powder for Inhalation, 2019, pp. 291-326.

[94] A. Osman, L. Goehring, A. Patti, H. Stitt, N. Shokri, Fundamental Investigation of the Drying of Solid Suspensions, Industrial & Engineering Chemistry Research, 56 (2017) 10506-10513.

[95] W.E. Ranz, Wall Flows in a Cyclone Separator: A Description of Internal Phenomena, Aerosol Science and Technology, 4 (1985) 417-432.

[96] R. Vehring, W.R. Foss, D. Lechuga-Ballesteros, Particle formation in spray drying, Journal of Aerosol Science, 38 (2007) 728-746.

[97] N. Anton, A. Jakhmola, T.F. Vandamme, Trojan Microparticles for Drug Delivery, Pharmaceutics, 4 (2012) 1-25.

[98] N. Tsapis, D. Bennett, B. Jackson, D.A. Weitz, D.A. Edwards, Trojan particles: large porous carriers of nanoparticles for drug delivery, Proceedings of the National Academy of Sciences of the United States of America, 99 (2002) 12001-12005.

[99] N. Alhajj, N.J. O'Reilly, H. Cathcart, Nano-in-Microparticles for Pulmonary Drug Delivery, in: P.P. Mehta, V. Dhapte -Pawar (Eds.) Pulmonary Drug Delivery Systems: Material and Technological Advances, Springer Nature Singapore, Singapore, 2023, pp. 91-129.

[100] R. Vehring, Pharmaceutical Particle Engineering via Spray Drying, Pharmaceutical research, 25 (2008) 999-1022.

[101] A. Polson, The Some Aspects of Diffusion in Solution and a Definition of a Colloidal Particle, The Journal of Physical and Colloid Chemistry, 54 (1950) 649-652.

[102] N. Alhajj, N.J. O'Reilly, H. Cathcart, Leucine as an excipient in spray dried powder for inhalation, Drug Discovery Today, 26 (2021) 2384-2396.

[103] Y. Roos, H., Importance of glass transition and water activity to spray drying and stability of dairy powders, Lait, 82 (2002) 475-484.

[104] T. Sou, L.M. Kaminskas, T.-H. Nguyen, R. Carlberg, M.P. McIntosh, D.A.V. Morton, The effect of amino acid excipients on morphology and solid-state properties of multi-component spray-dried formulations for pulmonary delivery of biomacromolecules, European Journal of Pharmaceutics and Biopharmaceutics, 83 (2013) 234-243.

[105] E.K. Efthimiadou, A.-F. Metaxa, G. Kordas, Modified PolysaccharidesPolysaccharidesas Drug Delivery, in: K.G. Ramawat, J.-M. Mérillon (Eds.) Polysaccharides: Bioactivity and Biotechnology, Springer International Publishing, Cham, 2021, pp. 1-26.

[106] Z. Shariatinia, Chapter 2 - Pharmaceutical applications of natural polysaccharides, in: M.S. Hasnain, A.K. Nayak (Eds.) Natural Polysaccharides in Drug Delivery and Biomedical Applications, Academic Press2019, pp. 15-57.

[107] M. Gericke, P. Schulze, T. Heinze, Nanoparticles Based on Hydrophobic Polysaccharide Derivatives—Formation Principles, Characterization Techniques, and Biomedical Applications, Macromolecular Bioscience, 20 (2020) 1900415.

[108] O. Germershaus, T. Lühmann, J.C. Rybak, J. Ritzer, L. Meinel, Application of natural and semi-synthetic polymers for the delivery of sensitive drugs, International Materials Reviews, 60 (2015) 101-131.

[109] J. Yang, S. Han, H. Zheng, H. Dong, J. Liu, Preparation and application of micro/nanoparticles based on natural polysaccharides, Carbohydrate Polymers, 123 (2015) 53-66.

[110] F. Avaltroni, P.E. Bouquerand, V. Normand, Maltodextrin molecular weight distribution influence on the glass transition temperature and viscosity in aqueous solutions, Carbohydrate Polymers, 58 (2004) 323-334.

[111] S. Barthold, M. Hittinger, D. Primavessy, A. Zapp, H. Groß, M. Schneider, Preparation of maltodextrin nanoparticles and encapsulation of bovine serum albumin – Influence of formulation parameters, European Journal of Pharmaceutics and Biopharmaceutics, 142 (2019) 405-410.

[112] Y. Jallouli, A. Paillard, J. Chang, E. Sevin, D. Betbeder, Influence of surface charge and inner composition of porous nanoparticles to cross blood–brain barrier in vitro, International Journal of Pharmaceutics, 344 (2007) 103-109.

[113] M.Q. Le, R. Carpentier, I. Lantier, C. Ducournau, I. Dimier-Poisson, D. Betbeder, Residence time and uptake of porous and cationic maltodextrin-based nanoparticles in the nasal mucosa: Comparison with anionic and cationic nanoparticles, International Journal of Pharmaceutics, 550 (2018) 316-324.

[114] M.Q. Lê, R. Carpentier, I. Lantier, C. Ducournau, F. Fasquelle, I. Dimier-Poisson, D. Betbeder, Protein delivery by porous cationic maltodextrin-based nanoparticles into nasal

mucosal cells: Comparison with cationic or anionic nanoparticles, International Journal of Pharmaceutics: X, 1 (2019) 100001.

[115] E. Jung, J. Lee, L. Jeong, S. Park, M. Lee, C. Song, D. Lee, Stimulus-activatable echogenic maltodextrin nanoparticles as nanotheranostic agents for peripheral arterial disease, Biomaterials, 192 (2019) 282-291.

[116] E. Jung, C. Kang, J. Lee, D. Yoo, D.W. Hwang, D. Kim, S.-C. Park, S.K. Lim, C. Song, D. Lee, Molecularly Engineered Theranostic Nanoparticles for Thrombosed Vessels: H2O2-Activatable Contrast-Enhanced Photoacoustic Imaging and Antithrombotic Therapy, ACS Nano, 12 (2018) 392-401.

[117] R. Carpentier, A. Platel, N. Salah, F. Nesslany, D. Betbeder, Porous Maltodextrin-Based Nanoparticles: A Safe Delivery System for Nasal Vaccines, Journal of Nanomaterials, 2018 (2018) 9067195.

[118] F. Erra Díaz, E. Dantas, J. Geffner, Unravelling the Interplay between Extracellular Acidosis and Immune Cells, Mediators of Inflammation, 2018 (2018) 1218297.

[119] J.-Z. Du, X.-J. Du, C.-Q. Mao, J. Wang, Tailor-Made Dual pH-Sensitive Polymer–Doxorubicin Nanoparticles for Efficient Anticancer Drug Delivery, Journal of the American Chemical Society, 133 (2011) 17560-17563.

[120] E.R. Gillies, A.P. Goodwin, J.M.J. Fréchet, Acetals as pH-Sensitive Linkages for Drug Delivery, Bioconjugate Chemistry, 15 (2004) 1254-1263.

[121] E.M. Bachelder, T.T. Beaudette, K.E. Broaders, J. Dashe, J.M.J. Fréchet, Acetal-Derivatized Dextran: An Acid-Responsive Biodegradable Material for Therapeutic Applications, Journal of the American Chemical Society, 130 (2008) 10494-10495.

[122] L.R. Volpatti, M.A. Matranga, A.B. Cortinas, D. Delcassian, K.B. Daniel, R. Langer, D.G. Anderson, Glucose-Responsive Nanoparticles for Rapid and Extended Self-Regulated Insulin Delivery, ACS Nano, 14 (2020) 488-497.

[123] S. Wang, F. Fontana, M.-A. Shahbazi, H.A. Santos, Acetalated dextran based nano- and microparticles: synthesis, fabrication, and therapeutic applications, Chemical Communications, 57 (2021) 4212-4229.

[124] E.M. Bachelder, E.N. Pino, K.M. Ainslie, Acetalated Dextran: A Tunable and Acid-Labile Biopolymer with Facile Synthesis and a Range of Applications, Chemical Reviews, 117 (2017) 1915-1926.

[125] J.A. Cohen, T.T. Beaudette, J.L. Cohen, K.E. Broaders, E.M. Bachelder, J.M.J. Fréchet, Acetal-Modified Dextran Microparticles with Controlled Degradation Kinetics and Surface Functionality for Gene Delivery in Phagocytic and Non-Phagocytic Cells, Advanced Materials, 22 (2010) 3593-3597.

[126] P.R. Wich, J.M.J. Fréchet, Degradable Dextran Particles for Gene Delivery Applications, Australian Journal of Chemistry, 65 (2012) 15-19.

[127] E.M. Bachelder, T.T. Beaudette, K.E. Broaders, J.M.J. Fréchet, M.T. Albrecht, A.J. Mateczun, K.M. Ainslie, J.T. Pesce, A.M. Keane-Myers, In vitro analysis of acetalated dextran microparticles as a potent delivery platform for vaccine adjuvants, Molecular pharmaceutics, 7 (2010) 826-835.

[128] N. Chen, M.D. Gallovic, P. Tiet, J.P.Y. Ting, K.M. Ainslie, E.M. Bachelder, Investigation of tunable acetalated dextran microparticle platform to optimize M2e-based influenza vaccine efficacy, Journal of Controlled Release, 289 (2018) 114-124.

[129] S. Lee, A. Stubelius, N. Hamelmann, V. Tran, A. Almutairi, Inflammation-Responsive Drug-Conjugated Dextran Nanoparticles Enhance Anti-Inflammatory Drug Efficacy, ACS Appl Mater Interfaces, 10 (2018) 40378-40387.

[130] A. Stubelius, W. Sheng, S. Lee, J. Olejniczak, M. Guma, A. Almutairi, Disease-Triggered Drug Release Effectively Prevents Acute Inflammatory Flare-Ups, Achieving Reduced Dosing, Small, 14 (2018) e1800703.

[131] S. Suarez, G.N. Grover, R.L. Braden, K.L. Christman, A. Almutairi, Tunable Protein Release from Acetalated Dextran Microparticles: A Platform for Delivery of Protein Therapeutics to the Heart Post-MI, Biomacromolecules, 14 (2013) 3927-3935.

[132] C. Ornelas-Megiatto, P.N. Shah, P.R. Wich, J.L. Cohen, J.A. Tagaev, J.A. Smolen, B.D. Wright, M.J. Panzner, W.J. Youngs, J.M.J. Fréchet, C.L. Cannon, Aerosolized Antimicrobial Agents Based on Degradable Dextran Nanoparticles Loaded with Silver Carbene Complexes, Molecular Pharmaceutics, 9 (2012) 3012-3022.

[133] B. Shkodra-Pula, C. Kretzer, P.M. Jordan, P. Klemm, A. Koeberle, D. Pretzel, E. Banoglu, S. Lorkowski, M. Wallert, S. Höppener, S. Stumpf, A. Vollrath, S. Schubert, O. Werz, U.S. Schubert, Encapsulation of the dual FLAP/mPEGS-1 inhibitor BRP-187 into acetalated dextran and PLGA nanoparticles improves its cellular bioactivity, Journal of Nanobiotechnology, 18 (2020) 73.

[134] Z. Liu, Y. Li, W. Li, C. Xiao, D. Liu, C. Dong, M. Zhang, E. Mäkilä, M. Kemell, J. Salonen, J.T. Hirvonen, H. Zhang, D. Zhou, X. Deng, H.A. Santos, Multifunctional Nanohybrid Based on Porous Silicon Nanoparticles, Gold Nanoparticles, and Acetalated Dextran for Liver Regeneration and Acute Liver Failure Theranostics, Advanced Materials, 30 (2018) 1703393.

[135] J.V. Gregory, D.R. Vogus, A. Barajas, M.A. Cadena, S. Mitragotri, J. Lahann, Programmable Delivery of Synergistic Cancer Drug Combinations Using Bicompartmental Nanoparticles, Advanced Healthcare Materials, 9 (2020) 2000564.

[136] Z. Wang, S.K. Gupta, S.A. Meenach, Development and physicochemical characterization of acetalated dextran aerosol particle systems for deep lung delivery, International Journal of Pharmaceutics, 525 (2017) 264-274.

[137] K.E. Broaders, J.A. Cohen, T.T. Beaudette, E.M. Bachelder, J.M.J. Fréchet, Acetalated dextran is a chemically and biologically tunable material for particulate immunotherapy, Proceedings of the National Academy of Sciences, 106 (2009) 5497.

[138] S. Bakkialakshmi, P. Selvarani, S. Chenthamarai, Fluorescence quenching of Rhodamine B base by two amines, Spectrochimica Acta Part A: Molecular and Biomolecular Spectroscopy, 105 (2013) 557-562.

[139] I. Siemons, R.G.A. Politiek, R.M. Boom, R.G.M. van der Sman, M.A.I. Schutyser, Dextrose equivalence of maltodextrins determines particle morphology development during single sessile droplet drying, Food Research International, 131 (2020) 108988.

[140] N. Castro, V. Durrieu, C. Raynaud, A. Rouilly, Influence of DE-value on the physicochemical properties of maltodextrin for melt extrusion processes, Carbohydrate Polymers, 144 (2016) 464-473.

[141] Z. Saavedra-Leos, C. Leyva-Porras, S.B. Araujo-Díaz, A. Toxqui-Terán, A.J. Borrás-Enríquez, Technological Application of Maltodextrins According to the Degree of Polymerization, Molecules (Basel, Switzerland), 20 (2015) 21067-21081.

[142] T. Li, H. Li, H. Wang, W. Lu, M. Osa, Y. Wang, J. Mays, K. Hong, Chain flexibility and glass transition temperatures of poly(n-alkyl (meth)acrylate)s: Implications of tacticity and chain dynamics, Polymer, 213 (2021) 123207.

[143] R.-M. Wang, S.-R. Zheng, Y.-P. Zheng, 3 - Matrix materials, in: R.-M. Wang, S.-R. Zheng, Y.-P. Zheng (Eds.) Polymer Matrix Composites and Technology, Woodhead Publishing2011, pp. 101-548.

[144] R.G.M. van der Sman, Predictions of Glass Transition Temperature for Hydrogen Bonding Biomaterials, The Journal of Physical Chemistry B, 117 (2013) 16303-16313.

[145] M. Norouzi, P. Hardy, Clinical applications of nanomedicines in lung cancer treatment, Acta Biomaterialia, 121 (2021) 134-142.

[146] E. Bernabeu, M. Cagel, E. Lagomarsino, M. Moretton, D.A. Chiappetta, Paclitaxel: What has been done and the challenges remain ahead, International Journal of Pharmaceutics, 526 (2017) 474-495.

[147] N. Bertrand, J. Wu, X. Xu, N. Kamaly, O.C. Farokhzad, Cancer nanotechnology: the impact of passive and active targeting in the era of modern cancer biology, Adv Drug Deliv Rev, 66 (2014) 2-25.

[148] K. Tzogani, K. Penttilä, T. Lapveteläinen, R. Hemmings, J. Koenig, J. Freire, S. Márcia, S. Cole, P. Coppola, B. Flores, Y. Barbachano, S.D. Roige, F. Pignatti, EMA Review of Daunorubicin and Cytarabine Encapsulated in Liposomes (Vyxeos, CPX-351) for the Treatment of Adults with Newly Diagnosed, Therapy-Related Acute Myeloid Leukemia or Acute Myeloid Leukemia with Myelodysplasia-Related Changes, The oncologist, 25 (2020) e1414-e1420.

[149] J.A. Kemp, M.S. Shim, C.Y. Heo, Y.J. Kwon, "Combo" nanomedicine: Co-delivery of multi-modal therapeutics for efficient, targeted, and safe cancer therapy, Advanced Drug Delivery Reviews, 98 (2016) 3-18.

[150] Y. Yuan, T. Cai, X. Xia, R. Zhang, P. Chiba, Y. Cai, Nanoparticle delivery of anticancer drugs overcomes multidrug resistance in breast cancer, Drug delivery, 23 (2016) 3350-3357.

[151] B.V.N. Nagavarma, H. Yadav, A. Ayaz, L. Vasudha, H. Shivakumar, Different techniques for preparation of polymeric nanoparticles- A review, Asian Journal of Pharmaceutical and Clinical Research, 5 (2012) 16-23.

[152] C.I.C. Crucho, M.T. Barros, Polymeric nanoparticles: A study on the preparation variables and characterization methods, Materials Science and Engineering: C, 80 (2017) 771-784.

[153] A. Zielińska, F. Carreiró, A.M. Oliveira, A. Neves, B. Pires, D.N. Venkatesh, A. Durazzo, M. Lucarini, P. Eder, A.M. Silva, A. Santini, E.B. Souto, Polymeric Nanoparticles: Production, Characterization, Toxicology and Ecotoxicology, Molecules (Basel, Switzerland), 25 (2020) 3731.

[154] I.J. Joye, D.J. McClements, Production of nanoparticles by anti-solvent precipitation for use in food systems, Trends in Food Science & Technology, 34 (2013) 109-123.

[155] Y. Liu, G. Yang, D. Zou, Y. Hui, K. Nigam, A.P.J. Middelberg, C.-X. Zhao, Formulation of Nanoparticles Using Mixing-Induced Nanoprecipitation for Drug Delivery, Industrial & Engineering Chemistry Research, 59 (2020) 4134-4149.

[156] S. Galindo-Rodriguez, E. Allémann, H. Fessi, E. Doelker, Physicochemical Parameters Associated with Nanoparticle Formation in the Salting-Out, Emulsification-Diffusion, and Nanoprecipitation Methods, Pharmaceutical research, 21 (2004) 1428-1439.

[157] S. Ding, N. Anton, T.F. Vandamme, C.A. Serra, Microfluidic nanoprecipitation systems for preparing pure drug or polymeric drug loaded nanoparticles: an overview, Expert Opin Drug Deliv, 13 (2016) 1447-1460.

[158] W.S. Saad, R.K. Prud'homme, Principles of nanoparticle formation by flash nanoprecipitation, Nano Today, 11 (2016) 212-227.

[159] N. Günday Türeli, A.E. Türeli, M. Schneider, Optimization of ciprofloxacin complex loaded PLGA nanoparticles for pulmonary treatment of cystic fibrosis infections: Design of experiments approach, International Journal of Pharmaceutics, 515 (2016) 343-351.

[160] R. Rietscher, C. Thum, C.M. Lehr, M. Schneider, Semi-automated nanoprecipitation-system--an option for operator independent, scalable and size adjustable nanoparticle synthesis, Pharmaceutical research, 32 (2015) 1859-1863.

[161] N. Günday Türeli, A.E. Türeli, M. Schneider, Counter-ion complexes for enhanced drug loading in nanocarriers: Proof-of-concept and beyond, International Journal of Pharmaceutics, 511 (2016) 994-1001.

[162] H. Fessi, F. Puisieux, J.P. Devissaguet, N. Ammoury, S. Benita, Nanocapsule formation by interfacial polymer deposition following solvent displacement, International Journal of Pharmaceutics, 55 (1989) R1-R4.

[163] K. Robinson, C. Mock, D. Liang, Pre-formulation studies of resveratrol, Drug Dev Ind Pharm, 41 (2015) 1464-1469.

[164] M.E. Lund, J. To, B.A. O'Brien, S. Donnelly, The choice of phorbol 12-myristate 13-acetate differentiation protocol influences the response of THP-1 macrophages to a pro-inflammatory stimulus, Journal of Immunological Methods, 430 (2016) 64-70.

[165] M. Mehanny, M. Koch, C.-M. Lehr, G. Fuhrmann, Streptococcal Extracellular Membrane Vesicles Are Rapidly Internalized by Immune Cells and Alter Their Cytokine Release, Frontiers in Immunology, 11 (2020).

[166] M. Kakran, N.G. Sahoo, I.L. Tan, L. Li, Preparation of nanoparticles of poorly water-soluble antioxidant curcumin by antisolvent precipitation methods, Journal of Nanoparticle Research, 14 (2012) 757.

[167] S. Kalepu, V. Nekkanti, Insoluble drug delivery strategies: review of recent advances and business prospects, Acta Pharmaceutica Sinica B, 5 (2015) 442-453.

[168] N. Chen, M.A. Collier, M.D. Gallovic, G.C. Collins, C.C. Sanchez, E.Q. Fernandes, E.M. Bachelder, K.M. Ainslie, Degradation of acetalated dextran can be broadly tuned based on cyclic acetal coverage and molecular weight, International Journal of Pharmaceutics, 512 (2016) 147-157.

[169] K.J. Kauffman, C. Do, S. Sharma, M.D. Gallovic, E.M. Bachelder, K.M. Ainslie, Synthesis and Characterization of Acetalated Dextran Polymer and Microparticles with Ethanol as a Degradation Product, ACS Applied Materials & Interfaces, 4 (2012) 4149-4155.

[170] S. Behzadi, V. Serpooshan, W. Tao, M.A. Hamaly, M.Y. Alkawareek, E.C. Dreaden, D. Brown, A.M. Alkilany, O.C. Farokhzad, M. Mahmoudi, Cellular uptake of nanoparticles: journey inside the cell, Chemical Society reviews, 46 (2017) 4218-4244.

[171] W. Yang, J.I. Peters, R.O. Williams, Inhaled nanoparticles—A current review, International Journal of Pharmaceutics, 356 (2008) 239-247.

[172] A. Torge, P. Grützmacher, F. Mücklich, M. Schneider, The influence of mannitol on morphology and disintegration of spray-dried nano-embedded microparticles, European Journal of Pharmaceutical Sciences, 104 (2017) 171-179.

[173] H.I. Shahin, L. Chablani, A comprehensive overview of dry powder inhalers for pulmonary drug delivery: Challenges, advances, optimization techniques, and applications, Journal of Drug Delivery Science and Technology, 84 (2023) 104553.

[174] A. Dolor, F.C. Szoka, Jr., Digesting a Path Forward: The Utility of Collagenase Tumor Treatment for Improved Drug Delivery, Molecular Pharmaceutics, 15 (2018) 2069-2083.

[175] Z. Zhao, A. Ukidve, J. Kim, S. Mitragotri, Targeting Strategies for Tissue-Specific Drug Delivery, Cell, 181 (2020) 151-167.

[176] M. Marques, R. Löbenberg, M. Almukainzi, Simulated Biological Fluids with Possible Application in Dissolution Testing, Dissolution Technologies, 18 (2011) 15-28.

[177] N. Lababidi, E. Ofosu Kissi, W.A.M. Elgaher, V. Sigal, J. Haupenthal, B.C. Schwarz, A.K.H. Hirsch, T. Rades, M. Schneider, Spray-drying of inhalable, multifunctional formulations for the treatment of biofilms formed in cystic fibrosis, Journal of Controlled Release, 314 (2019) 62-71.

[178] A. Torge, G. Pavone, M. Jurisic, K. Lima-Engelmann, M. Schneider, A comparison of spherical and cylindrical microparticles composed of nanoparticles for pulmonary application, Aerosol Science and Technology, 53 (2019) 53-62.

[179] N.A. Stocke, S.A. Meenach, S.M. Arnold, H.M. Mansour, J.Z. Hilt, Formulation and characterization of inhalable magnetic nanocomposite microparticles (MnMs) for targeted pulmonary delivery via spray drying, International Journal of Pharmaceutics, 479 (2015) 320-328.

[180] T. Hibbard, H. Mitchell, Y. Kim, K. Shankland, H. Al-Obaidi, Spray dried progesterone formulations for carrier free dry powder inhalation, European Journal of Pharmaceutics and Biopharmaceutics, 189 (2023) 264-275.

[181] C.A. Lima, P.M.B. Rodrigues, T.S. Porto, D.A. Viana, J.L. Lima Filho, A.L.F. Porto, M.G. Carneiro da Cunha, Production of a collagenase from Candida albicans URM3622, Biochemical Engineering Journal, 43 (2009) 315-320.

[182] D.A. Fernandes, E. Costa, P. Leandro, M.L. Corvo, Formulation of spray dried enzymes for dry powder inhalers: An integrated methodology, Int J Pharm, 615 (2022) 121492.

[183] R.Y.K. Chang, M.Y.T. Chow, D. Khanal, D. Chen, H.-K. Chan, Dry powder pharmaceutical biologics for inhalation therapy, Advanced Drug Delivery Reviews, 172 (2021) 64-79.

[184] D.A. Fernandes, P. Leandro, E. Costa, M.L. Corvo, Dry powder inhaler formulation of Cu,Zn-superoxide dismutase by spray drying: A proof-of-concept, Powder Technology, 389 (2021) 131-137.

[185] N. Alhajj, N.J. O'Reilly, H. Cathcart, Quality by design – Spray drying of ciprofloxacin-quercetin fixed-dose combination intended for inhalation, International Journal of Pharmaceutics, 642 (2023) 123151.

[186] S. Focaroli, P.T. Mah, J.E. Hastedt, I. Gitlin, S. Oscarson, J.V. Fahy, A.M. Healy, A Design of Experiment (DoE) approach to optimise spray drying process conditions for the production of trehalose/leucine formulations with application in pulmonary delivery, International Journal of Pharmaceutics, 562 (2019) 228-240.

[187] U.V. Shah, V. Karde, C. Ghoroi, J.Y.Y. Heng, Influence of particle properties on powder bulk behaviour and processability, International Journal of Pharmaceutics, 518 (2017) 138-154.

[188] R. Vehring, Pharmaceutical particle engineering via spray drying, Pharmaceutical research, 25 (2008) 999-1022.

[189] M.A.M. Momin, I.G. Tucker, C.S. Doyle, J.A. Denman, S. Sinha, S.C. Das, Co-spray drying of hygroscopic kanamycin with the hydrophobic drug rifampicin to improve the aerosolization of kanamycin powder for treating respiratory infections, International Journal of Pharmaceutics, 541 (2018) 26-36.

[190] Y.-X. Chang, J.-J. Yang, R.-L. Pan, Q. Chang, Y.-H. Liao, Anti-hygroscopic effect of leucine on spray-dried herbal extract powders, Powder Technology, 266 (2014) 388-395.

[191] L. Li, S. Sun, T. Parumasivam, J.A. Denman, T. Gengenbach, P. Tang, S. Mao, H.-K. Chan, l-Leucine as an excipient against moisture on in vitro aerosolization performances of highly hygroscopic spray-dried powders, European Journal of Pharmaceutics and Biopharmaceutics, 102 (2016) 132-141.

[192] P. Zanen, L.T. Go, J.W. Lammers, The efficacy of a low-dose, monodisperse parasympathicolytic aerosol compared with a standard aerosol from a metered-dose inhaler, European journal of clinical pharmacology, 54 (1998) 27-30.

[193] S.A. Langhans, Three-Dimensional in Vitro Cell Culture Models in Drug Discovery and Drug Repositioning, Frontiers in Pharmacology, 9 (2018).

[194] K. Stock, M.F. Estrada, S. Vidic, K. Gjerde, A. Rudisch, V.E. Santo, M. Barbier, S. Blom, S.C. Arundkar, I. Selvam, A. Osswald, Y. Stein, S. Gruenewald, C. Brito, W. van Weerden, V. Rotter, E. Boghaert, M. Oren, W. Sommergruber, Y. Chong, R. de Hoogt, R. Graeser, Capturing tumor complexity in vitro: Comparative analysis of 2D and 3D tumor models for drug discovery, Scientific Reports, 6 (2016) 28951.

[195] I. Van Zundert, B. Fortuni, S. Rocha, From 2D to 3D Cancer Cell Models-The Enigmas of Drug Delivery Research, Nanomaterials (Basel, Switzerland), 10 (2020).

[196] H. Shen, S. Cai, C. Wu, W. Yang, H. Yu, L. Liu, Recent Advances in Three-Dimensional Multicellular Spheroid Culture and Future Development, Micromachines, 12 (2021).

[197] J.M. Rozenberg, G.I. Filkov, A.V. Trofimenko, E.A. Karpulevich, V.D. Parshin, V.V. Royuk, M.I. Sekacheva, M.O. Durymanov, Biomedical Applications of Non-Small Cell Lung Cancer Spheroids, Frontiers in Oncology, 11 (2021).

[198] X. He, Y. Yang, L. Li, P. Zhang, H. Guo, N. Liu, X. Yang, F. Xu, Engineering extracellular matrix to improve drug delivery for cancer therapy, Drug Discovery Today, 25 (2020) 1727-1734.

[199] T. Liu, L. Zhou, D. Li, T. Andl, Y. Zhang, Cancer-Associated Fibroblasts Build and Secure the Tumor Microenvironment, Frontiers in cell and developmental biology, 7 (2019) 60.

[200] R.M. Almuqbil, R.S. Heyder, E.R. Bielski, M. Durymanov, J.J. Reineke, S.R.P. da Rocha, Dendrimer Conjugation Enhances Tumor Penetration and Efficacy of Doxorubicin in Extracellular Matrix-Expressing 3D Lung Cancer Models, Molecular Pharmaceutics, 17 (2020) 1648-1662.

[201] X. Yong, P. Wang, T. Jiang, W. Yu, Y. Shang, Y. Han, P. Zhang, Q. Li, Fibroblasts weaken the anti-tumor effect of gefitinib on co-cultured non-small cell lung cancer cells, Chinese medical journal, 127 (2014) 2091-2096.

[202] I. Yakavets, A. Francois, A. Benoit, J.-L. Merlin, L. Bezdetnaya, G. Vogin, Advanced co-culture 3D breast cancer model for investigation of fibrosis induced by external stimuli: optimization study, Scientific Reports, 10 (2020) 21273.

[203] S.J. Han, S. Kwon, K.S. Kim, Challenges of applying multicellular tumor spheroids in preclinical phase, Cancer Cell International, 21 (2021) 152.

[204] J. López-García, M. Lehocký, P. Humpolíček, P. Sáha, HaCaT Keratinocytes Response on Antimicrobial Atelocollagen Substrates: Extent of Cytotoxicity, Cell Viability and Proliferation, Journal of Functional Biomaterials, 5 (2014) 43-57.

[205] S.M. Abdel-Hafez, J. Zapp, M. Gallei, M. Schneider, Formulation attributes, acid tunable degradability and cellular interaction of acetalated maltodextrin nanoparticles, Carbohydrate Polymers, 288 (2022) 119378.

[206] M. Kato, Y. Hattori, M. Kubo, Y. Maitani, Collagenase-1 injection improved tumor distribution and gene expression of cationic lipoplex, International Journal of Pharmaceutics, 423 (2012) 428-434.

[207] L. Eikenes, S. Bruland Ø, C. Brekken, L. Davies Cde, Collagenase increases the transcapillary pressure gradient and improves the uptake and distribution of monoclonal antibodies in human osteosarcoma xenografts, Cancer research, 64 (2004) 4768-4773.

[208] R.Z. Lin, H.Y. Chang, Recent advances in three-dimensional multicellular spheroid culture for biomedical research, Biotechnology journal, 3 (2008) 1172-1184.

[209] B.M. Leung, S.C. Lesher-Perez, T. Matsuoka, C. Moraes, S. Takayama, Media additives to promote spheroid circularity and compactness in hanging drop platform, Biomaterials Science, 3 (2015) 336-344.

[210] N.A. Slawny, M. Labant, Physiologically relevant spheroid models for three-dimensional cell culture, Technology Platforms for 3D Cell Culture2017, pp. 50-73.

[211] N. Hari, P. Patel, J. Ross, K. Hicks, F. Vanholsbeeck, Optical coherence tomography complements confocal microscopy for investigation of multicellular tumour spheroids, Scientific Reports, 9 (2019) 10601.

Scientific output

Research articles

S.M. Abdel-Hafez, J. Zapp, M. Gallei, M. Schneider, Formulation attributes, acid tunable degradability and cellular interaction of acetalated maltodextrin nanoparticles, Carbohydrate Polymers, 288 (2022) 119378.

S.M. Abdel-Hafez, M. Gallei, M. Schneider, Inhalable nano-structured microparticles for extracellular matrix modulation as a potential delivery system for lung cancer, in due submission.

Conference contributions

S.M. Abdel-Hafez and M. Schneider, Acetalated maltodextrin pH-responsive nanoparticles: Formulation, characterization and cellular interaction studies, poster presentation. Annual Meeting of the German Pharmaceutical Society (DPhG), virtual conference, October 2021.

S.M. Abdel-Hafez and M. Schneider, Polysaccharide-based nano-structured microparticles for inhalation for lung cancer therapy, oral presentation. Annual Meeting of the German Pharmaceutical Society (DPhG), Marburg, Germany, September 2022.

S.M. Abdel-Hafez and M. Schneider, Extracellular matrix-modulating nano-structured microparticles for pulmonary inhalation as potential delivery system for lung cancer, oral presentation. The International Society for Aerosols in Medicine (ISAM) Congress, Saarbrücken, Germany, August 2023.

Curriculum vitae

Salma Mahmoud AbdelHafez AbdelFattah

Personal and contact information

Date of birth: 11th March 1988

Nationality: Egyptian

E-mail address: salma.abdelhafez@uni-saarland.de, salma.abdelhafez@pharma.asu.edu.eg, salma.abdelhafez@pharm.asu.edu.eg

Google scholar profile: Salma M. Abdel-Hafez

Research gate profile: Salma M. Abdel-Hafez

Education and training

Apr 2019 – present: Doctoral thesis

Department of Biopharmaceutics and Pharmaceutical Technology, Saarland University, Saarbrücken, Germany.

- Thesis title: Inhalable nano-structured microparticles for lung cancer treatment.

- Thesis supervisor: Prof. Dr. Marc Schneider.

Jul 2015 – Aug 2015: Nanosystems Initiative Munich (NIM) Research Internship

Department of Chemistry, Ludwig-Maximilian University, Munich, Germany.

- Project title: Functionalization of large-pore mesoporous silica nanoparticles for protein delivery.

- Group of Prof. Dr. Thomas Bein.

Nov 2012 – Dec 2017: Masters of Pharmaceutical Sciences (Drug Technology)

Department of Pharmaceutics and Industrial Pharmacy, Faculty of Pharmacy, Ain Shams University, Cairo, Egypt.

- Thesis title: Colloidal carriers for transdermal delivery.

- Supervisors: Prof. Dr. Omaima Sammour and Prof. Dr. Rania Hathout.

Sep 2005 – May 2010: Bachelor of Pharmaceutical Sciences

Faculty of Pharmacy, Ain Shams University, Cairo, Egypt.

- Cumulative grade: Excellent with honors (Premium rank).

Academic work experience

Apr 2019 – present: PhD Student

Department of Biopharmaceutics and Pharmaceutical Technology, Saarland University, Saarbrücken, Germany.

Apr 2018 – Mar 2019: Assistant lecturer

Department of Pharmaceutics and Industrial Pharmacy, Faculty of Pharmacy, Ain Shams University, Cairo, Egypt.

Jun 2011 – Mar 2018: Teaching assistant

Department of Pharmaceutics and Industrial Pharmacy, Faculty of Pharmacy, Ain Shams University, Cairo, Egypt.

Language skills

Mother tongue: Arabic

Foreign languages: English (IELTS overall band score: 7), German (Goethe Zertifikat B1: Note 2), and French (Basic user)

Grants

May 2018: German Egyptian Research Long-term Scholarship (GERLS)

- Full PhD scholarship, co-funded by the German Academic Exchange Service (DAAD) and the Egyptian Ministry of Higher Education.

Publications

D. Schmitt, **S.M. Abdel-Hafez**, M. Tummeley, V. Schünemann, M. Schneider, V. Presser, M. Gallei, Surface-Initiated Living Anionic Polymerization of Functional Methacrylates from the Surface of Organic Particles, Macromolecules, 56 (2023) 7086-7101.

J. Buescher, T. John, A.K. Boehm, L. Weber, **S.M. Abdel-Hafez**, C. Wagner, T. Kraus, M. Gallei, M. Schneider, A precise nanoparticle quantification approach using microfluidics and single-particle tracking, Journal of Drug Delivery Science and Technology, 75 (2022) 103579.

S.M. Abdel-Hafez, J. Zapp, M. Gallei, M. Schneider, Formulation attributes, acid tunable degradability and cellular interaction of acetalated maltodextrin nanoparticles, Carbohydrate Polymers, 288 (2022) 119378.

S.M. Abdel-Hafez, R.M. Hathout, O.A. Sammour, Attempts to enhance the anti-cancer activity of curcumin as a magical oncological agent using transdermal delivery, Advances in Traditional Medicine, 21 (2021) 15-29.

R.M. Hathout, H.A. Gad, **S.M. Abdel-Hafez**, N. Nasser, N. Khalil, T. Ateyya, A. Amr, N. Yasser, S. Nasr, A.A. Metwally, Gelatinized core liposomes: A new Trojan horse for the development of a novel timolol maleate glaucoma medication, International Journal of Pharmaceutics, 556 (2019) 192-199.

S.M. Abdel-Hafez, R.M. Hathout, O.A. Sammour, Tracking the transdermal penetration pathways of optimized curcumin-loaded chitosan nanoparticles via confocal laser scanning microscopy, International Journal of Biological Macromolecules, 108 (2018) 753-764.

S.M. Abdel-Hafez, R.M. Hathout, O.A. Sammour, Curcumin-loaded ultradeformable nanovesicles as a potential delivery system for breast cancer therapy, Colloids and Surfaces B: Biointerfaces, 167 (2018) 63-72.

S.M. Abdel-Hafez, R.M. Hathout, O.A. Sammour, Towards better modeling of chitosan nanoparticles production: Screening different factors and comparing two experimental designs, International Journal of Biological Macromolecules, 64 (2014) 334-340.

Conference contributions

S.M. Abdel-Hafez and M. Schneider, Extracellular matrix-modulating nano-structured microparticles for pulmonary inhalation as potential delivery system for lung cancer, oral presentation. The International Society for Aerosols in Medicine (ISAM) Congress, Saarbrücken, Germany, August 2023.

S.M. Abdel-Hafez and M. Schneider, Polysaccharide-based nano-structured microparticles for inhalation for lung cancer therapy, oral presentation. Annual Meeting of the German Pharmaceutical Society (DPhG), Marburg, Germany, September 2022.

S.M. Abdel-Hafez and M. Schneider, Acetalated maltodextrin pH-responsive nanoparticles: Formulation, characterization and cellular interaction studies, poster presentation. Annual Meeting of the German Pharmaceutical Society (DPhG), virtual conference, October 2021.

R.M. Hathout, H.A. Gad, **S.M. Abdel-Hafez**, N. Nasser, N. Khalil, T. Ateyya, A. Amr, N. Yasser, S. Nasr, A.A. Metwally, Gelatinized core liposomes: Towards an advanced carrier for hydrophilic drugs formulation, poster presentation. Controlled Release Society (CRS) Annual Meeting, Edinburgh, Scottland, July 2015.

S.M. Abdel-Hafez, R.M. Hathout, O.A. Sammour, Chitosan nanoparticles production: End of the debate, poster presentation. Biological Surfaces and Interfaces, Sant Feliu de Guixols, Catalonia, Spain, July 2013.

Teaching experience

Preparation, demonstration, laboratory supervision, and exam and assignment arrangement for undergraduate practical courses in the following topics:
- Pharmaceutical calculations
- Physical pharmacy
- Liquid, semisolid, and solid dosage forms
- Reaction and release kinetics
- Biopharmaceutics and biostatistics
- Industrial pharmacy

References are available upon request.

Acknowledgements

إن الحمد لله نحمده ونستعينه ونستهديه، الحمد لله أولا وآخرا على واسع فضله وجميل عطائه وعظيم نعمته، الحمد لله الذي بيده الخير كله، وإليه يرجع الأمر كله.

(وَإِن تَعُدُّواْ نِعْمَةَ ٱللَّهِ لَا تُحْصُوهَآ ۗ إِنَّ ٱللَّهَ لَغَفُورٌ رَّحِيمٌ) النحل: ١٨

This work would not have been accomplished if it weren't for the contribution and support of many people, to whom I would like to show my appreciation.

I would like to express my gratitude to my supervisor, **Prof. Dr. Marc Schneider**. Thank you for giving me the opportunity to pursue my doctoral degree under your supervision. You have always been supportive from the very beginning; from the first correspondences for setting the project, through the course of experiments, and till the final work stages. The constructive discussions, accepting the negative results and supporting the positive ones, and enabling me to extend and shape my own scientific experience, all added a lot to the value of the journey. I deeply thank you for always being considerate and making me feel welcome and comprehended. I would like to thank **Prof. Dr. Markus Gallei,** my second supervisor, for his positive contribution in supervising this thesis, and for the fruitful cooperation in the polymer characterization part.

I would like to thank **Dr. Josef Zapp** for performing the ^{1}H-NMR analysis and his input in this direction. I would like to thank **Assoc. Prof. Dr. Eman Dokla** for her useful remarks about the ^{1}H-NMR data. I would like to thank **Jun- Prof. Dr. Sangeun Lee** for her assistance with the polymer labeling and valuable notes throughout the work. I am grateful to **Pascal Paul** for his assistance with the scanning electron microscope, for his responsiveness and patience with troubleshooting. I would like to thank **Blandine Boßmann** for her help with the molecular weight and thermal analysis measurements. I would like to thank **Michelle Müller** for sharing her experience about spheroid culturing.

I would like to acknowledge the financial support granted by the **German Academic Exchange Service (DAAD)** and the **Egyptian Ministry of Higher Education**. I would like to thank them for their direction through the initial preparatory and administrative steps, and over four years of support.